Spray-Deposited Oxides for

Applications in Solar Cells

by

Woo Jung Shin

A Dissertation Presented in Partial Fulfillment
of the Requirements for the Degree
Doctor of Philosophy

Approved April 2019 by the
Graduate Supervisory Committee:

Meng Tao, Chair
Michael Goryll
Qing Hua Wang

ARIZONA STATE UNIVERSITY

May 2019

ABSTRACT

Photovoltaics (PV) is one of the promising options for maintaining sustainable energy supply because it is environmentally friendly, a non-polluting and low-maintenance energy source. Despite the many advantages of PV, solar energy currently accounts for only 1% of the global energy portfolio for electricity generation. This is because the cost of electricity from PV remains about a factor of two higher than the fossil fuel (10¢/kWh). Widely-used commercial methods employed to generate PV energy, such as silicon or thin film-based technologies, are still expensive as they are processed through vacuum-based techniques. Therefore, it is desirable to find an alternative method that is open-air and continuous process for the mass production of solar cells.

The objective of the research in this thesis is to develop low-cost spray pyrolysis technique to synthesize oxides thin films for applications in solar cells. Chapter 4 and 5 discuss spray-deposited dielectric oxides for their applications in Si solar cells. In Chapter 4, a successful deposition of Al_2O_3 is demonstrated using water as the solvent which ensures a lower cost and safer process environment. Optical, electrical, and structural properties of spray-deposited Al_2O_3 are investigated and compared to the industrial standard Atomic Layer Deposition (ALD) Al_2O_3/Plasma Enhanced Chemical Vapor Deposition (PECVD) SiN_x stack, to reveal the suitability of spray-deposited Al_2O_3 for rear passivation and optical trapping in p-type Si Passivated Emitter and Rear Cell (PERC) solar cells. In Chapter 5, The possibility of using low-cost spray-deposited ZrO_2 as the antireflection coating for Si solar cells is investigated. Optical, electrical and structural properties of spray-deposited ZrO_2 films are studied and compared to the industrial standard antireflection coating PECVD SiN_x. In Chapter 6, spray-deposited hematite Fe_2O_3

and sol-gel prepared anatase TiO_2 thin films are sulfurized by annealing in H_2S to investigate the band gap narrowing by sulfur doping and explore the possibility of using ternary semiconductors for their application as solar absorbers.

ACKNOWLEDGMENTS

TABLE OF CONTENTS

LIST OF TABLES

LIST OF FIGURES

CHAPTER 1

INTRODUCTION

1.1. Background

Today, most of the energy is generated by burning fossil fuels (coal, oil, natural gas) and other non-renewable sources. However, fossil fuel sources such as coal and natural gas are limited and there is pressing need to look for alternate sources of energy. Figure 1.1 shows a prediction on future global energy demand [1]. The topmost curve indicates that we are currently consuming energy at an average rate of about 20 terawatts globally. By 2050, the demand is predicted to reach 30 TW and by 2100 46 TW. Therefore, solar energy needs to expand to terawatt-scale deployment to meet the power demand in the future.
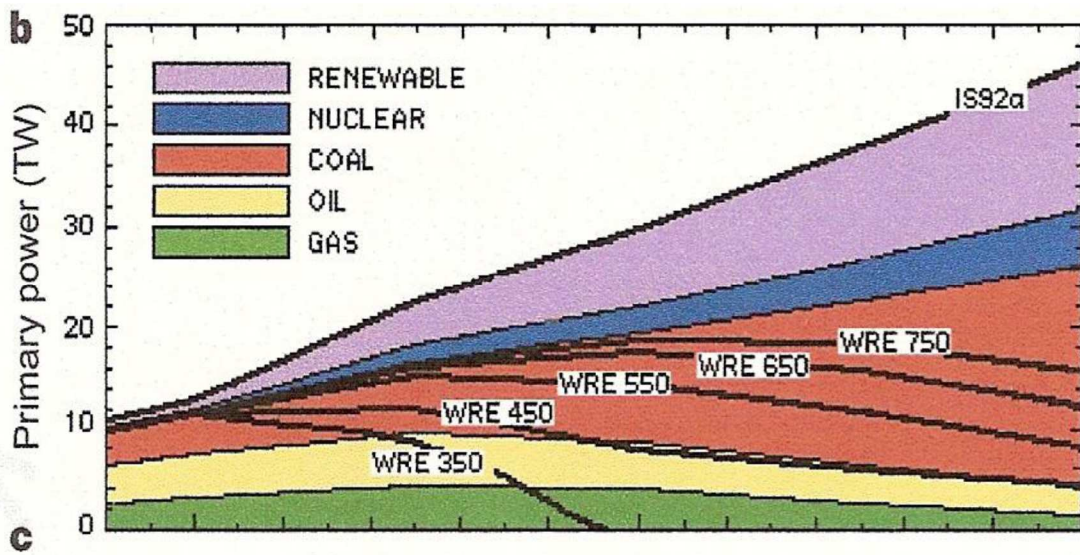
Figure 1.1 Predicted global energy demands through 2100 [1].

According to the data shown in Figure 1.2 [2], installations of solar photovoltaic (PV) panels have reached 120 gigawatts (GW) during 2018. Compared to 60 GW installed during 2015, photovoltaics capacity in the world have doubled in 2018.
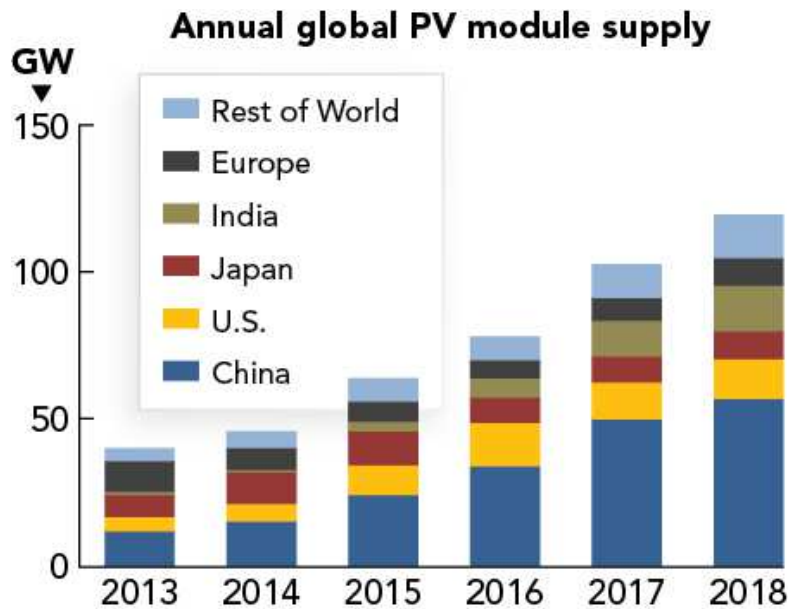
Figure 1.2 Annual global PV module supply from 2013 to 2018 [2].

Fig. 1.3 shows the PV global shipment share by technology. Crystalline-Si (c-Si) solar modules including mono-Si modules and multi-Si modules have always been the major technology with a ~95% market share. Figure 1.4 shows the expected market share of different c-Si solar cell technologies in the future. Aluminum back surface field cells which is known as the standard cell has been a major technology in the past, covering about 90% of the market share in 2015. However, PERC cells which is known as (Passivated Emitter and Rear Cell) is expected to become dominant in the future. Already, PERC is used in about 20% of PV capacity and it is predicted to be used in more than half of the cell production by 2026.
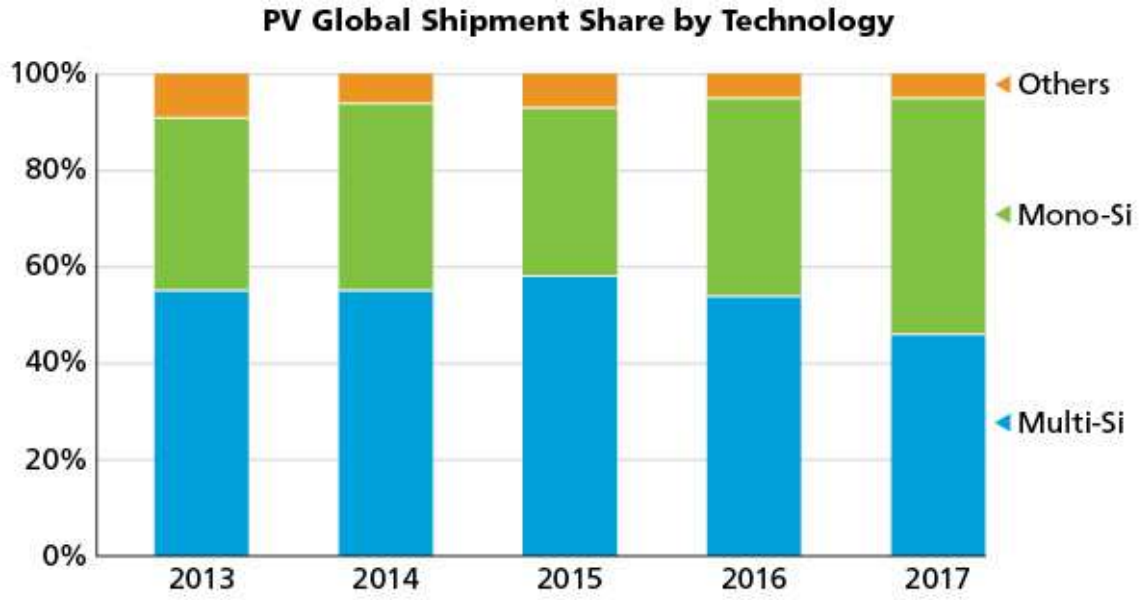
Figure 1.3 PV global shipment share by technology [3].
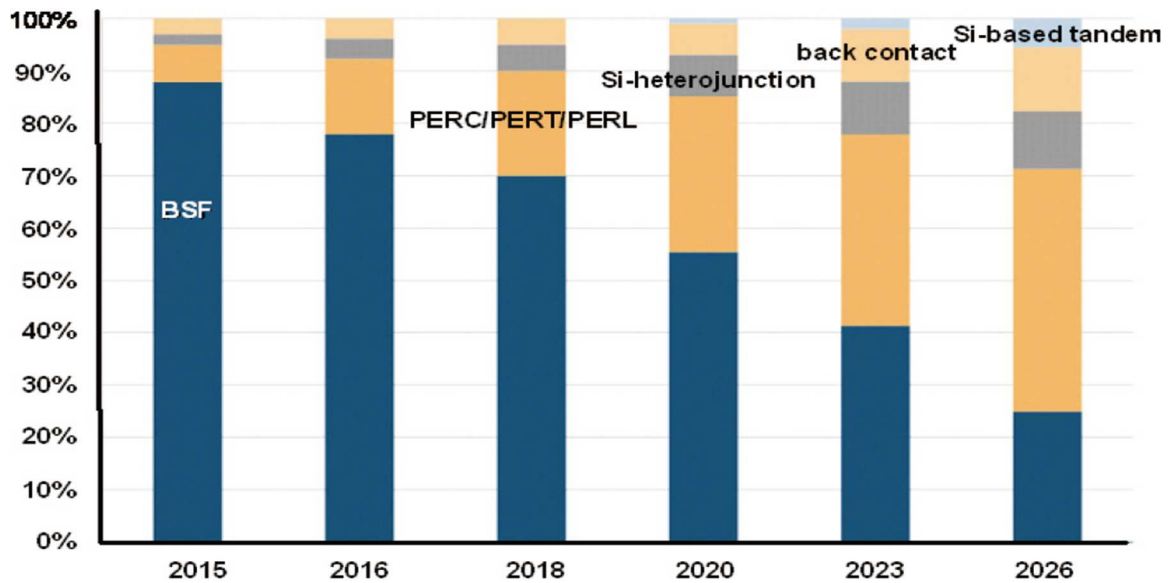
Figure 1.4 Expected market share of different Si cell technologies [4].

Fig. 1.5 (a) shows the structure of Al-BSF cell. While Al-BSF cells have back surface

field on the rear side, PERC cells have thin dielectric layers inserted between P-type Si and

aluminum as shown in Fig. 1.5 (b). There are two advantages of having dielectric films on the rear side: (1) Thin layer of Al_2O_3 reduces rear surface recombination on p-type Si by chemical and field effect passivation. (2) Low refractive index of Al_2O_3 improves light trapping in the Si cell by rear reflection. Combination of these advantages results in 1% absolute gain in efficiency, and therefore PERC cells have a great potential for producing high efficiency solar panels in the future.
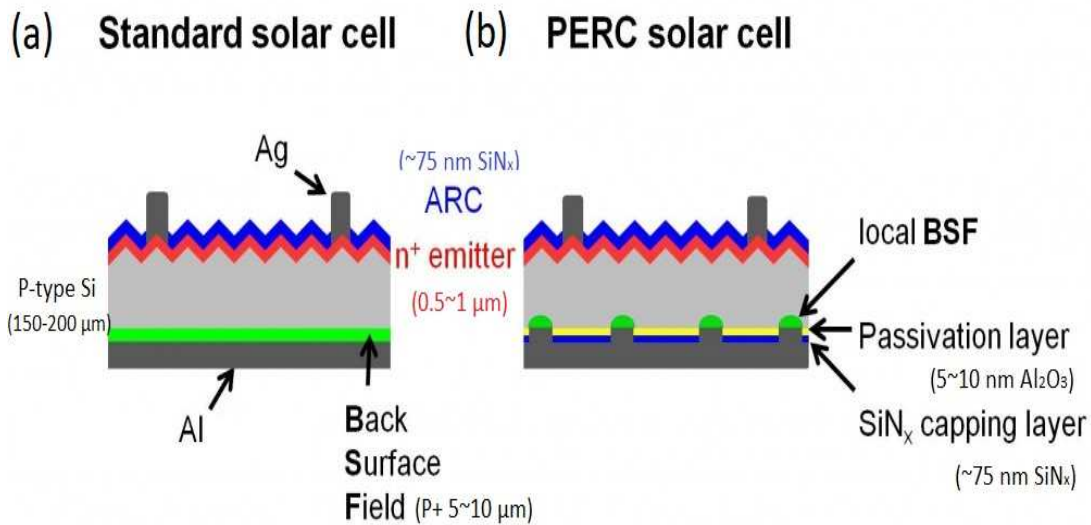
Fig. 1.5 Comparison of Al-BSF Cell and PERC cell structure [5].

1.2 Deposition Techniques of Dielectrics in Crystalline-Si Solar Cells

In general, dielectric films with uniform thickness are synthesized by vacuum-based processes such as physical vapor deposition including thermal evaporation or reactive sputtering and chemical vapor deposition including plasma-enhanced chemical vapor deposition (PECVD) and atomic layer deposition (ALD). In current industry, The SiN_x is prepared by PECVD and the Al_2O_3 is prepared by ALD.

Plasma-enhanced Chemical Vapor Deposition- SiN_x

4

Silicon nitride (SiN_x) grown by plasma-enhanced chemical vapor deposition is widely used as an antireflection coating as well as a surface passivation layer for the phosphorous doped emitter on p-type silicon. SiN_x is also known to provide excellent passivation (SRV <10 cm/s) on p-type Si wafers [6] by inducing an inversion layer due to its high positive charge density of $\sim 10^{12}$ cm^{-2} [7]. However, when SiNx is used for rear passivation for PERC-type solar cells, this electron-rich inversion layer shunts the local back contacts resulting significant loss in the short-circuit current density due to the out flow of electrons from the back. This phenomenon is referred to as parasitic shunting. Therefore, direct SiN_x is not a good candidate for back surface passivation.

Atomic Layer Deposition (ALD)

Previously, it was demonstrated that a thin Al_2O_3 film grown by atomic layer deposition system can also provide an excellent surface passivation on 1 Ω-cm p- and n- type Si wafers as well as on boron-doped p+ emitters [8]. This is because, contrary to PECVD SiN_x film, Al_2O_3 film contains very high negative charge density ($\sim 10^{13}$ cm^{-3}) which forms an accumulation layer in p-Si, so no parasitic shunting occurs. This is because minority carrier electrons are repelled back into Si by the accumulation layer when Al_2O_3 is used for rear side passivation of p-type PERC solar cells [9]. However, the process of ALD is very slow and this is known to be its major limitation. Other disadvantages of ALD process include high equipment cost and high precursor cost. This provided the motivation in this research to examine the formation of low-cost spray-deposited Al_2O_3 oxide to achieve high quality passivation and rear reflection.

1.3 Spray Pyrolysis Technique

The spray pyrolysis technique is a low-cost, non-vacuum required, way to synthesize materials in the form of powders and films. In the case of films, they are usually deposited over a wide variety of substrates that can be easily adapted for large area deposition and industrial production processes. Unlike many other film deposition techniques, spray pyrolysis represents a very simple and relatively cost-effective processing method. It offers an extremely easy technique for preparing films of any composition. Typical spray pyrolysis equipment consists of an atomizer, spray nozzle, precursor solution, substrate heater, and temperature controller as shown in Fig. 1.6.
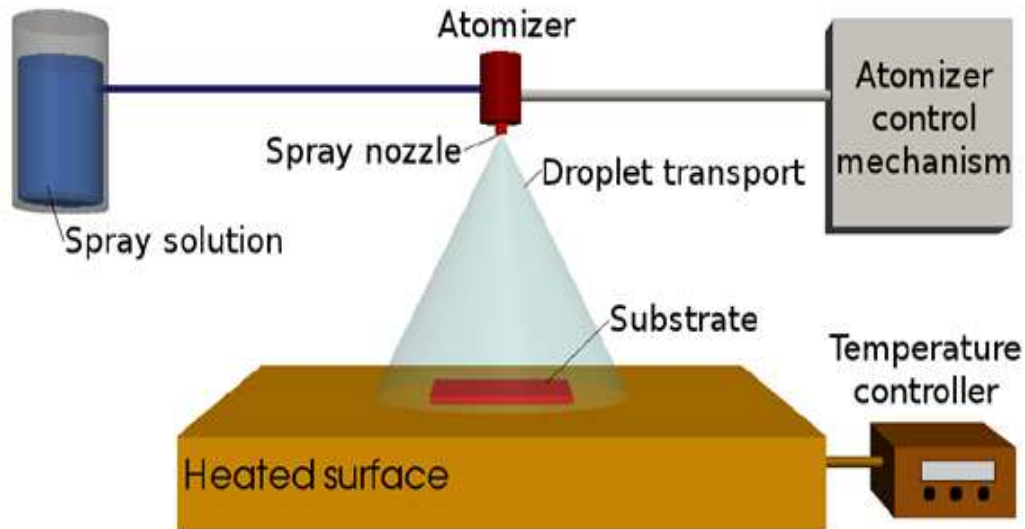
Figure 1.6 General schematics of a spray pyrolysis deposition process [10].

Spray pyrolysis uses liquid phase precursor. Typically, metal precursors are dissolved in starting solution which contains water, organic solvent, or the mixer of these two. Atomizer in the middle generates solution into small droplets, and these fine droplets are sprayed

6

onto a hot substrate using carrier gas, which is typically air. When the droplets get closer to the heated substrate, solvent evaporates, solid precursor melts and undergoes chemical reaction to form oxides on the substrate.

Spray pyrolysis is a very simple and relatively cost-effective processing method. Therefore, if good quality dielectrics can be synthesized by spray pyrolysis, it will allow us to achieve an increase in efficiency of solar cells without much of an increase in cost.

CHAPTER 2

WORKING PRINCIPLES AND LOSS MECHANISMS IN SOLAR CELLS

2.1 Working Principles of Si Solar Cells

A solar cell is a power delivering device that converts sunlight into electricity. The electricity generation from solar cells is based on a particularly designed p-n junction diode under illumination. The process of converting sunlight into voltage or electrical energy using solar cells is called photovoltaic effect that incorporates following three basic steps: (1) When sunlight strikes a semiconductor or solar cell, a large number of electron-hole pairs are created in the device through absorption of photons with energy greater than the bandgap of the semiconductor; (2) The electron-hole pairs diffuse randomly and are then separated by electrical field inside the p-n junction; (3) The electrons end up in the n-type semiconductor and the holes on the p-type side resulting in a charge separation or voltage across the junction that leads current flow into the external circuit or load.

Figure 2.1 illustrates a schematic of a Si solar cell and its basic operation. The fabrication of current baseline type commercial cell involves formation of a p-n junction on the front side, a silicon nitride (SiNx) anti-reflection coating (ARC) on the emitter surface, screen-printed silver (Ag) grid lines on the front side and full-area aluminum (Al) on the rear side. During a short high-temperature contact firing process, the Ag grid makes electrical contact on the front and Al dopes the silicon to form a p+ Al back surface field (BSF) and contact on the rear. The BSF provides moderate passivation and optical reflection on the rear side of the cell. Currently, most commercial solar cells use screen-printing technique to form the front and back contacts because of simplicity, high-throughput, and low manufacturing cost.
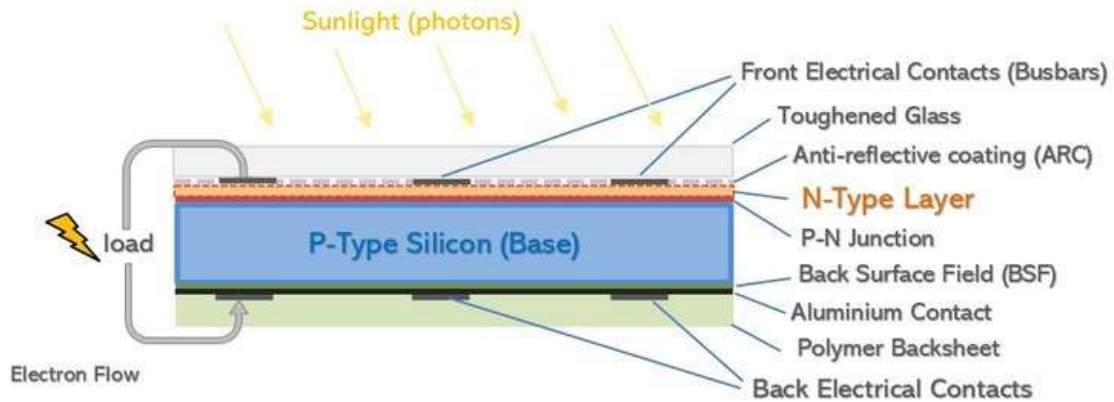
Figure 2.1 A schematic of a simple solar cell structure (Al-BSF) [11].

2.2 Loss Mechanisms in Solar Cells

An essential part for achieving high-efficiency is the reduction of various losses in a solar cell. Understanding the loss mechanisms is the foundation for designing high efficiency advanced solar cells. Since solar cell is an optoelectronic device, there are two major types of loss mechanisms in silicon solar cells: optical and electrical losses. Optical loss is referred to the loss of photons that could have generated electron-hole pairs in the cell. This loss reduces the short-circuit current and is attributed to front surface reflection, gridline shading and incompletely absorption of long wavelength light. Electrical loss is the photons that got absorbed in the cell but were not able to contribute to the cell power output. This loss can reduce both short-circuit current and open-circuit voltage via carrier recombination and parasitic resistances. Figure 2.2 shows a schematic of optical loss mechanisms in a solar cell.

9
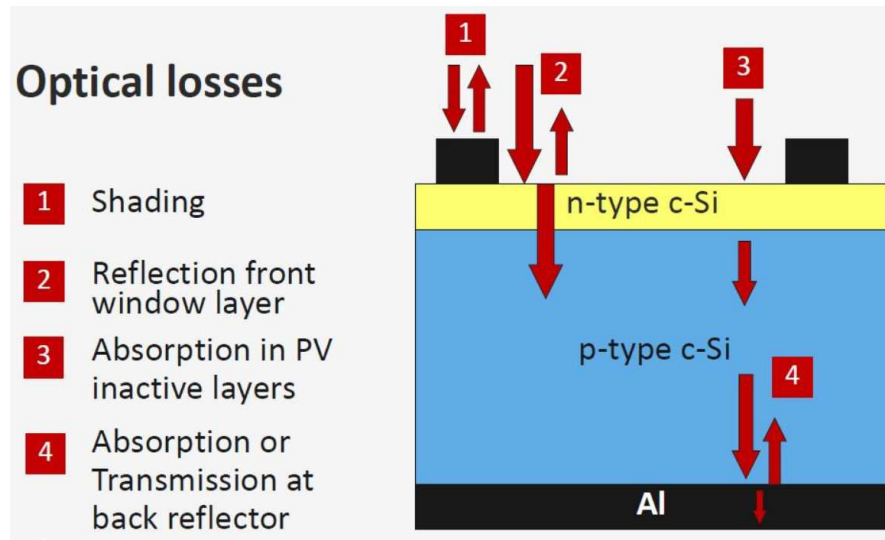
Figure 2.2 Optical loss mechanisms in solar cells [12].

2.3 Reflection Loss and Anti-reflection Coating

The reflection loss is attributed to a fraction of incident light reflected from the cell surface. A bare silicon surface reflects about 30% of the incident light because of the high refractive index of the silicon (n = 3.4). The surface reflection can be minimized by applying anti-reflection coating (ARC) and/or surface texturing on the front surface of the cell. The anti-reflection coatings are typically formed by dielectric layers with properly designed thicknesses and refractive indexes to produce destructive interference in the rays reflected from the air-ARC interface and from the ARC-Si interface. Figure 2.3 illustrates the mechanism of an anti-reflection coating on the cell.
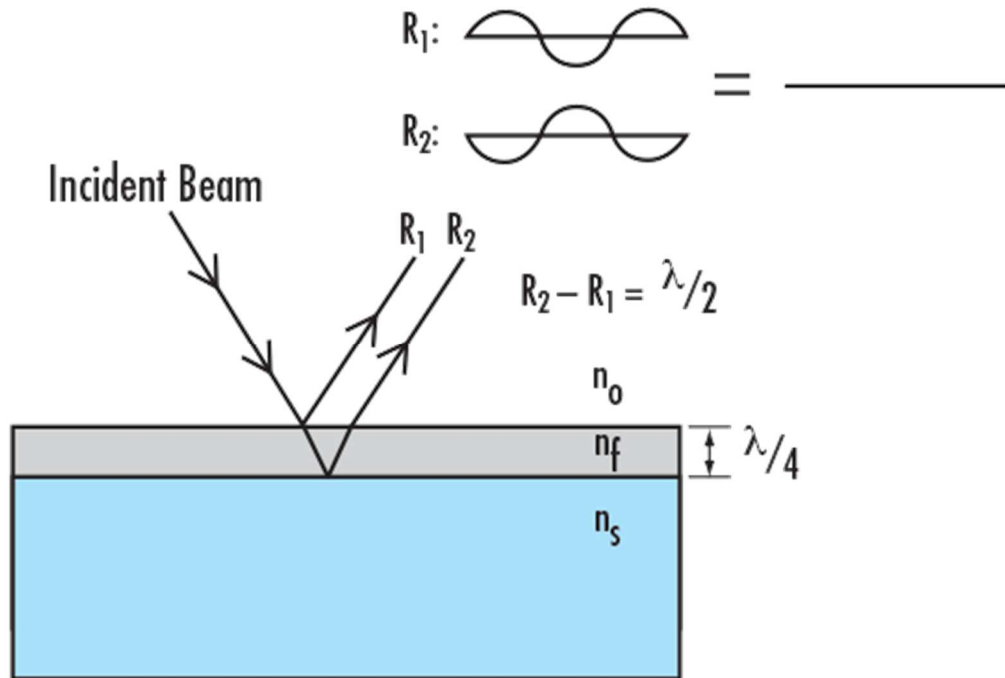
Figure 2.3 Anti-reflection coating to reduce the surface reflection [13].

The thickness of the anti-reflection coating is chosen so that the wavelength in the dielectric material is one quarter the wavelength of the incoming wave. For a quarter wavelength anti-reflection coating of a transparent material with a refractive index n_f and light incident on the coating with a free-space wavelength λ, the thickness d which causes minimum reflection can be calculated by:

$$d = \lambda/n_f \quad (2.1)$$

For the broad solar spectrum, about 600nm is used to determine the thickness of the antireflection layer since it is close to the wavelength at maximum solar intensity. Reflection is further minimized if the refractive index of the anti-reflection coating on either side; that is, glass or air and the semiconductor. This is calculated by:

$$n_f = \sqrt{n_0 n_s} \quad (2.2)$$

11

Where n_0 and n_s are the refractive indices of the materials below and above. As solar cells are typically packaged into modules, the material on top of the cells is glass or EVA with refractive indies of about 1.4. Therefore, the optimum index of antireflection layer on wafer-Si solar cells is around 2.34 with $n_{si} = 3.9$ at 600nm.

2.4 Recombination Loss

When an electron in the valence band (VB) absorbs a photon (h ν >Eg) and undergoes a transition to the conduction band (CB) then we have an extra electron in CB and a hole in VB. This process by which an electron-hole pairs are created is known as generation. When light falls on the solar cell, electron-hole pairs are generated which are responsible for conversion of light energy into electrical energy. However, if the electrons and holes recombine in the bulk or at the surface of the solar cell before they can reach external circuit, then it is known as recombination.
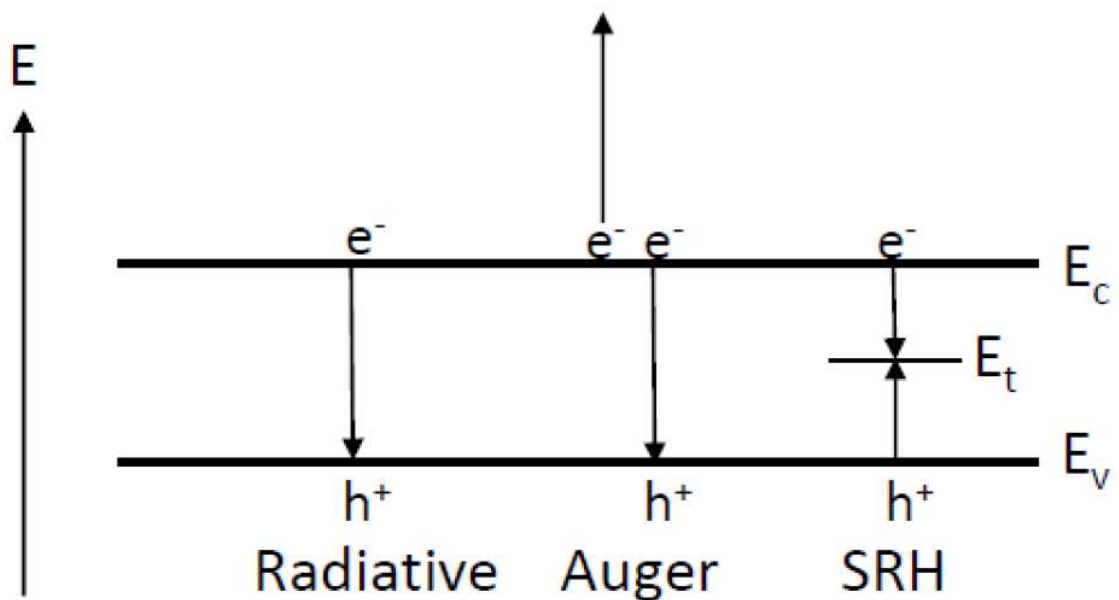
Fig. 2.4 Schematic of recombination mechanism.

12

Radiative Recombination

   Radiative recombination is also referred to as band-to-band recombination, reverse of the photogeneration in a semiconductor. In the radiative recombination, an electron in the conduction band directly annihilates a hole in the valance band and then releases the energy as a photon. This energy corresponds to the bandgap of the semiconductor. Radiative recombination is more significant in direct band-gap semiconductors (e.g. GaAs) than in indirect ones (e.g. Si). This is because a phonon is required to conserve both energy and momentum in an indirect bandgap material.

Shockley-Read-Hall Recombination

   Recombination through defects, also called Shockley-Read-Hall or SRH recombination, does not occur in perfectly pure, un-defected material. SRH recombination is a two-step process. The two steps involved in SRH recombination are: (1) An electron (or hole) is trapped by an energy state in the forbidden region which is introduced through defects in the crystal lattice. These defects can either be unintentionally introduced or deliberately added to the material, for example in doping the material; and (2) If a hole (or an electron) moves up to the same energy state before the electron is thermally re-emitted into the conduction band, then it recombines. The rate at which a carrier moves into the energy level in the forbidden gap depends on the distance of the introduced energy level from either of the band edges. Therefore, if an energy is introduced close to either band edge, recombination is less likely as the electron is likely to be re-emitted to the conduction band edge rather than recombine with a hole which moves into the same energy state from the

valence band. For this reason, energy levels near mid-gap are very effective for recombination.

Auger Recombination

Auger Recombination involves three carriers. An electron and a hole recombine, but rather than emitting the energy as heat or as a photon, the energy is given to a third carrier, an electron in the conduction band. This electron then thermalizes back down to the conduction band edge. Auger recombination is most important at high carrier concentrations caused by heavy doping or high-level injection under concentrated sunlight. In silicon-based solar cells (the most popular), Auger recombination limits the lifetime and ultimate efficiency. The more heavily doped the material is, the shorter the Auger recombination lifetime.

Surface Recombination

Surface recombination is associated with the defect levels within the bandgap at the surface due to abrupt termination of the crystal lattice material. These surface states promote recombination which can be analyzed by applying the bulk SRH recombination theory with minor reformations. For a single level surface state, the surface recombination rate, U_s, is given by:

$$U_s = \frac{n_s p_s - n_i^2}{\dfrac{n_s + n_1}{S_{p0}} + \dfrac{p_s + p_1}{S_{n0}}} \quad (2.3)$$

Where n_s and p_s are the electron and hole concentrations at the surface, S_{po} and S_{no} and are surface recombination velocities of holes and electrons which are related to surface state density (N_{st}), and the capture cross-sections of the electron and hole (δ_n and δ_p):

$$S_{n0} \equiv \delta_n v_{th} N_{st} \text{ and } S_{p0} \equiv \delta_p v_{th} N_{st} \quad (2.4)$$

the surface recombination velocity is related to the surface recombination rate according to:

$$S \equiv \frac{U_s}{\Delta n} = \frac{n_{s0} + p_{s0+\Delta n}}{\frac{n_s + n_1}{S_{p0}} + \frac{p_s + p_1}{S_{n0}}} \quad (2.5)$$

Surface recombination lifetime ($\tau_{surface}$) can be defined as:

$$\tau_{surface} = (\frac{2S}{W} + \frac{1}{D}(\frac{W}{\pi})^2)^{-1} \quad (2.6)$$

where W is wafer thickness and D is the diffusion coefficient of minority carrier. For a silicon solar cell, the wafer thickness is typically around 200 μm. The second term in Equation (2.6) is very small and therefore it can be dropped resulting in:

$$\tau_{surface} = (\frac{2S}{W})^{-1} \quad (2.7)$$

In practice, the surface states are not localized at a single energy level but are continuously distributed throughout the bandgap of a semiconductor. Moreover, the density of surface states and the capture cross-sections are dependent on their energy level. Hence, the total surface recombination rate of a real semiconductor is obtained by integrating Equation (2.3) over the entire energy bandgap:

$$U_s = \int_{E_v}^{E_c} \frac{n_s p_s - n_i^2}{\frac{n_s + n_1(E)}{\delta_p(E)} + \frac{p_s + p_1(E)}{\delta_n(E)}} v_{th} \cdot D_{it}(E) dE \quad (2.8)$$

where E_c is the minimum conduction band energy, E_v is the maximum valance band energy, D_{it} is the density of surface states per unit energy ($cm^{-2}eV^{-1}$).

The four recombination mechanisms occur simultaneously in a semiconductor material. The effective recombination rate, U_{eff}, is the sum of the individual recombination rate, which is given as:

$$U_{eff} = U_{rad} + U_{Auger} + U_{SRH} + U_{surface} \quad (2.9)$$

The effective lifetime is therefore given as:

$$\frac{1}{\tau_{eff}} = \frac{1}{\tau_{rad}} + \frac{1}{\tau_{Auger}} + \frac{1}{\tau_{SRH}} + \frac{1}{\tau_{surface}} \quad (2.10)$$

2.5 Surface Passivation

Surface recombination loss has become increasingly important in industrial solar cells due to the trend toward large-area and thinner silicon wafers. Consequently, the reduction of surface recombination is an important task in this research to obtain high efficiency commercial scale solar cells. In practice, surface recombination can be reduced by chemical passivation and field-effect passivation.

The chemical passivation is based on the reduction of the density of surface states (D_{it}). The surface defect density can be significantly reduced by depositing thin dielectrics that can satisfy the dangling bonds at the surface of wafers. A high-quality thermal oxide film (SiO_2) on Si is commonly used to reduce the density of surface states (D_{it}) and a subsequent anneal in a forming gas can further reduce the D_{it} value.

The surface recombination relates to the electron and hole concentrations at the surface. The highest recombination rate occurs when the electron and hole concentrations at the surface are equal. The field-effect passivation is based on the reduction of the electron or hole concentration at the semiconductor surface by using a built-in electric field that can repeal either the electron or the hole from the surface. The built-in electric field can be achieved by doping the surface or by the introducing a charged dielectric at the surface. For conventional p-type cells, the field- effect passivation is typically obtained by a p+-doping at the back surface called the back-surface field (BSF). A negatively charged

16

dielectric such as Al_2O_3 can also effectively passivate the surface of p-type Si by field-effect passivation.

CHAPTER 3

CHARACTERIZATION TECHNIQUES

3.1 Photoconductance Based Lifetime Tester

The passivation quality of spray-deposited oxides on Si was tested by Sinton lifetime tester WCT-120, and a schematic is given in Figure 3.1. The sample of interest is inductively coupled by the coil to an rf-bridge circuit, which senses changes in the sample's permeability and therefore its conductance. Measurements can be taken using either Quasi-Steady-State-Photo-Conductance (QSSPC) method or Transient Photo-Conductance Decay (Transient PCD). In our work, the effective minority carrier lifetime was measured using QSSPC method and evaluated in generalized mode. The calibration was checked with the reference calibration wafer provided by the manufacturer. Depending on the average thickness and refractive index of the film, optical constant values between 0.675 and 0.975 is used to evaluate the measured lifetime.
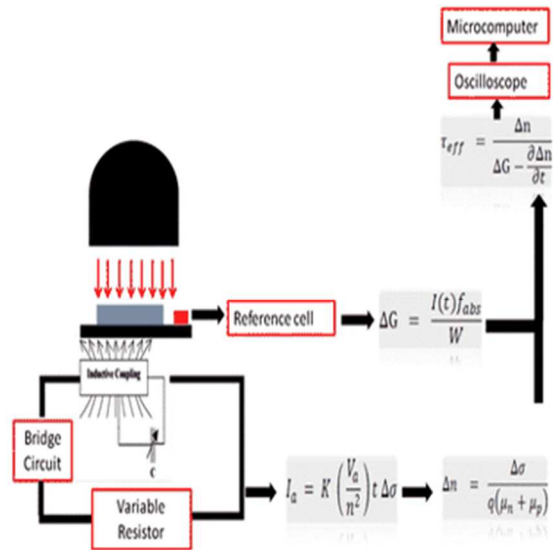
Figure 3.1 Schematic of the inductively coupled photoconductance apparatus used for

measuring the effective lifetime [14].

3.2 Capacitance-Voltage (C-V)

A CV curve measurement of a MOS capacitor is a convenient method for the extraction of many material properties. It can provide information about dielectric properties and interface quality. Dielectric constant can be determined from a single measurement from a HF CV curve in accumulation. The equivalent circuit of the MOS capacitor includes only the oxide capacitance and the series resistance of the device. The dielectric constant of the dielectric film is then:

$$C = \frac{K_s \varepsilon_0 A}{W} \quad (3.1)$$

Where K_s is relative permittivity.

Additional information can be obtained from a HF CV curve about the density of oxide charge. Oxide charge is different from interface charge because it's independent from gate bias. There are three types of oxide charge Q. The first type is the oxide fixed charge Q_f. The density of fixed charges can be determined by

$$Q_f = (\Delta\phi_{MS} - V_{FB}) \times C_{ox}/A \quad (3.2)$$

Where V_{FB} is the flat-band voltage, and $\Delta\phi_{MS}$ is work-function difference between metal contact and Si. The second type is the oxide trapped charge Q_{ot} that can be located at the metal-dielectric or silicon-dielectric interface. The third type of oxide charge is the mobile ionic charge Q_m that is caused usually by the presence of ionized alkali metal atoms like sodium or potassium. Fixed and trapped oxide charge density is related to the voltage shift

19

of a CV curve with respect to the theoretical result. For both p-type and n-type silicon, a positive oxide charge density will shift the CV curve towards more negative values of gate bias. The opposite happens for negative oxide charge densities. Thus, from the direction of the shift the polarity of the oxide charge can be determined.

3.3 Ultraviolet-Visible Spectroscopy (UV-Vis)

In this thesis, transmittance and reflectance spectrums were measured with a JASCO UV-Vis spectrophotometer. The spectrometer measures transmittance as a percentage (%T); this represents the percentage of the incident beam of light transmitted by the sample. This value is then used to calculate absorbance:

$$A = \log(1/T) \quad (3.3)$$

A number of things happen when a beam of light comes into contact with a solid. The beam may be reflected, transmitted, diffused, absorbed, refracted or polarized as shown in Figure 3.2.
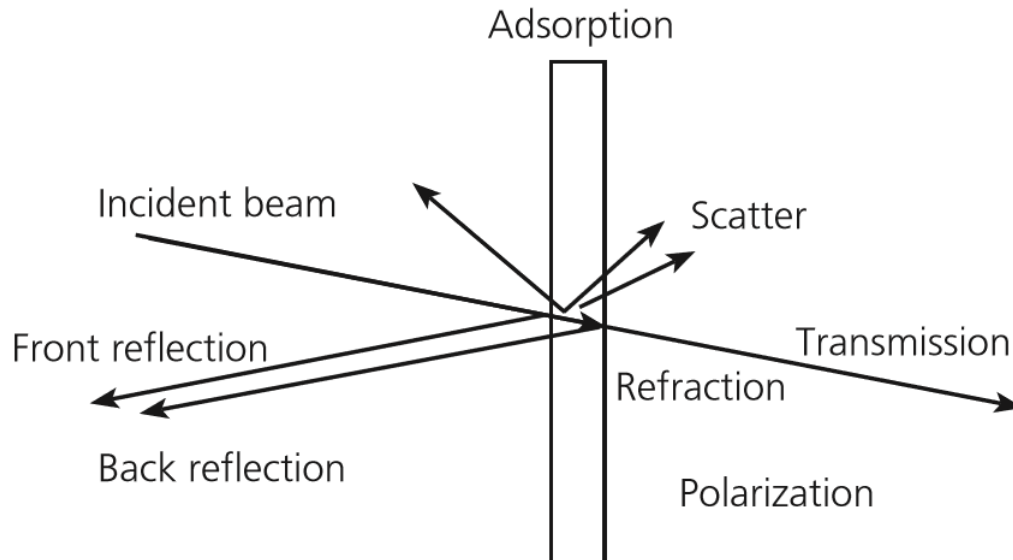
Figure 3.2 Interactions of light with a solid [15].

For our experiments, overall transmittance, i.e. direct transmittance plus diffuse transmittance, and overall reflectance, i.e specular reflectance and diffuse reflectance was measured with an integrating sphere over a range of 200-2500 nm. The sample is placed against the sphere and the beam transmitted or reflected by the sample is reflected onto the internal reflective surface of the sphere before reaching the detectors inside the sphere as shown in Figure 3.3. The sample is placed in front of the sphere if transmittance is being measured and behind it if reflectance is being measured.
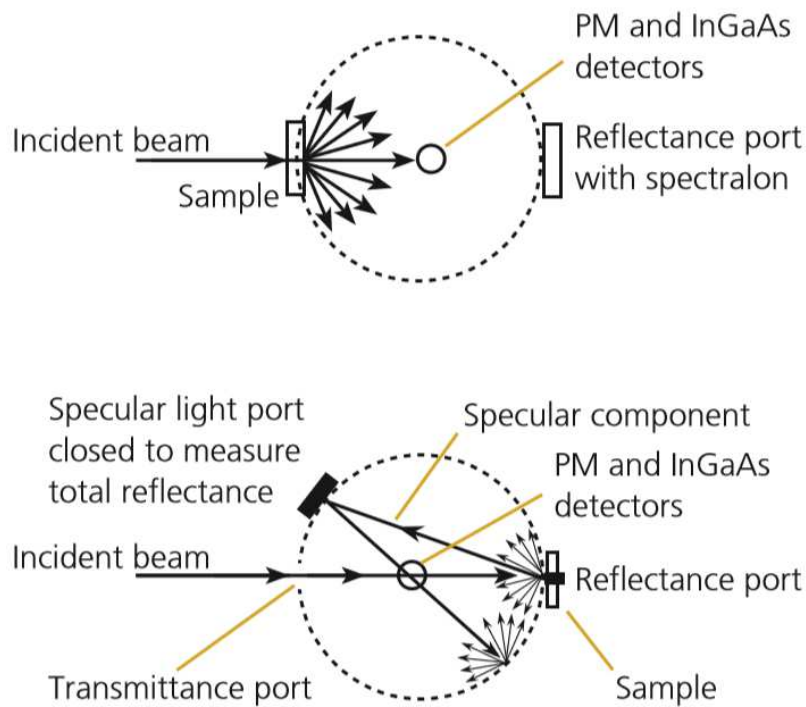
Figure 3.3 Measurements with a integrating sphere: reflectance (lower); transmission (upper) [15].

3.4 Ellipsometry

Ellipsometry is a non-destructive, sensitive technique for determining optical properties of surfaces and thin films. It measures a change in polarization as light reflects or transmits from a material structure. The polarization change is represented in terms of an amplitude ratio, Ψ, and the phase difference, Δ. These two coefficients contain information related to material optical properties and physical dimensions and are measured as a function of wavelength. A scheme of ellipsometry measurement is shown in Figure 3.4
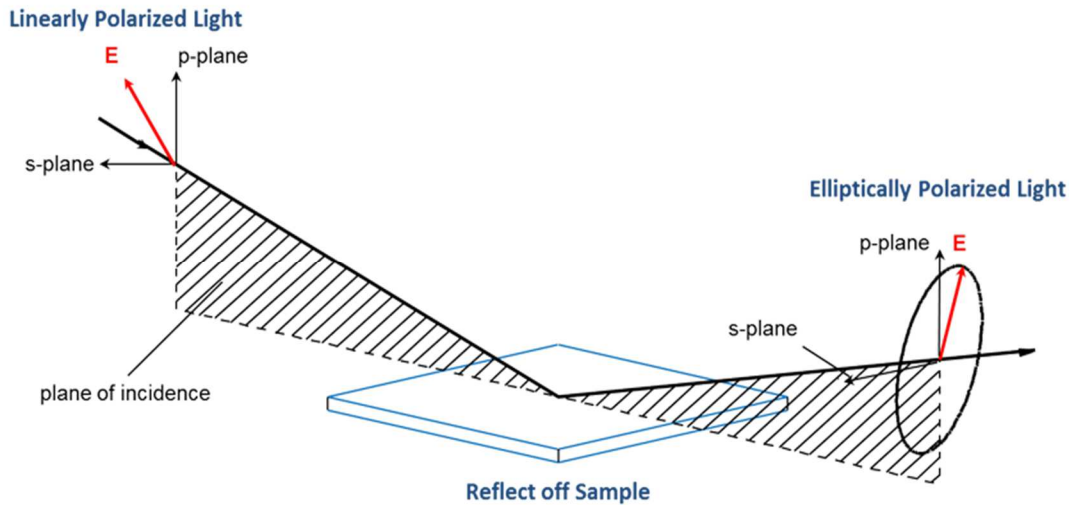
Figure 3.4 Typical ellipsometry configuration [16].

Ellipsometry is a model dependent technique, i.e. it is not possible to determine directly the physical quantities (dielectric functions, refractive indices, material composition, film thicknesses etc). Therefore, the fitting process is performed to adjust the theoretical sample (previously built) to the experimental data (real measure) using VASE32 software. Ellipsometry measurements were performed by a variable angle spectroscopic ellipsometer (Woolam VASE) in the wavelength range of λ=300–1200 nm.

3.5 Atomic Force Microscopy (AFM)

Atomic force microscopy (AFM) was utilized for characterization of the surface morphology of deposited thin films and estimation of their roughness. A schematic illustration of the main part of the AFM instrument is shown in Figure 3.5.

A Atomic Force Microscope

Laser

Segmented Photodiode

Cantilever with Tip

Sample

XYZ Scanner

B AFM Imaging Modes

Contact Mode

Tapping or Non-contact Mode
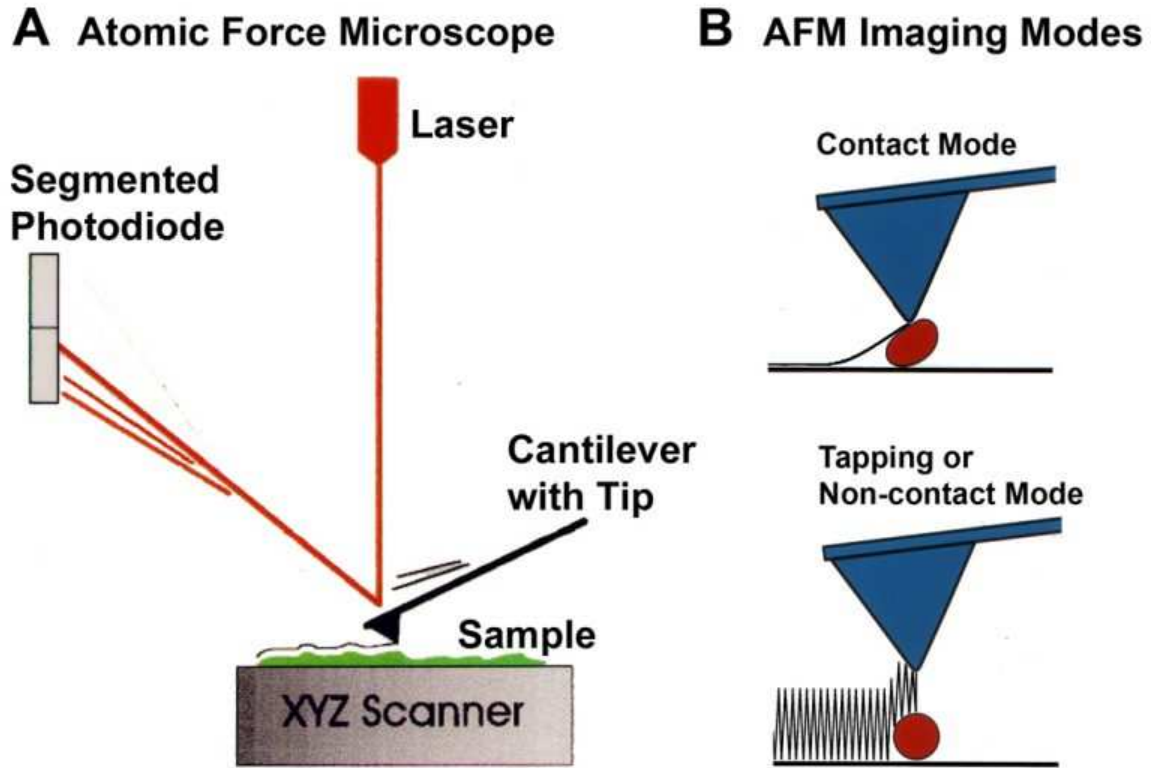
Figure 3.5 Schematic of AFM microscope [17].

The roughness of the films is usually presented by Root mean square (RMS) roughness R_q. Root mean square (RMS) roughness, R_q, is the root mean square average of the roughness profile ordinates:

$$R_q = \sqrt{\frac{1}{l}\int_0^1 Z^2(x)\,dx} \quad (3.4)$$

23

where Z(x) is profile ordinates of the roughness profile. The surface topography and roughness were examined by Parks AFM.

3.6 X-ray Diffraction (XRD)

X-ray diffraction (XRD), being a non-destructive technique provides information of crystal structures, identification of different phases and crystallite size. The technique works on the principle of Bragg's law i.e. $2d\mathrm{Sin}\theta = n\lambda$, where d is the distance between two consecutive planes, λ is wavelength of incident beam and θ is the scattering angle. For diffraction, the wavelength of incident beam must be comparable to the dimensions of the aperture i.e. of interatomic distances in crystals; hence gives information about the crystal structure. When Bragg condition is satisfied, a peak appears in the diffraction pattern. Using, x-rays of known wavelength and Bragg peak position, one can determine the d spacing of various lattice planes in the sample.

In case of thin films, x-ray diffraction measurements using conventional $\theta/2\theta$ scan generally generates a weak signal from the film and strong signal from the substrate. Therefore, to avoid strong signal from the substrate and to enhance signal from the film grazing incidence x-ray diffraction (GIXRD) has been used. In the measurements, detector scan is performed with a fixed grazing angle of incidence which is generally chosen to be slightly above the critical angle for total reflection from the film material. Figure 3.6 shows the schematic of typical GIXRD setup.
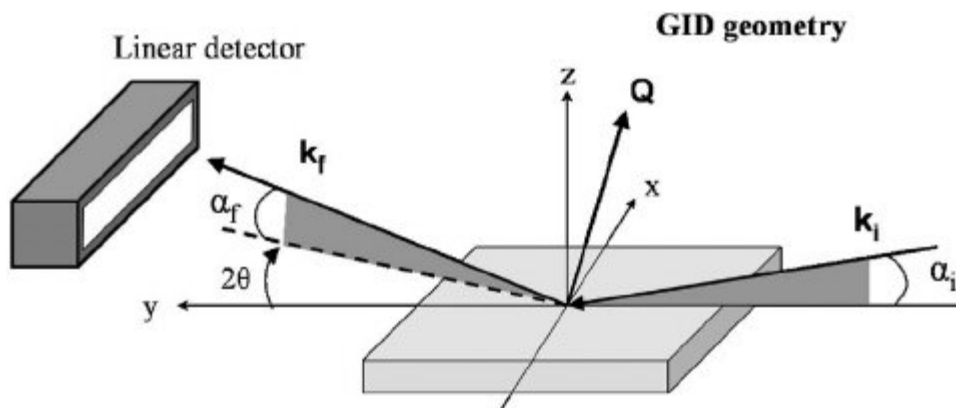
Figure 3.6 Geometry of typical GIXRD setup [18].

3.7 X-ray Photoelectron Spectroscopy (XPS)

Photoelectron spectroscopy is a surface sensitive technique which gives information about elemental composition of material and chemical state of atom in material. The technique works on the principle of photoelectron emission. When the photons from x-ray source of sufficient energy is made to incident on sample, then ejection of photoelectrons take place having kinetic energy given as:

$$E_{kinetic\ energy} = \text{hv} - E_{binding\ energy} - \varphi \quad (3.5)$$

An electron spectrometer known as concentric hemispherical analyzer (CHA) measures the kinetic energy of photoelectrons, which in turn is converted to binding energy scale. The schematic of typical XPS setup is shown in Figure 3.7. The Binding energy position as well as shape of photoelectron peak gives information about the chemical state of element in material while peak area is used to determine the elemental composition of materials. Being a surface sensitive technique the information about material is obtained only up to the escape depth of photoelectron. Escape depth of photoelectron is the depth

25

from the surface up to which photoelectron is emitted which is in general of the order of

~20- 30 Å in XPS measurements.
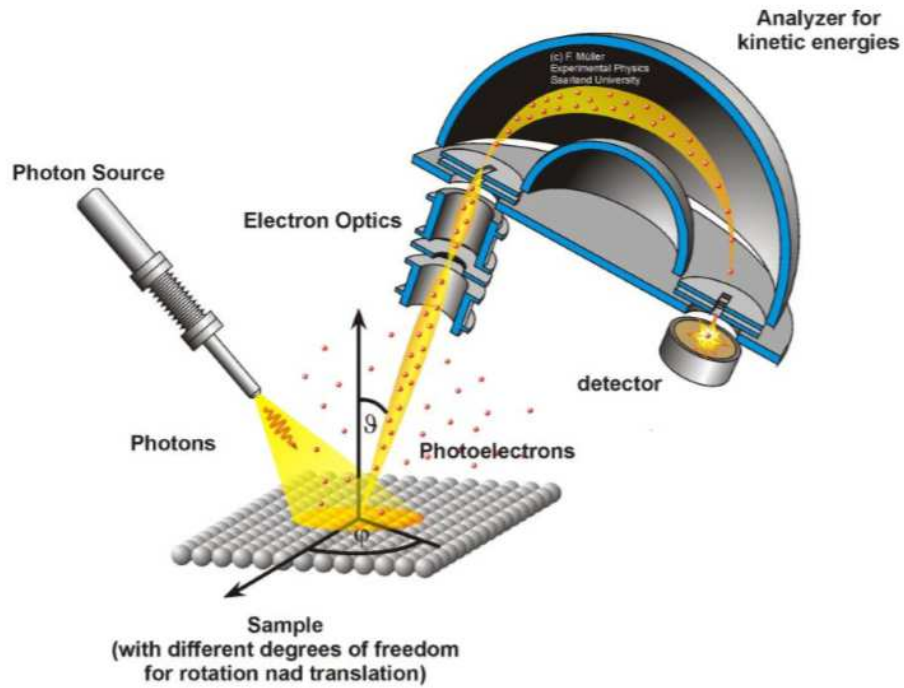
Figure 3.7. Schematic of typical XPS setup [19].

CHAPTER 4

SPRAY-DEPOSITED AL$_2$O$_3$ FOR REAR PASSIVATION AND OPTICAL TRAPPING

IN SILICON SOLAR CELLS

4.1 Introduction

The solar photovoltaic industry has been dominated by the Al back-surface field (BSF) cell for many years. However, the Al BSF technology is approaching its practical limit, and further gains in efficiency are unlikely. The search for continued efficiency improvements has led to the adoption of the passivated emitter rear contact (PERC) cell which offers a 1% absolute gain in efficiency by integrating a localized BSF structure [20]. As of 2016, PERC cells accounted for 15% of the global Si solar cell production and they are expected to become the dominant cell technology in the near future [4]. In PERC cells, a thin layer of Al$_2$O$_3$, about 10 nm, is deposited on the rear of the Si cell, which reduces rear surface recombination on p-type Si by chemical and field effect passivation [21]. Optically the 10-nm Al$_2$O$_3$ film is supported by an 80-nm SiN$_x$ layer which is stacked on Al$_2$O$_3$, and the low refractive index of SiN$_x$ improves light trapping in the Si cell by rear reflection [22].

Al$_2$O$_3$ films are typically synthesized by vacuum-based processes such as atomic layer deposition (ALD) [23], plasma-enhanced chemical vapor deposition (PECVD) [24], metal organic chemical vapor deposition [25], atmospheric pressure chemical vapor deposition [26], and sputter deposition [27]. For commercial Si PERC cells, the Al$_2$O$_3$ film is prepared by ALD. ALD is a slow process and the precursor for Al$_2$O$_3$, Al$_2$(CH$_3$)$_6$, is expansive and pyrophoric. For these reasons the thickness of the Al$_2$O$_3$ film in Si PERC cells is limited to about 10 nm and an 80-nm SiN$_x$ layer is deposited on Al$_2$O$_3$ by PECVD to provide rear

reflection as shown in Fig 4.1(a). It is noted that the refractive index of Al_2O_3 is lower than that of SiN_x, 1.6 vs. 2.0 [23,28], so a thicker Al_2O_3 film on the rear of the PERC cell as shown in Fig 4.1(b) should provide better optical trapping than an Al_2O_3/SiN_x stack. This requires a low-cost process to deposit thicker Al_2O_3 on Si.
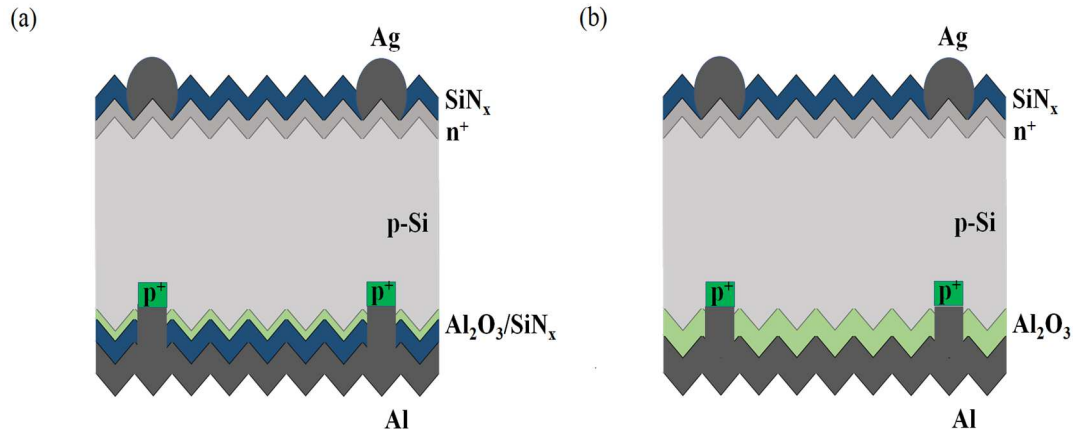
Figure 4.1. Schematic structure of the p-type Si PERC cell with a (a) 10-nm Al_2O_3/80-nm SiN_x stack and (b) thicker Al_2O_3 layer on the rear.

Non-vacuum processes such as sol-gel deposition [29] or spray deposition [30] have been explored for Al_2O_3. However, those studies used high-temperature processes (850˚C in O_2) or toxic and expensive solvents such as 2-methoxyethanol. Since spray pyrolysis is a continuous, open-air process, the use of organic solvents at high temperatures introduces potential fire and explosion risks in mass production. In this chapter, we report successful Al_2O_3 deposition on Si by spray pyrolysis using water as the solvent, which ensures a lower cost and safer process. Optical, electrical, and structural properties of spray-deposited Al_2O_3 are investigated and compared to the industrial standard ALD Al_2O_3/PECVD SiN_x

stack, to reveal the suitability of spray-deposited Al_2O_3 for rear passivation and optical trapping in Si PERC cells.

4.2 Experimental

Amorphous Al_2O_3 films were obtained by spray deposition in air. The precursor solution was prepared with 0.1 M Al acetylacetonate ($Al(C_5H_7O_2)_3$) and 0.2 M HCl in water. HCl was added to completely dissolve the Al precursor in the solution. The Si wafers used in this work were textured p-type Czochralski (CZ) (100) wafers of 2 Ω-cm. The thickness of the wafers was 200 μm and they were cut into pieces of 4×4 cm^2. Si substrates were cleaned with diluted HF to remove native oxide from the surface before spray deposition. The starting Si substrates had a minority carrier lifetime of 20 μs after HF dip. The substrate was placed on a hotplate and the temperature of the hotplate was set between 400˚C and the highest temperature of the hotplate, 550˚C. In order to reduce the fluctuations in substrate temperature and provide ample time for solvent evaporation, pulsed spray deposition was employed with each cycle comprised of 10 s on and 50 s off [31]. The optimized deposition parameters for Al_2O_3 are listed in Table 4.1.

For a comparative study, 10-nm ALD Al_2O_3 and 80-nm PECVD SiN_x were deposited sequentially on Si substrates at 200˚C using $Al_2(CH_3)_3$ and a mixture of SiH_4 and NH_3 as the precursors, respectively. Optical and electrical properties of the Al_2O_3/SiN_x stack were measured and compared with those of spray-deposited Al_2O_3.

Table 4.1

Optimized parameters for spray deposition of Al_2O_3 films

Nozzle-substrate distance (cm)	65
Al concentration (M)	0.1
Solution flow rate (ml/min)	17
Carrier gas	Air
Atomization/piston pressure (pa)	35/40

Capacitance-voltage (C-V) measurements were performed using a MDC C-V system with a Hg probe. For current-voltage (I-V) characterization, a MDC probe station equipped with a HP 4140B current meter was used. The refractive index of Al_2O_3 films was measured with a Woollam VASE ellipsometer. Optical properties of Al_2O_3 films were characterized with a JASCO V-670 spectrophotometer. X-ray diffraction (XRD) spectra were obtained using a Panalytical X-ray diffractometer under grazing incident angles. Surface roughness of the films was measured by a Park System atomic force microscope (AFM). The thickness of Al_2O_3 films on textured Si substrates was analyzed using a Hitachi S4700 field-emission scanning electron microscope (SEM). Elemental analysis was carried out with a VG 220i-XL X-ray photoelectron spectrometer. The minority carrier lifetime was measured with a Sinton WCT-120 lifetime tester. Measurements were taken using Quasi-Steady-State-Photo-Conductance (QSSPC) method, and the effective minority carrier lifetime was evaluated in generalized mode.

4.3 Surface Passivation of p-type Si by Spray-Deposited Al_2O_3

The first experiment carried out was the optimization of the spray deposition parameters for Al_2O_3. The minority carrier lifetime of Si substrates covered with Al_2O_3 on both sides was monitored for this experiment. As shown in Fig 4.2, the minority carrier lifetime

strongly depends on deposition parameters such as deposition temperature, Al_2O_3 thickness, and post-annealing conditions. Fig. 4.2(a) presents the effect of deposition temperature on minority carrier lifetime. The thickness of Al_2O_3 was fixed to 80 nm. The lifetime increases linearly with deposition temperature from 400°C to 550°C, and 550°C is the highest temperature the hotplate can achieve. The minority carrier lifetime is 170 μs at 550°C, while the starting substrate has a lifetime of 20 μs. Samples prepared at 550°C were post-annealed in nitrogen at different conditions to further improve the minority carrier lifetime. Fig. 4.2(b) compares the minority carrier lifetime of Si with 80-nm Al_2O_3 at different post-annealing temperatures for 1 hr. The lifetime increases from 205 μs to 280 μs with post-annealing temperature from 400°C to 550°C. At 600°C, the lifetime decreases. Fig. 4.2(c) shows the effect of post-annealing time on minority carrier lifetime. The post-annealing temperature and the thickness of Al_2O_3 were fixed to 550°C and 80 nm, respectively. The lifetime increases from 234 μs to 280 μs with annealing time from 30 min to 1 hr. Further increase in annealing time above 1 hr does not result in a higher lifetime. Fig. 4.2(d) illustrates the effect of Al_2O_3 thickness on minority carrier lifetime. The lifetime was measured before and after post annealing in nitrogen at 550°C for 1 hr. In both cases, the maximum lifetime was obtained with 80-nm Al_2O_3. From this experiment, the best deposition parameters were identified as: deposition temperature 550°C, Al_2O_3 thickness 80 nm, post-annealing temperature 550°C, and post-annealing time 1 hr. These parameters were used in all the following experiments.
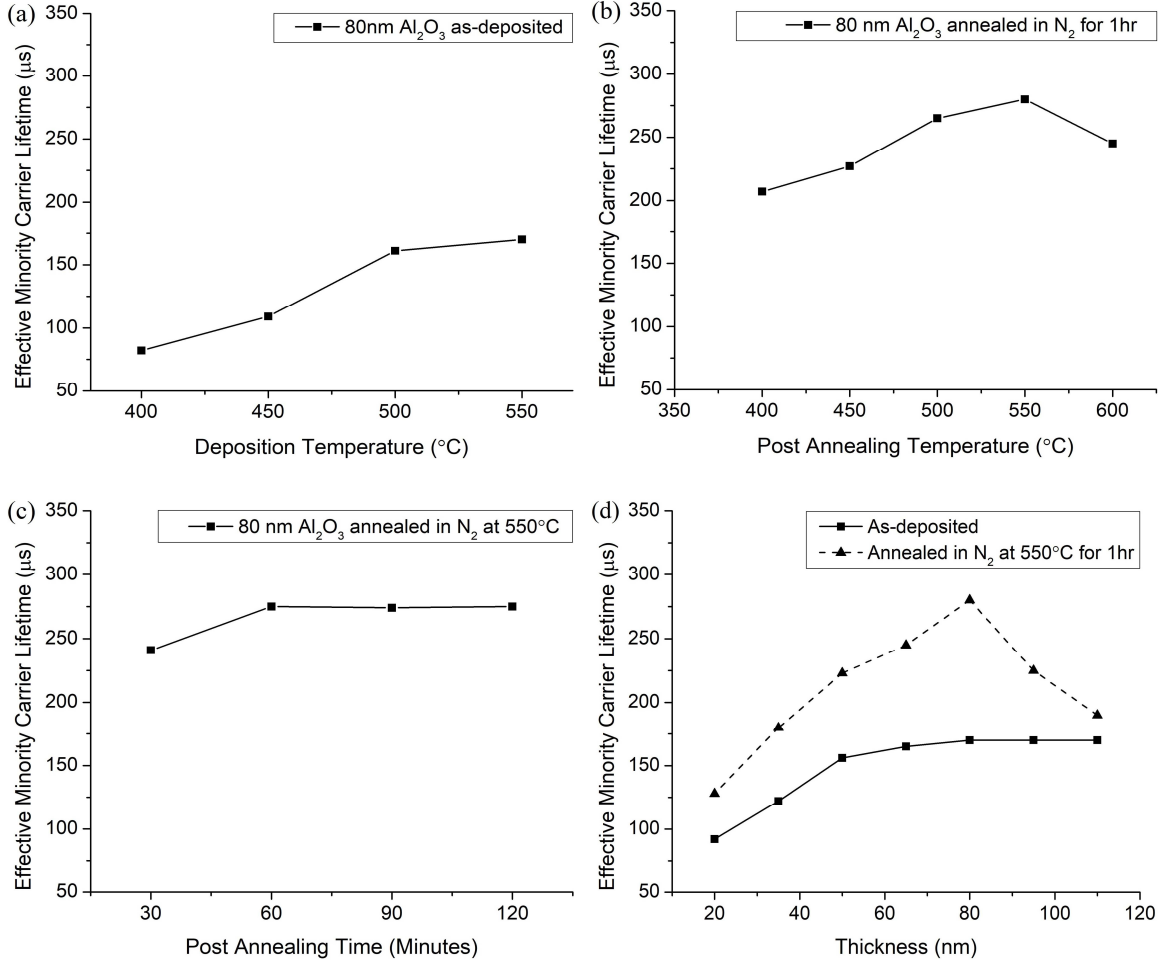
Figure 4.2. Minority carrier lifetime of p-type Si covered by Al_2O_3 on both sides at different (a) deposition temperatures, (b) post-annealing temperatures, (c) post-annealing times, and (d) Al_2O_3 thicknesses.

Fig. 4.3 shows the minority carrier lifetime for a Si sample as a function of excess carrier concentration. The Si sample was covered with Al_2O_3 on both sides using the optimized deposition parameters described above. A lifetime of 280 μs is obtained at the excess carrier concentration of 4×10^{15} cm^{-3}. From the measured minority carrier lifetime, the surface recombination velocity, S_{eff}, is calculated using the following equation [32]:

$$\frac{1}{\tau_{eff}} = \frac{1}{\tau_{bulk}} + \frac{1}{W/2S_{eff} + W^2/(D_n\pi^2)} \quad (4.1)$$

where τ_{bulk} is the bulk lifetime of the substrate, W and D_n are the thickness and electron diffusion coefficient of the substrate, respectively. S_{eff} was calculated assuming an infinite bulk lifetime and $D_n = 29.82$ cm^2/s for Si substrates of 2 Ω-cm [33]. A S_{eff} value of 35.89 cm/s is obtained for the sample with 80-nm Al$_2$O$_3$ on both sides after post annealing at 550°C for 1 hr.
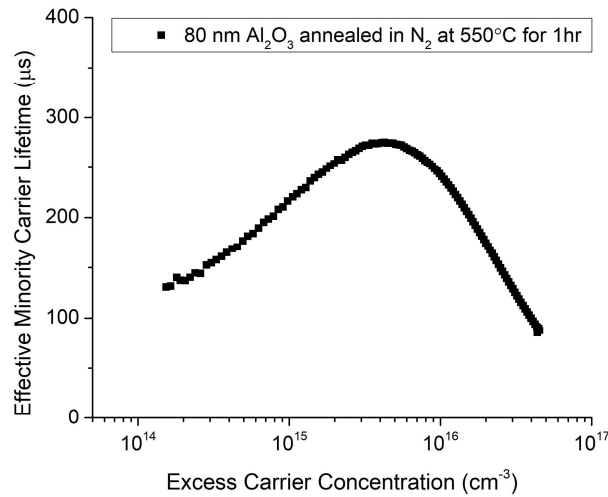
Figure 4.3. Minority carrier lifetime as a function of excess carrier concentration. The lifetime was measured on a Si sample covered with Al$_2$O$_3$ using the optimized deposition parameters.

4.4 Film Thickness Measurement

The thickness of Al$_2$O$_3$ films on Si substrates was measured using both destructive and non-destructive methods as shown in Figs. 4.4 and 4.5. Fig. 4.4 shows SEM cross-sectional images of Al$_2$O$_3$ deposited on polished and textured Si substrates. As shown in Fig. 4(a), the Al$_2$O$_3$ film deposited on a polished substrate shows a uniform and smooth morphology

of 80 nm. However, the Al_2O_3 film deposited with the same parameters on a textured substrate shows thickness variations over the pyramidal surface due to shadowing effects caused by the pyramids. Fig. 4.4(b) is the SEM cross-sectional image of a sample with a lifetime of 280 μs. The thickness on top of a pyramid is about 135 nm, but it reduces to about 55 nm between pyramids. Since passivation quality strongly depends on the thickness of the Al_2O_3 layer as shown in Fig. 4.2(d), it is predicted that improvement in film thickness uniformity should enhance the passivation quality of Al_2O_3 on p-type Si.
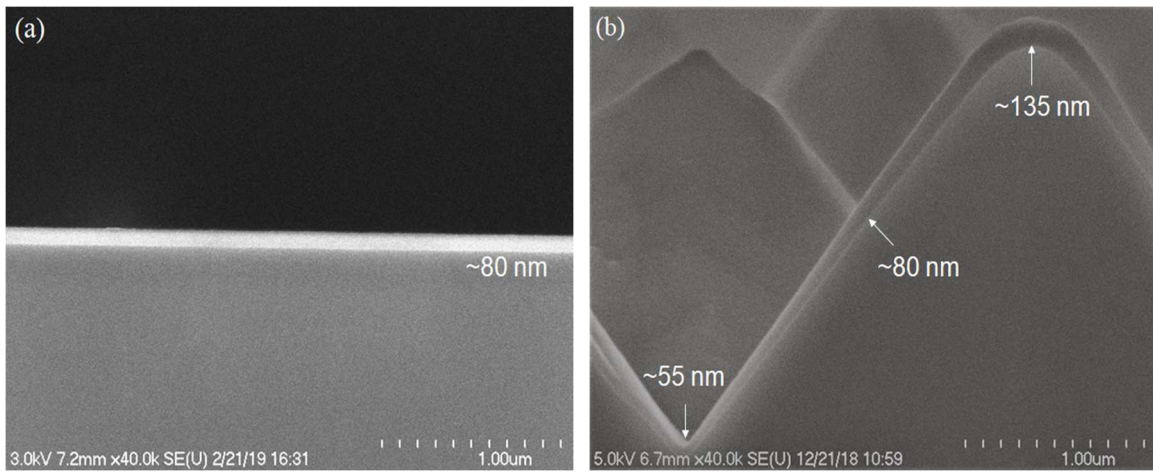
Figure 4.4. SEM cross-sectional images of Al_2O_3 films deposited on (a) polished and (b) textured Si(100) substrates.

Due to thickness non-uniformity on textured substrates, the average thickness of Al_2O_3 was measured using the refractive index and reflectance spectrum of Al_2O_3 as presented in Fig. 4.5. For a transparent film with a refractive index n, its thickness d can be calculated by:

$$d = \lambda/4n \ (4.2)$$

where λ is the minimum in the reflectance spectrum. Fig. 4.5(a) shows the reflectance spectrum of Al_2O_3 on textured Si. The optimized deposition parameters for a minority carrier lifetime of 280 μs were used to prepare the Al_2O_3 film on one side of the textured Si substrate. The minimum reflectance of 3.2% was found at the wavelength of 513 nm. At this wavelength, the corresponding refractive index of Al_2O_3 was measured to be 1.61 as shown in Fig. 4.5(b). Therefore, the average thickness of the Al_2O_3 film which resulted in the highest lifetime of 280 μs was calculated to be 79.65 nm.
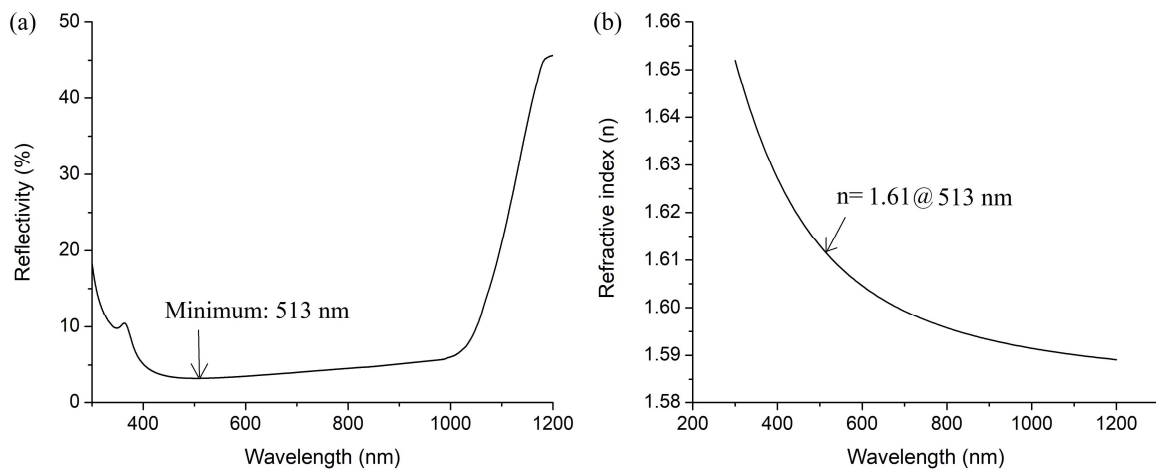
Figure 4.5. (a) Reflectance spectrum of textured Si covered with 80-nm Al_2O_3 on one side and (b) refractive index of 80-nm Al_2O_3 on textured Si.

4.5 C-V Characteristics of Al_2O_3

Fig. 4.6 shows the C-V characteristics of 80-nm Al_2O_3 on Si substrates measured at a frequency of 100 kHz using the retrace mode. The substrates for C-V were p-type polished CZ Si(100) wafers of 0.5 Ω-cm. Fig. 4.6(a) presents the C-V curve of a 80-nm Al_2O_3/Si sample after post annealing in nitrogen at 550˚C for 1 hr. The oxide capacitance of 410 pF translates into a dielectric constant of 8.1 for spray-deposited Al_2O_3 which was calculated

from the contact area of the Hg probe (0.456 mm^2) and the oxide thickness (80 nm). This value is close to Al$_2$O$_3$ prepared by ALD [23]. The flat-band voltage and density of fixed charges in 80-nm Al$_2$O$_3$ were calculated to be +5.5 V and -3.19×10^{12} cm^{-2}, respectively. The density of negative fixed charges in 80-nm spray-deposited Al$_2$O$_3$ is low compared to 45-nm ALD Al$_2$O$_3$ (10^{13} cm^{-2}) [34], which is likely due to more stoichiometry and fewer structural defects in spray-deposited Al$_2$O$_3$ than ALD Al$_2$O$_3$. Our spray-deposited Al$_2$O$_3$ is obtained at a higher deposition temperature, 550˚C vs. 200˚C for ALD, and with an ample supply of water as the solvent.

Fig. 4.6(b) reveals that the C-V curve at 450˚C shifts to the left as compared the C-V curve at 550˚C, indicating a lower density of fixed charges in the 450˚C film. In addition, a hysteresis exists in the 450˚C C-V curve revealing the existence of slow charges associated with defects. This suggests that the lower lifetime for lower deposition temperatures below 550˚C in Fig. 4.2(a) is likely due to the combined effect of a lower density of fixed charges and a higher density of interfacial defects. The interfacial defects are introduced by lower thermal energy provided to Al atoms at lower deposition temperatures. Moreover, the C-V curves at 450˚C and 550˚C both show a small hump which is characteristic of interface defects [35]. This hump disappears completely upon post annealing in nitrogen (Fig. 4.6(a)). There is no flat-band voltage shift between 550˚C as-deposited and post-annealed samples indicating that the improved lifetime after post annealing in Fig. 4.2(b) is likely caused by reduced interface defects, not by an increase in negative charge density.
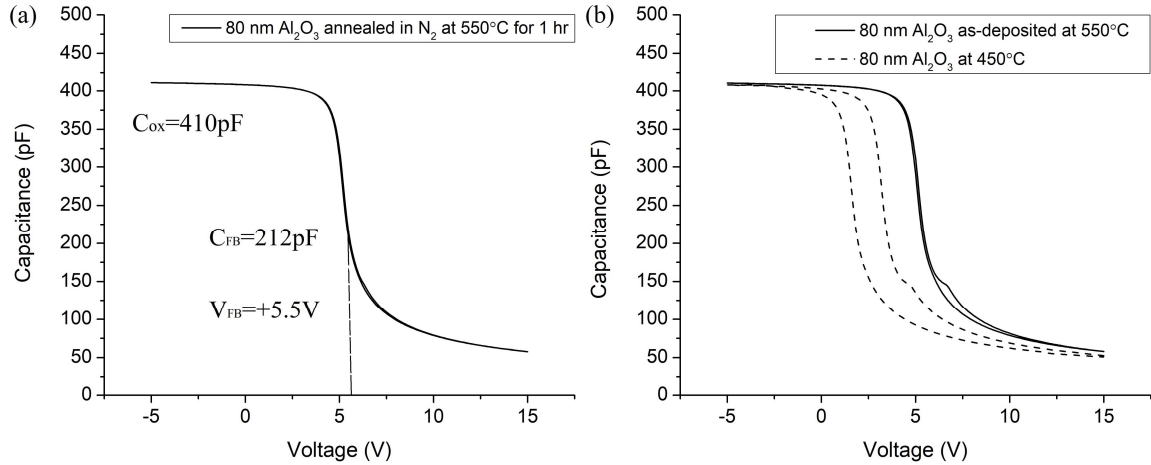
Figure 4.6. C-V characteristics of 80-nm Al$_2$O$_3$ deposited at (a) 550˚C followed by post annealing in nitrogen at 550˚C for 1 hr and (b) 450˚C and 550˚C without post annealing.

4.6 Light Trapping Characteristics of Spray-Deposited Al$_2$O$_3$ and ALD Al$_2$O$_3$/PECVD SiN$_x$ Stack

To compare light trapping between spray-deposited Al$_2$O$_3$ and industrial standard Al$_2$O$_3$/SiN$_x$ stack for Si PERC cells, Al$_2$O$_3$ of different thicknesses was spray-deposited on the rear of textured Si substrates and compared to a sample with a 10-nm ALD Al$_2$O$_3$/80-nm PECVD SiN$_x$ stack on the rear. 250 nm Al was deposited by electron-beam evaporation on spray-deposited Al$_2$O$_3$ and ALD Al$_2$O$_3$/PECVD SiN$_x$ stack to mimic the rear Al electrode in PERC cells. On the front side of the samples, 75-nm PECVD SiN$_x$ was deposited as the anti-reflection layer. Reflectance spectra were measured for these samples between 300 nm and 1,112 nm, the latter being the cutoff wavelength for Si at 48˚C. Fig. 4.7(a) shows the reflectance spectra of the samples with different thicknesses of spray-deposited Al$_2$O$_3$. There is little difference in reflectance between 300 nm and 1,000 nm, but the reflectance above 1,000 nm increases with the thickness of spray-deposited Al$_2$O$_3$. Fig.

37

4.7(b) compares the reflectance spectra of 80-nm spray-deposited Al_2O_3 with a 10-nm ALD Al_2O_3/80-nm PECVD SiN_x stack. The two reflectance spectra are almost identical. With the incident photon flux at AM1.5 as a function of wavelength, the difference in reflected photon flux between 80-nm spray-deposited Al_2O_3 and ALD Al_2O_3/PECVD SiN_x stack was calculated by multiplying the change in reflectance with the incident photon flux at each wavelength [31]:

$$\Delta\Phi_{Reflected}(\lambda) = [(R_{Al_2O_3}(\lambda) - R_{Al_2O_3/SiN_x}(\lambda)] \times \Phi_{Incident}(\lambda) \quad (4.3)$$

As shown in Fig. 4.7(c), negative values indicate that 80-nm spray-deposited Al_2O_3 reflects less than the ALD Al_2O_3/PECVD SiN_x stack. Integrating the change in reflected photon flux over wavelength reveals that spray-deposited Al_2O_3 reflects a net of 7.598×10^{17} $m^{-2}s^{-1}$ fewer photons than the ALD Al_2O_3/PECVD SiN_x stack. This is less than 0.03% of the total number of photons in the AM1.5 solar spectrum with energy above the Si bandgap, which is within the margin of error. Therefore, spray-deposited Al_2O_3 is optically identical to ALD Al_2O_3/PECVD SiN_x stack as the rear reflector in Si PERC cells.
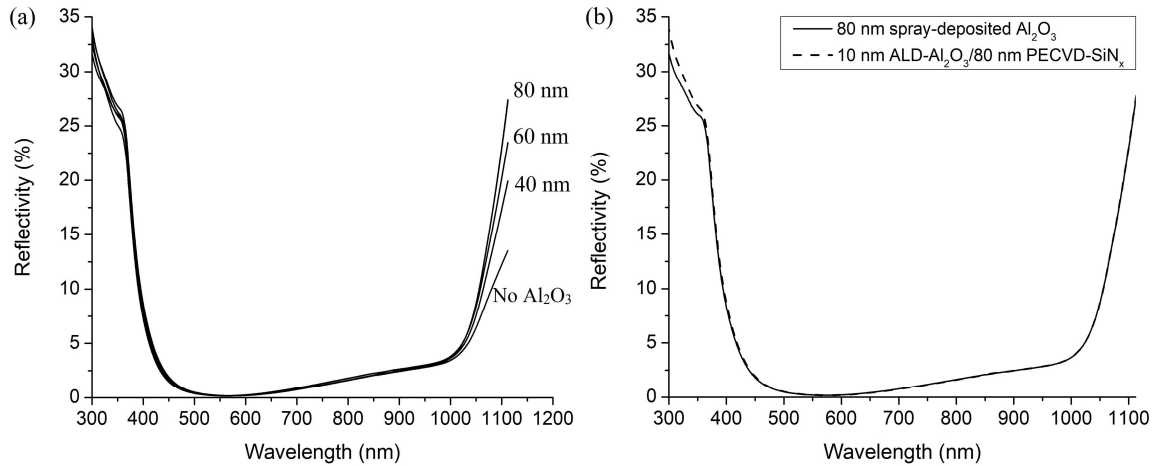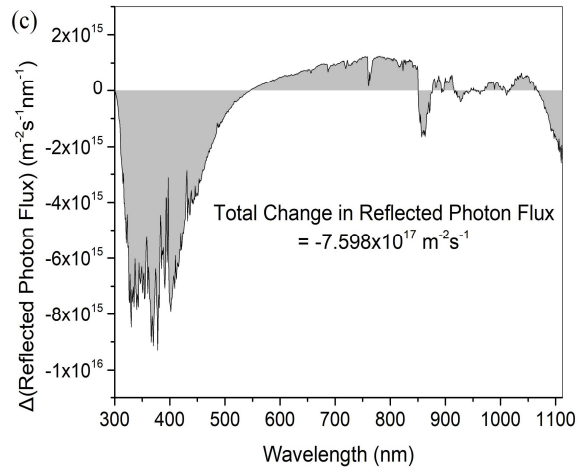
Figure 4.7. (a) Reflectance spectra of Al$_2$O$_3$ with different thicknesses on the rear of Si substrates. (b) Reflectance spectra of 80-nm spray-deposited Al$_2$O$_3$ and 10-nm ALD Al$_2$O$_3$/80-nm PECVD SiN$_x$. (c) Change in reflected photon flux between 80-nm Al$_2$O$_3$ and 10-nm Al$_2$O$_3$/80-nm SiN$_x$ as a function of wavelength.

4.7 X-Ray Diffraction and Surface Roughness of Al$_2$O$_3$

Fig. 4.8(a) shows a XRD spectrum of a 500-nm Al$_2$O$_3$ film after post annealing at 550˚C. No diffraction peaks over the entire range of two theta indicate that spray-deposited Al$_2$O$_3$ under the optimized deposition parameters is amorphous. Fig. 4.8(b) is an AFM scan of an 80-nm Al$_2$O$_3$ film on a polished Si(100) substrate after post annealing at 550˚C. The scan area is 9×9 μm^2. As shown in the 3-dimensional AFM scan, the surface roughness of the Al$_2$O$_3$ film is very low in the range of ±1 nm. The smooth morphology with small surface roughness agrees with the amorphous nature of the film revealed by XRD. The profile scan in Fig. 4.8(b) reveals that the root mean square surface roughness is 0.52 nm for the 80-nm film.
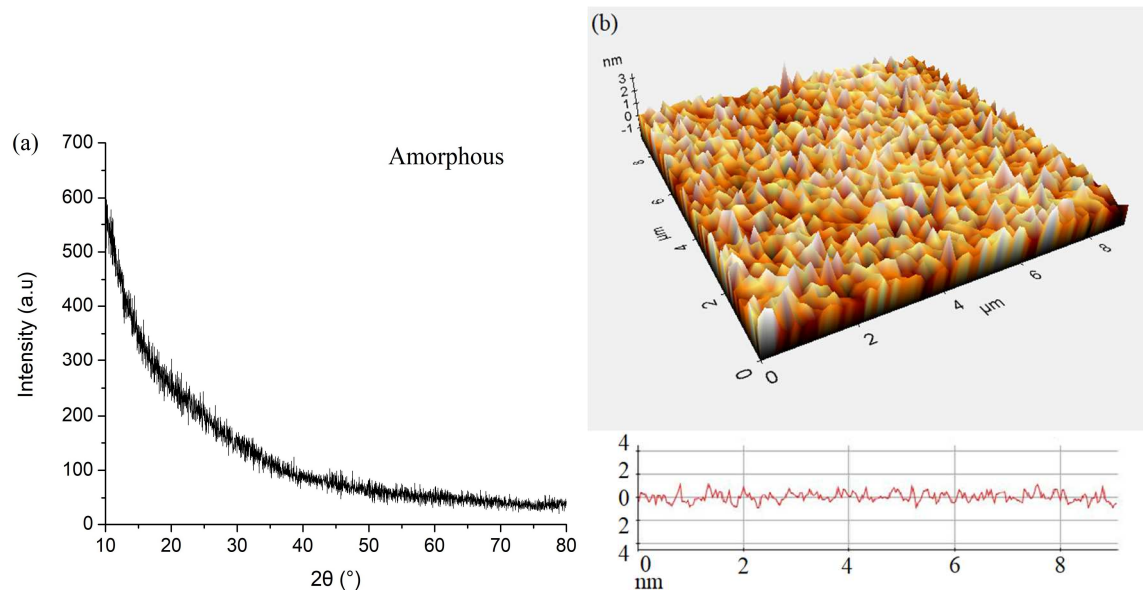
Figure 4.8. (a) XRD spectrum of a 500-nm Al_2O_3 film and (b) AFM image of an 80-nm Al_2O_3 film. Both films were deposited at 550˚C followed by post annealing in nitrogen at 550˚C for 1 hr.

4.8 Chemical Compositional of Al_2O_3

The chemical composition of spray-deposited Al_2O_3 was evaluated by XPS. Fig. 4.9 shows an XPS spectrum of an 80-nm Al_2O_3 film. Only Al, O, and C are detected in the sample. The ratio of Al to O is 1:1.28, while stoichiometric Al_2O_3 has an Al to O ratio of 1:1.5. This suggests that spray-deposited Al_2O_3 is slightly Al rich and can be represented as Al_2O_{3-x}. A small amount of C, 5.5%, was detected by XPS, which is likely due to the organic precursor used in this work.
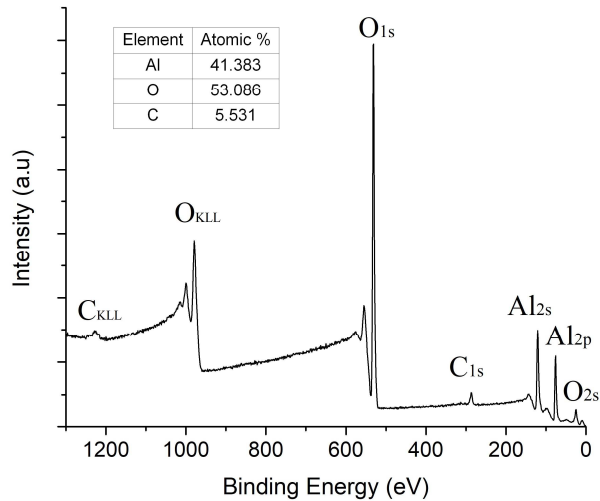
Figure 4.9. XPS spectrum of an 80-nm Al$_2$O$_3$ film deposited at 550˚C on Si followed by post annealing in nitrogen at 550˚C for 1 hr.

4.9 I-V Characteristics of Spray-Deposited Al$_2$O$_3$ and ALD Al$_2$O$_3$/PECVD SiN$_x$

Fig. 4.10 compares the I-V characteristics of 80-nm spray-deposited Al$_2$O$_3$ and 10-nm ALD Al$_2$O$_3$/80-nm PECVD SiN$_x$. The substrates used for I-V were p-type polished CZ Si(100) wafers of 0.001 Ω-cm as the substrate serves as the bottom electrode in I-V characterization. Al dots with an area of 5.54×10^{-3} cm^2 were deposited on each sample by electron-beam evaporation. As shown in Table 4.2, the resistivity and breakdown field of spray-deposited Al$_2$O$_3$ is 5.46×10^{14} Ω-cm and 3.28 MV/cm, respectively. These values are lower compared to 10-nm ALD Al$_2$O$_3$/80-nm PECVD SiN$_x$ but, considering that the open-circuit voltage of Si solar cells is about 0.7 V, the leakage current through 80-nm spray-deposited Al$_2$O$_3$ becomes negligible.

41
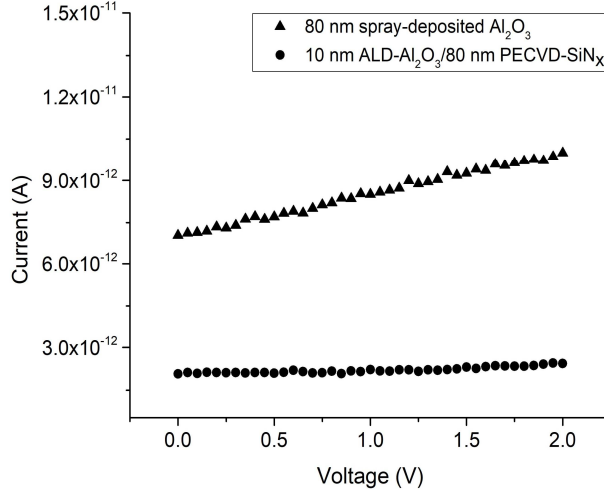
Figure 4.10. Comparison of I-V characteristics between 80-nm spray-deposited Al_2O_3 and

10-nm ALD Al_2O_3/80-nm PECVD SiN_x.

Table 4.2

Resistivity and breakdown field of 80-nm spray-deposited Al_2O_3 and 10-nm ALD

Al_2O_3/80-nm PECVD SiN_x

	Resistivity (Ω-cm)	Breakdown field (MV/cm)
80-nm spray-deposited Al_2O_3	5.46×10^{14}	3.28
10-nm ALD Al_2O_3/80-nm PECVD SiN_x	3.07×10^{15}	3.53

4.10 Summary

The possibility of using low-cost spray-deposited Al_2O_3 for rear passivation and optical

trapping in Si PERC cells is investigated. Optical, electrical, and structural properties of

spray-deposited Al_2O_3 films are examined and compared to the industrial standard ALD

Al_2O_3/PECVD SiN_x stack. It was found that spray-deposited Al_2O_3 has a negative charge

density of 3.19×10^{12} cm^{-2} for an 80-nm film, indicating that spray-deposited Al_2O_3 can

serve as the passivation layer. Optical properties of spray-deposited Al_2O_3 are identical to the ALD Al_2O_3/PECVD SiN_x stack, suggesting that spray-deposited Al_2O_3 can also serve as the optical trapping layer. It was also found that spray-deposited Al_2O_3 is crack and pore free, and its surface roughness has a root-mean-square value of 0.52 nm for an 80-nm film. Spray-deposited Al_2O_3 is amorphous and its composition is slightly Al rich. The resistivity and breakdown field of 80-nm spray-deposited Al_2O_3 are 5.46×10^{14} Ω-cm and 3.28 MV/cm, respectively. These properties suggest that spray-deposited Al_2O_3 is a promising candidate to replace the Al_2O_3/SiN_x stack in Si PERC cells.

CHAPTER 5

LOW-COST SRPAY-DEPOSITED ZRO$_2$ FOR ANTIREFLECTION IN SI SOLAR

CELLS

5.1 Introduction

Si solar cells account for 95% of the current photovoltaic market, but the high production

cost remains a barrier to their wider adoption [36]. Major industrial efforts are being made

to continuously reduce the production cost while improving their power conversion

efficiency. Apart from other components in Si solar cells, the antireflection coating (ARC)

is an important part that reduces the reflection at the front surface of the solar cell, thereby

coupling more sunlight into the cell to increase the photocurrent and efficiency [37].

Several highly-transparent and high refractive-index materials have been investigated as

the ARC material in Si solar cells such as ZnS (n = 2.3) [38], CeO$_2$ (n = 2.2–2.4) [39],

TiO$_2$ (n = 2.3) [40], Ta$_2$O$_5$ (n = 2.1–2.3) [41], and ZnO (n = 2) [42], either in a single-layer

or multiple-layer coating. Among various materials for ARC, SiN$_x$ remains the material of

choice to this day for several reasons: (1) it is highly transparent with a refractive index of

2.0 at 600 nm [43]; (2) it has a large bandgap of 5.1 eV so there is little absorption between

300 nm and 1150 nm where Si solar cells operate [44]; and (3) it has a high density of

positive fixed charges providing good surface passivation on the n-type emitter in Si solar

cells [45].

In general, ARCs with uniform thickness and good optical properties are synthesized by

vacuum-based processes such as physical vapor deposition including thermal evaporation

or reactive sputtering and chemical vapor deposition including plasma-enhanced chemical

vapor deposition (PECVD) and atomic layer deposition [46]. The SiN$_x$ ARC in commercial

44

Si solar cells is prepared by PECVD [44]. Although these vacuum-based processes provide good power conversion efficiencies for Si cells, they hinder a continuous, open-air ARC process for mass production of Si solar cells at a lower cost. Therefore, it is desirable to find an alternative material for the ARC in Si solar cells that is low cost, earth-abundant, and suitable for an open-air continuous process.

In this work, we report spray deposition of ZrO_2 as a potential candidate to replace PECVD SiN_x in Si solar cells as the ARC. Spray deposition is simple, versatile, low cost, and high throughput, a process suitable for continuous open-air synthesis of metal oxides. Zr is an earth-abundant metal with a known reserve of 74 million metric tons [47], sufficient for terawatt-scale production of Si solar cells [48]. The optical properties of ZrO_2, at the first glance, are appropriate as the ARC on Si solar cells [49]. The bandgap of cubic ZrO_2 is 6.1 eV [50] and the refractive index of spray-deposited ZiO_2 is 2.0 at 600 nm which is the same as PECVD SiN_x [49]. However, a detailed study of ZrO_2 for antireflection and surface passivation in Si solar cells has not appeared. In this chapter, we report optical, electrical, and structural properties of spray-deposited ZrO_2 and compare them to PECVD SiN_x to reveal the suitability of ZrO_2 for antireflection in Si solar cells.

5.2 Experimental

Crystalline and amorphous ZrO_2 films were obtained by spray deposition in air. The precursor solution was prepared with 0.2 M zirconium acetylacetonate, $Zr(C_5H_7O_2)_4$ dissolved in methanol, CH_3OH. Pulsed spray deposition was employed for ZrO_2 films, with each cycle comprised of 10 s on and 50 s off. As a hotplate was used to maintain the substrate temperature in our setup, pulsed deposition reduces the fluctuations in substrate temperature and provides ample time for solvent to evaporate. Deposition parameters such

45

as solution flow rate, carrier gas flow rate, and distance between spray nozzle and substrate were optimized to obtain ZrO_2 films with uniform thickness across the entire substrate. The process parameters for optimized ZrO_2 deposition are listed in Table 5.1.

Table 5.1

Optimized parameters for spray deposition of ZrO_2 films

Nozzle-substrate distance (cm)	50
Zr concentration (M)	0.2
Solution flow rate (ml/cycle)	1
Carrier gas	Air
Atomization/piston pressure (pa)	35/40
Substrate temperature (˚C)	450–550

The substrates used in this work were soda lime glass slides and Si wafers with different resistivities. For current-voltage (I-V) characterization of ZrO_2 and SiN_x films, low-resistivity p-type Si(100) wafers of 0.001 Ω-cm were used, which serve as the bottom electrode. For minority carrier lifetime measurements, both n-type and p-type Si(100) wafers of 1 Ω-cm were used. ZrO_2 films deposited on glass substrates were used to characterize structural and optical properties of the films; and those on Si substrates were used to characterize optical and electrical properties. The glass substrates were ultrasonically cleaned with acetone, methanol, and water. Si substrates were cleaned with diluted HF to remove native oxide from the surface. For comparison, 75-nm SiNx films were also deposited on glass and Si substrates in PECVD at 200˚C using a mixture of SiH_4

46

and NH$_3$. The recipe for PECVD SiN$_x$ is adopted from recipes commonly used in the industry.

5.3 Optical Properties of Spray-Deposited ZrO$_2$ and PECVD-SiN$_x$

The refractive index of the ARC is one of the most important parameters for antireflection in Si solar cells. The optimum refractive index for a single-layer ARC can be calculated using the following equation:

$$n_{ARC} = \sqrt{n_{Si} n_{Glass}} \quad (5.1)$$

assuming that the ARC is sandwiched between Si wafer and glass. Glass has a typical refractive index of 1.4 and the refractive index of Si is 3.9 at 600 nm, so the optimum refractive index for the ARC is 2.34. This suggests that the refractive index of SiN$_x$, 2.0, is slightly below the optimum value and a high-index material is preferred for the ARC in Si solar cells.

Figure 5.1 presents the measured refractive index of 75-nm spray-deposited ZrO$_2$ films at different deposition temperatures as a function of wavelength. The refractive index of spray-deposited ZrO$_2$ increases with deposition temperature. Its value at 600 nm changes from 1.934 to 2.002 as the deposition temperature increases from 450˚C to 550˚C. A similar trend was also observed in ZrO$_2$ films prepared by pulsed laser deposition [51]. The refractive index of spray-deposited ZrO$_2$ is lower than the refractive index of bulk ZrO$_2$, 2.15 at 600 nm, presumably due to the lower density of the spray-deposited ZrO$_2$. At 550˚C, the index of ZrO$_2$ at 600 nm is similar to that of PECVD SiN$_x$, 2.002±0.00189 for ZrO$_2$ vs. 2.007±0.00213 for SiN$_x$. These values were obtained with the WVASE32 software. The difference in refractive index is much smaller at long wavelengths but becomes noticeable at short wavelengths between SiN$_x$ and 550˚C ZrO$_2$.
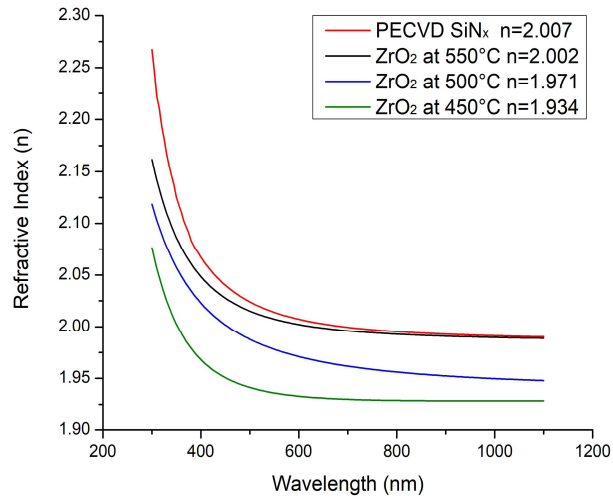
Figure 5.1. Comparison of refractive index between PECVD SiN$_x$ and spray-deposited ZrO$_2$ prepared at different deposition temperatures.

Antireflection relies on quarter-wavelength destructive interference. For a film of a transparent material with a refractive index n and thickness d, the wavelength λ at which zero reflection occurs is calculated by:

$$d = \lambda/4n \ (5.2)$$

where λ is the wavelength of the normal-incidence light in vacuum. For solar cell applications, the refractive index and thickness of the ARC are designed to minimize the reflection at 600 nm. This wavelength is close to the maximum power point of the solar spectrum. Since ZrO$_2$ and SiN$_x$ both have a refractive index of 2.0, they require the same thickness of 75 nm to have the minimum reflection at 600 nm. Fig. 5.2 compares a 75-nm SiN$_x$ prepared by PECVD and a 75-nm ZrO$_2$ prepared by spray deposition on Si substrates. They both show the same blue color which indicates they have a similar refractive index.
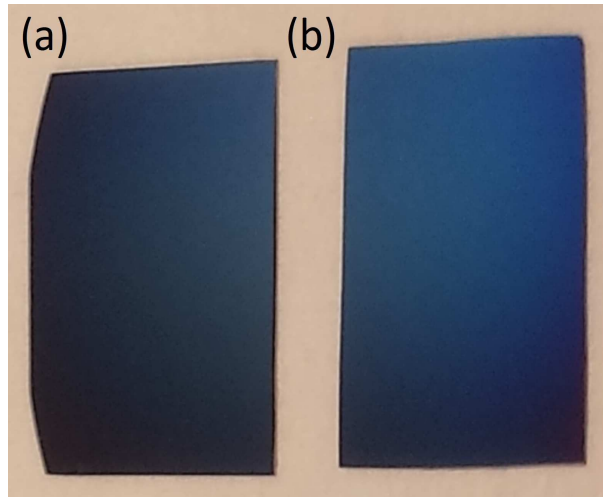
Figure 5.2. Photo of (a) 75-nm SiN$_x$ by PECVD and (b) 75-nm ZrO$_2$ by spray deposition.
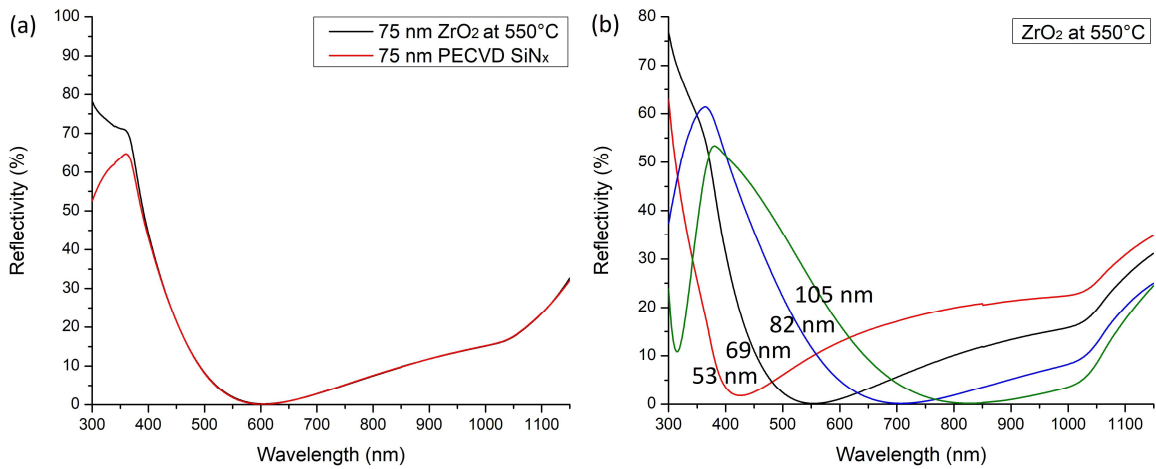
Figure 5.3. (a) Comparison of reflection between PECVD SiN$_x$ and spray-deposited ZrO$_2$ on Si substrates. (b) Reflection of ZrO$_2$ films on Si substrates with different thicknesses.

Reflection spectra of Si substrates covered with PECVD SiN$_x$ and spray-deposited ZrO$_2$ are provided in Fig. 5.3(a). The ZrO$_2$ film was deposited at 550˚C. A 75nm film of SiN$_x$

and a 75nm film of ZrO_2 on Si substrates result in the same minimum reflection point at 600 nm. This confirms that they have the same refractive index of 2.0. Below 400 nm, ZrO_2 has slightly higher reflection than SiN_x, but they are similar at long wavelengths. Both refractive index and reflection are dependent on wavelength. Therefore, the difference in reflection below 400 nm is likely due to the greater difference in refractive index between SiN_x and 550°C ZrO_2 below 400 nm as revealed in Fig. 5.1. Fig. 5.3(b) shows reflection spectra of Si substrates covered with ZrO_2 films of different thicknesses from 53 nm to 105 nm. The minimum reflection point shifts towards higher wavelengths as film thickness increases. This relationship is predicted by Eq. (5.2) and is also observed in SiN_x films of different thicknesses.

Since the number of photons determine the maximum number of electron-hole pairs that can be generated in a solar cell, the difference in reflection between SiN_x and ZrO_2 in Fig. 5.3(a) was converted into the difference in reflected photon flux. Fig. 5.4(a) shows the incident photon flux at AM1.5 as a function of wavelength. The total number of photons with energy above the Si bandgap was found to be 2.75×10^{21} $m^{-2}s^{-1}$, which was calculated by integrating the area under the photon flux curve from 0 nm and 1112 nm, the cutoff wavelength for Si at 48°C. Fig. 5.4(b) plots the difference in reflected photon flux between SiN_x and 550°C ZrO_2 based on Fig. 5.3(a). This was calculated by multiplying the change in reflection in Fig. 5.3(a) with the incident photon flux at each wavelength:

$$\Delta\Phi_{Reflected}(\lambda) = [R_{ZrO_2}(\lambda) - R_{SiN_x}(\lambda)] \times \Phi_{Incident}(\lambda) \text{ (5.3)}$$

where $\Delta\Phi_{Reflected}(\lambda)$ is the change in reflected photon flux and $\Phi_{Incident}(\lambda)$ is the incident photon flux from Fig. 5.4(a), both of which are wavelength dependent. As shown in Fig. 5.4(b), positive values indicate a net loss in reflection by ZrO_2 over SiN_x and negative

values are desirable. Integrating the change in reflected photon flux over wavelength reveals that ZrO_2 reflects a net of $5.19 \times 10^{18}\,\text{m}^{-2}\text{s}^{-1}$ more photon than SiN_x on Si substrates. This is less than 0.2% of the total number of photons in the AM1.5 solar spectrum which has energy above the Si bandgap, which is within margin of error. Therefore, ZrO_2 is optically comparable to SiN_x.
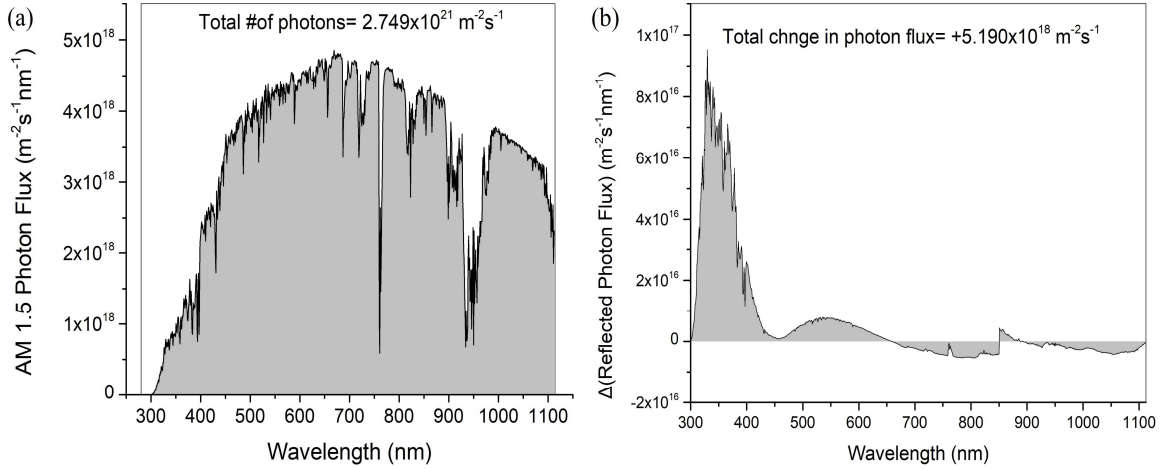
Figure 5.4. (a) Photon flux in the AM1.5 solar spectrum as a function of wavelength. (b) Change in reflected photon flux between ZrO_2 and SiN_x as a function of wavelength.

Figure 5.5(a) compares the transmission between SiN_x and 550°C ZrO_2 on glass substrates. The thickness of both films was 75 nm. At long wavelengths, SiN_x has slightly higher transmission, but ZrO_2 has higher transmission below 570 nm. The difference in transmission between SiN_x and ZrO_2 was converted into the difference in transmitted photon flux as shown in Fig. 5.5(b):

$$\Delta\Phi_{Transmitted}(\lambda) = [T_{ZrO_2}(\lambda) - T_{SiN_x}(\lambda)] \times \Phi_{Incident}(\lambda) \quad (5.4)$$

where $\Delta\Phi_{Transmitted}(\lambda)$ is the change in transmitted photon flux. In this case positive values are desirable. Integrating the curve over wavelength indicates that ZrO_2 transmits

2.54×10^{19} m^{-2}s^{-1} fewer photons than SiN$_x$. This accounts for less than 1% of the total number of photons in the AM1.5 solar spectrum with energy above the Si bandgap, which is within margin of error. Again, ZrO$_2$ is optically comparable to SiN$_x$.
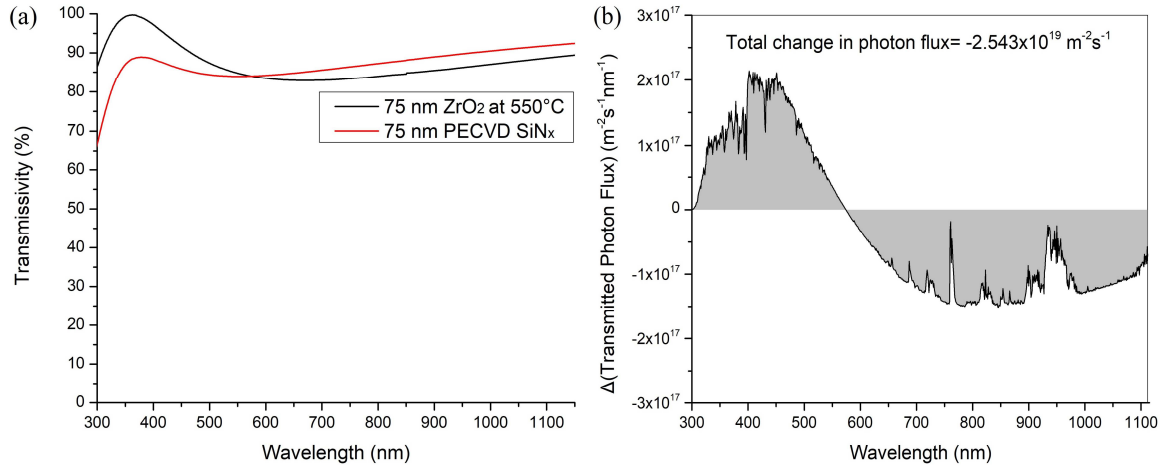
Figure 5.5. (a) Comparison of transmission between of PECVD SiN$_x$ and spray-deposited ZrO$_2$ on glass substrates. (b) Change in transmitted photon flux as a function of wavelength.

5.4 X-Ray Diffraction and Surface Roughness of ZrO$_2$
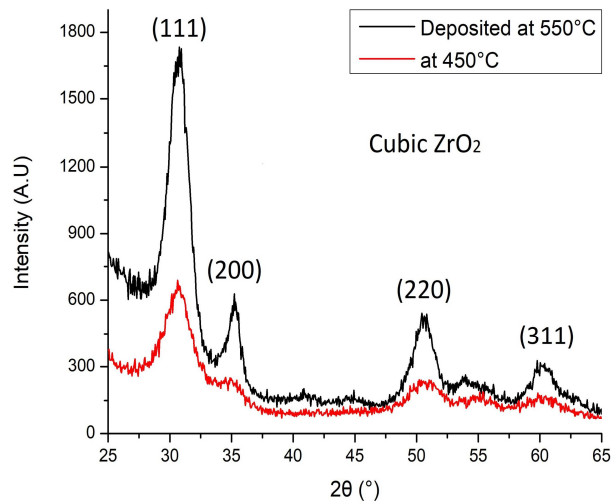
Figure 5.6. XRD spectra of 75-nm ZrO_2 films deposited at two temperatures, 450˚C and 550˚C. Spray-deposited ZrO_2 has a cubic structure.

XRD spectra of 75-nm ZrO_2 films deposited at two temperatures, 450˚C and 550˚C, are presented in Fig. 5.6. ZrO_2 can appear in three phases: cubic, tetragonal, or monoclinic. Fig. 5.6 indicates that spray-deposited ZrO_2 is cubic, and no other phases of ZrO_2 are detected in XRD. The four peaks in Fig. 5.6 are identified as cubic $ZrO_2(111)$, (200), (220), and (311), respectively, with (111) as the strongest peak. The ZrO_2 film is more amorphous at 450˚C but becomes crystalline at 550˚C.

AFM was used to examine the surface morphology and roughness of spray-deposited ZrO_2 films. Fig. 5.7 shows an AFM scan of a ZrO_2 film deposited at 550˚C and with a thickness of 75 nm. The scan area in this figure is 9×9 μm^2. At 550˚C, the film appears polycrystalline with a grain size of roughly 100 nm. It is crack-free and pore-free. The surface roughness of the polycrystalline ZrO_2 film is low, in the range of ±2 nm as shown in the profile scan. The root mean square surface roughness is found to be 0.7 nm for the 75-nm film.
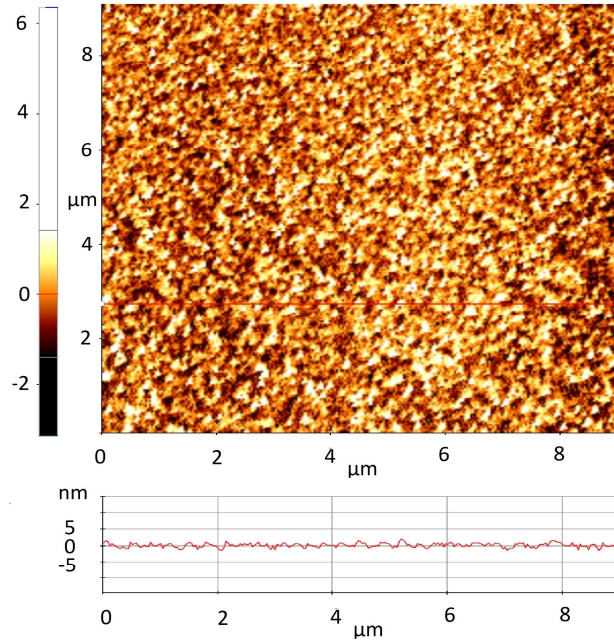
Figure 5.7. AFM image of a 75-nm ZrO$_2$ film deposited at 550˚C on a Si substrate. The

profile scan at bottom shows the surface roughness.

5.5 C-V Characteristics of ZrO$_2$

In order to determine the density of fixed charges in ZrO$_2$ films, C-V characterization

was carried out. The substrates used in this work were p-type Si(100) wafers of 0.5 Ω-cm.

The ZrO$_2$ film was deposited at 550˚C with a thickness of 75 nm. Fig. 5.8 shows the C-V

characteristics measured at a frequency of 100 kHz. To determine the intrinsic charge in

the ZrO$_2$ film, C-V was performed in a small voltage range between −1 V and 1.5 V. The

accumulation capacitance, which is the oxide capacitance, C$_{ox}$, is 712 pF. This translates

into a dielectric constant of 13.2 for ZrO$_2$ as calculated from the contact area of the Hg

probe (0.456 mm^2) and the oxide thickness (75 nm). This value is close to CVD ZrO$_2$ [52].

A flat-band capacitance of 311 pF was calculated, and a flat-band voltage of +0.35 V

obtained from the C-V curve. To determine the density of fixed charges in ZrO_2, the workfunction difference between Hg probe and Si, $\Delta\phi_{MS}$, was calculated by:

$$\Delta\phi_{MS} = \phi_M - \chi_{Si} - (E_C - E_F) \quad (5.5)$$

A workfunction difference of -0.49 eV was calculated from the workfunction of Hg, ϕ_M = 4.5 eV, the electron affinity of Si, χ_{Si} = 4.05 eV, and the position of the Fermi level in Si, $E_C - E_F$ = 0.94 eV, for 0.5 Ω-cm p-type Si. The density of fixed charges in ZrO_2, Q_f, was then determined by:

$$Q_f = (\Delta\phi_{MS} - V_{FB}) \times C_{ox}/A \quad (5.6)$$

where V_{FB} is the flat-band voltage and A the contact area of the Hg probe. The calculated density of fixed charges in the 550˚C-deposited 75-nm ZrO_2 film is -8.19×10^{11} cm^{-2}. The density of fixed charges is low compared to Al_2O_3 which has a fixed charge density of 10^{13} cm^{-2} for a 20-nm film [53]. The negative sign suggests that ZrO_2 may be able to serve for surface passivation on p-type Si.
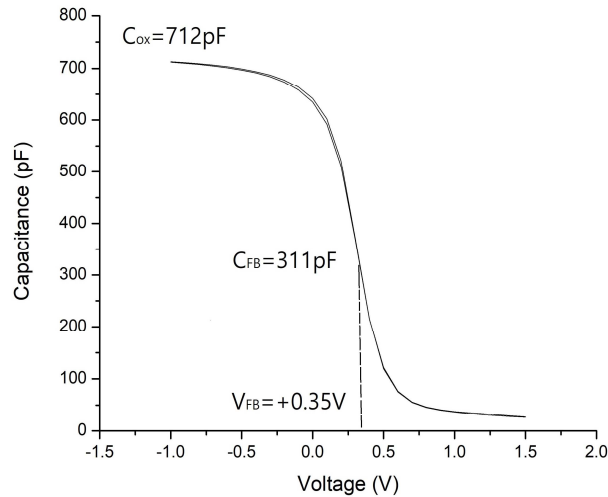
Figure 5.8. C-V characteristics of a 75-nm ZrO_2 film deposited at 550˚C. The density of fixed charges in 75nm ZrO_2 is -8.19×10^{11} cm^{-2}.

5.6 Effective Minority Carrier Lifetime of Si Covered with ZrO₂

The passivation effect of ZrO_2 on Si was examined by measuring the minority carrier lifetime of Si wafers covered with ZrO_2 on both sides. The Si wafers used in this work were p-type and n-type textured wafers of 1 Ω-cm. The final thickness of the wafers after texturing was 180 μm. The sample size was 4×4 cm². After removal of native oxide in diluted HF, ZrO_2 of different thicknesses was deposited on both sides of the wafers at 550˚C. As shown in Fig. 5.9, the minority carrier lifetime increases with ZrO_2 thickness. With 75-nm ZrO_2, the minority carrier lifetime of p-type and n-type Si measures out to be 17.3 μs and 26.7 μs, respectively. As a reference, the starting Si wafers had a minority carrier lifetime of 2 μs. The low lifetime with ZrO_2 coating is due to the low density of fixed charges present in ZrO_2, -8.19×10^{11} cm^{-2}, as well as the low lifetime in the starting wafers. Further annealing in air or nitrogen at different conditions did not improve the lifetime.
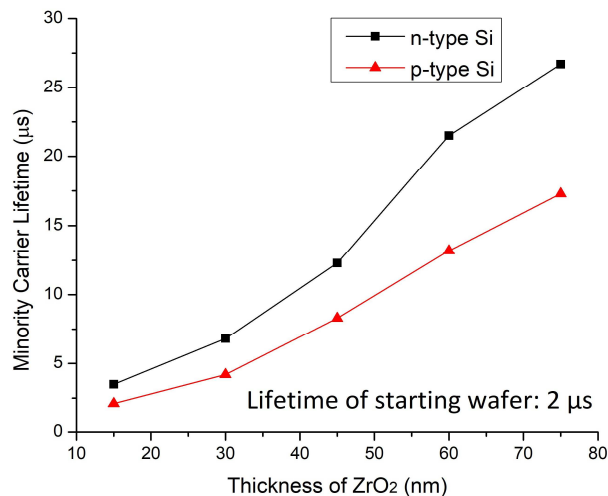
Figure 5.9. Minority carrier lifetime of p-type and n-type Si wafers covered with ZrO_2 of different thicknesses on both sides.

56

5.7 I-V Characteristics of ZrO$_2$ and PECVD SiN$_x$

The leakage current through spray-deposited ZrO$_2$ and PECVD SiN$_x$ was measured by I-V characterization as shown in Figure 5.10. The substrates used in this work were p-type Si(100) wafers of 0.001 Ω-cm as the substrate serves as the bottom electrode. Al dots were deposited on 75-nm SiN$_x$ and ZrO$_2$ by e-beam evaporation. The area of the Al dots was 5.54×10^{-3} cm^2. The resistance of each film, R, was calculated from the I-V characteristics, and the resistivity of each film, ρ, was obtained using the following equation:

$$\rho = RA/l \quad (5.7)$$

where A is the area of the Al dots, 5.54×10^{-3} cm^2, and l the thickness of the dielectric, 75 nm. As listed in Table 5.2, the resistivity of as-deposited 75-nm ZrO$_2$ is 3.69×10^{12} Ω-cm. While the value is respectable, it is approximately three orders of magnitude lower than that of SiN$_x$. After post-deposition annealing in air at 500˚C and 600˚C for 1 h, the resistivity of ZrO$_2$ increases to 9.23×10^{12} Ω-cm and 2.46×10^{13} Ω-cm, respectively. The breakdown field of as-deposited 75-nm ZrO$_2$ is 1.47 MV/cm. Upon post-deposition annealing in air at 500˚C and 600˚C for 1 h, the breakdown field increases to 1.73 MV/cm and 1.95 MV/cm, respectively. The increased resistivity and breakdown field are likely due to the SiO$_2$ layer formed between ZrO$_2$ and Si upon post annealing.
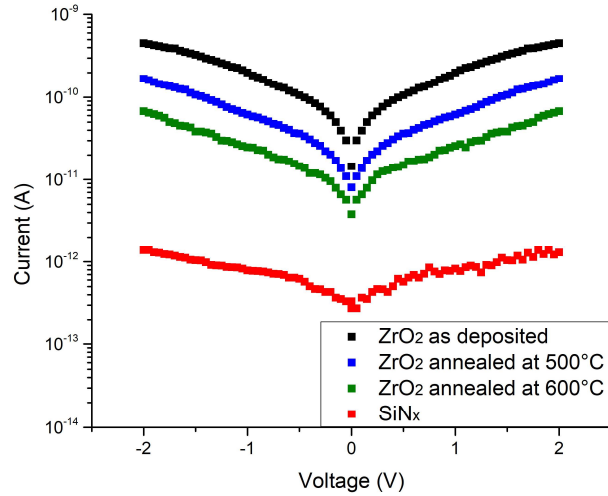
Figure 5.10. Comparison of I-V characteristics between PECVD SiN_x and as-deposited

and post-annealed ZrO_2 at different temperatures.

Table 5.2

Resistivity and breakdown field of PECVD SiN_x and spray-deposited ZrO_2

	Resistivity (Ω-cm)	Breakdown field (MV/cm)
PECVD SiN_x	1.48×10^{15}	2.78
As-deposited ZrO_2	3.69×10^{12}	1.47
ZrO_2 annealed in air at 500˚C for 1 h	9.23×10^{12}	1.73
ZrO_2 annealed in air at 600˚C for 1 h	2.46×10^{13}	1.95

5.8 Manipulating Fixed Charges in ZrO_2 by Doping

As-deposited ZrO_2 has negative fixed charges with a density of -8.19×10^{11} cm^{-2} for a 75-nm film, which is low for effective field-induced surface passivation on p-type Si. Therefore, doping in ZrO_2, i.e. introducing a second metal into ZrO_2, was attempted to manipulate the density of fixed charges for more effective surface passivation on p-type Si. Table 5.3 lists the metal dopants we tried and their effect on fixed charges. Most of the dopants we tried have no effect on fixed charges. The most effective dopant is Cr. With Cr-doped ZrO_2, a positive flat-band voltage shift was observed which indicates an increase in negative charge density in ZrO_2. As shown in Fig. 5.11, the magnitude of the flat-band shift is strongly dependent on doping concentration and post-deposition annealing temperature. Fig. 5.11(a) shows the effect of doping concentration on flat-band shift. The amount of positive flat-band shift increases linearly with Cr concentration from 1% to 4%. Further increase in Cr concentration above 4% did not result in a larger flat-band shift. The maximum flat-band shift of +1.11 V was observed with 4% Cr concentration after rapid thermal annealing of as-deposited Cr-doped ZrO_2 at 750˚C for 1 min. Under these conditions, the flat-band voltage was calculated to be +1.46 V and the density of negative charges -1.32×10^{12} cm^{-2}, still too low for effective surface passivation.

Table 5.3. Summary of attempted metal dopants in spray-deposited ZrO_2

Dopant	Flat-band voltage shift
Cr	+1.11V
Mn	+0.5V
V	No

Zn	No
Y	No
Ni	No

Figure 5.11(b) shows the effect of annealing temperature on flat-band shift and oxide capacitance. Cr concentration for all the samples was fixed to 4% and the thickness of the ZrO_2 films was 75 nm. The maximum flat-band shift is observed at 750˚C. At 800˚C and 850˚C the flat-band shift is smaller than at 750˚C. In addition to flat-band shift, the oxide capacitance significantly decreases after post annealing. The oxide capacitance for as-deposited 4% Cr-doped ZrO_2 is 720 pF. After 850˚C annealing, the oxide capacitance is reduced to 509 pF. It is well known that annealing a metal oxide/Si stack results in the formation of SiO_2 at the interface [54]. As the dielectric constant of SiO_2 is only 3.8, far below that of ZrO_2, the oxide capacitance decreases as SiO_2 thickens with post-annealing temperature.
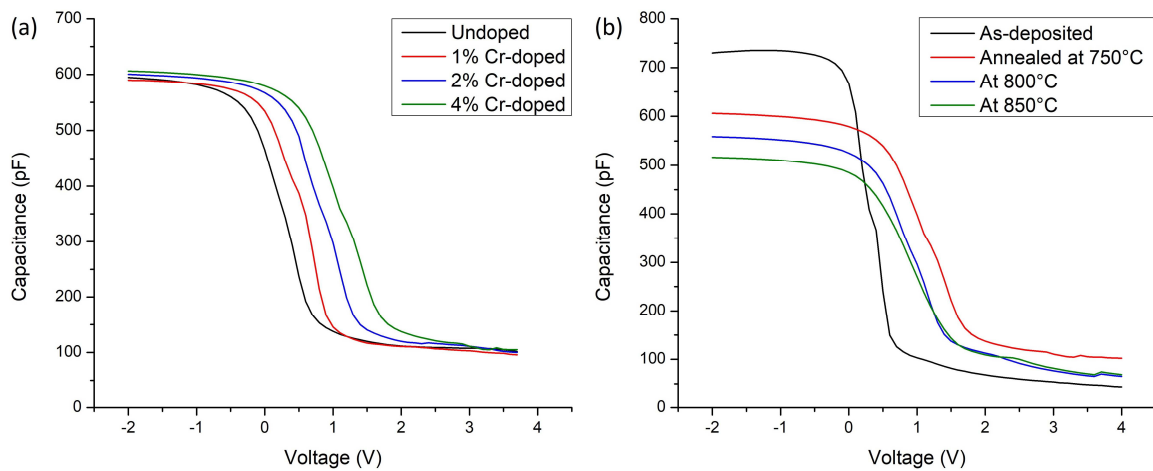
Figure 5.11. (a) C-V of undoped and Cr-doped 75-nm ZrO$_2$ after post annealing at 750˚C for 1 min. (b) C-V of 4% Cr-doped 75-nm ZrO$_2$ after post annealing at different temperatures from 750˚C to 850˚C.

To verify that the decrease in oxide capacitance in Fig. 5.11(b) was not caused by Cr doping but by interfacial SiO$_2$ formation, post-deposition annealing was performed on undoped ZrO$_2$ films. Fig. 5.12(a) shows the effect of post-annealing temperature on oxide capacitance in undoped ZrO$_2$. A similar decrease in oxide capacitance with annealing temperature is observed, and undoped ZrO$_2$ does not show any flat-band shift. Fig. 5.12(b) further confirms the hypothesis of interfacial SiO$_2$. The refractive index of ZrO$_2$ after post annealing decreases with annealing temperature, as the refractive index of SiO$_2$ is lower than ZrO$_2$, 1.46 vs 2.15 at 600 nm. The values of refractive index were obtained using the Cauchy model. The thickness of the SiO$_2$ layer formed at the ZrO$_2$/Si interface can be estimated in two different ways using the following equations:

$$1/C_{ox} = 1/C_{ox(ZrO_2)} + 1/C_{ox(SiO_2)} \quad (5.8)$$

$$n = n_{ZrO_2} \times t_{ZrO_2}/(t_{ZrO_2} + t_{SiO_2}) + n_{SiO_2} \times t_{SiO_2}/(t_{ZrO_2} + t_{SiO_2}) \quad (5.9)$$

where C$_{ox}$ and n are the measured oxide capacitance and refractive index. The thickness of ZrO$_2$ and the refractive index of SiO$_2$ are assumed to be 75 nm and 1.46, respectively. Table 5.4 lists the calculated SiO$_2$ thickness at different post-annealing temperatures. As expected, the SiO$_2$ thickness increases with annealing temperature, and the thicknesses calculated by the two methods agree well with each other.

To investigate the effect of Cr doping on optical properties of ZrO$_2$, the refractive index of undoped ZrO$_2$ and 4% Cr-doped ZrO$_2$ after post annealing are compared in Fig. 5.13.

The refractive index of 4% Cr-doped ZrO_2 at 600 nm is 2.162. This value is higher than undoped ZrO_2 and is closer to the optimum value (n=2.34) for the ARC in Si solar cells. The refractive index of Cr_2O_3 is 2.4–2.6 [55]. Therefore, the increase in refractive index is attributed to the introduction of Cr into ZrO_2.
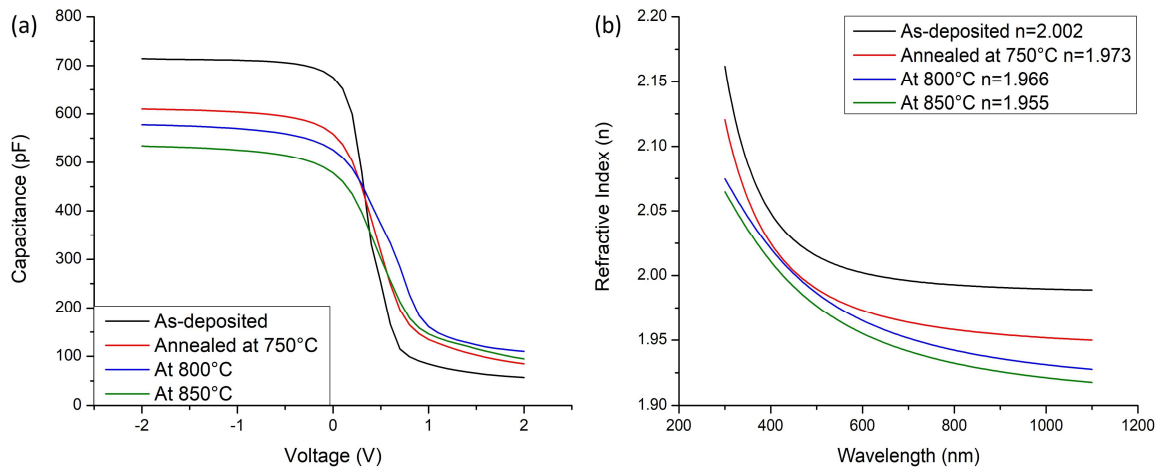
Figure 5.12. (a) C-V and (b) refractive index of 75-nm ZrO_2 after post-annealing in air at different temperatures from 750˚C to 850˚C. Post-annealing time was 1 min.

Table 5.4. Calculated SiO_2 thickness at different post-annealing temperatures

Temperature (˚C)	C_{ox} (pF)	t_{SiO2} by C_{ox} (nm)	n	t_{SiO2} by n (nm)
As-deposited	712	-	2.002	-
750˚C	602	3.94	1.973	4.24
800˚C	575	5.13	1.966	5.34
850˚C	528	7.51	1.955	7.12
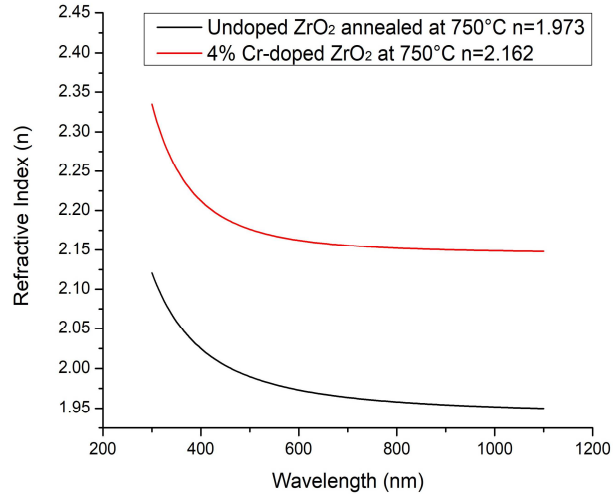
Figure 5.13. Refractive index of undoped 75-nm ZrO_2 and 4% Cr-doped 75-nm ZrO_2 after post annealing in air at 750˚C. Post-annealing time was 1 min.

5.9 Summary

The possibility of using low-cost spray-deposited ZrO_2 as the antireflection coating for Si solar cells is investigated. Optical, electrical, and structural properties of spray-deposited ZrO_2 are studied and compared to PECVD SiN_x. The results show that spray-deposited ZrO_2 has a refractive index of 2.0 at 600 nm which is similar to that of SiN_x. Reflection and absorption losses in spray-deposited ZrO_2 are comparable to SiN_x. As-deposited ZrO_2 films are crack/pore-free and have a smooth surface with a root-mean-square roughness of 0.7 nm for a 75-nm film. When deposited at 450˚C, the ZrO_2 film is largely amorphous. At 550˚C deposition temperature, the ZrO_2 film becomes polycrystalline with a cubic lattice. A density of negative fixed charges of 8.19×10^{11} cm^{-2} is calculated for a 75-nm ZrO_2 film. Doping ZrO_2 with Cr shows a significant positive flat-band indicating an increase in negative fixed charge density. Post-deposition annealing of ZrO_2 results in a significant decrease in oxide capacitance which is attributed to the formation of SiO_2 at the ZrO_2/Si

interface. The resistivity of as-deposited ZrO_2 is 3.69×10^{12} Ω-cm and it improves to 2.46×10^{13} Ω-cm after post-deposition annealing in air at 600˚C for 1 h.

CHAPTER 6

SULFURIZATION OF HEMATITE FE$_2$O$_3$ AND ANATASE TIO$_2$ BY ANNEALING

IN H$_2$S

6.1 Introduction

Hematite Fe$_2$O$_3$ and anatase TiO$_2$ have received growing interests for solar energy

applications such as solar water splitting [56-59] and photovoltaic solar cells [60-63]. They

are nontoxic, low-cost, earth-abundant, and environmentally-friendly, which are necessary

properties for mass production of their devices for solar energy conversion. However, the

realized solar energy conversion efficiencies from devices based on these materials have

been insufficient due to a number of issues, such as poor light absorption, short lifetime of

photo-excited charge carriers, and large bandgaps [64]. On the other hand, pyrite FeS$_2$ and

titanium disulfide TiS$_2$ have demonstrated promising properties for applications in

photovoltaic solar cells [65] and solar water splitting [66]. FeS$_2$ has a smaller bandgap

(0.95 eV indirect), high absorption coefficient ($\alpha > 10^5$ cm^{-1} for hv > 1.3 eV), and sufficient

minority carrier diffusion length (100–1000 nm) [67]. FeS$_2$ solar cells have demonstrated

a high quantum efficiency of 90% and a high photocurrent of 42 mA-cm^{-2} [65]. In solar

water splitting, it possesses excellent stability against photo-corrosion in comparison with

other chalcogenide semiconductors (e.g. CdS or CdSe) [66]. For TiS$_2$, Hall and

thermoelectric power measurements suggest that TiS$_2$ is a semiconductor [68]. TiS$_2$ has

recently been used as the charge transport layer in perovskite solar cells, resulting in a high

cell efficiency of 17.37% because of its high carrier mobility and conductivity [69].

It is well known that for a highly-efficient solar cell, a direct bandgap around 1.4 eV is

highly desirable. For solar water splitting, the optimum bandgap is about 1.7 eV direct. A

65

major disadvantage of TiO_2 is that it is a semiconductor with a wide bandgap of 3.2 eV and thus can only utilize the ultraviolet (UV) portion of the solar spectrum below 388 nm. That portion of the solar spectrum makes up just 4–5% of the energy from sunlight. α-Fe_2O_3 has a slightly-lower bandgap of 2.1 eV which theoretically allows the utilization of approximately 40% of the solar spectrum [70]. Therefore, narrowing the bandgap of these semiconductors to increase visible and infrared (IR) light absorption is crucial to advancing their applications in solar energy conversion.

Alloying or doping, i.e. the introduction of a third element into binary α-Fe_2O_3 and TiO_2, is a common approach to extend the absorption edge into the visible and IR region. In the past decade, cationic doping in α-Fe_2O_3 has been extensively studied both experimentally and theoretically [71-76], while there are few studies involving anionic doping in α-Fe_2O_3. Most of those doping studies aimed to provide extra charge carriers to the material. Only the studies of isovalent substitutional doping by Al attempted to modify the bandgap [77], but no significant change in bandgap was achieved. The experimental studies of N-doped α-Fe_2O_3 found an indirect bandgap of 1.96 eV indicating that N doping barely changes the bandgap of α-Fe_2O_3 [78]. To our knowledge, anionic isovalent doping in α-Fe_2O_3 has not been reported. On the other hand, various transition metals, such as Fe, Cr, Co, Mo, and V, have been employed to tune the electronic structure of TiO_2 [79-82]. However, introducing a second cation into TiO_2 can result in thermal instability and an increase in recombination centers for photo-excited charge carriers by the localized d-states of the transition metal which are deep in the bandgap of TiO_2 [83]. Anionic doping, such as C [84], N [85], and S [86], is more effective in modifying the electronic structure and extending the absorption edge into the visible region. They do not act as recombination centers as they introduce

66

states near the valence band edge [87]. Since their valence electrons (i.e. N 2p, S 3p, and C 2p) have energy higher than that of the O 2p orbital, a higher valence band can be formed in place of the pure O 2p band resulting in a decrease in the bandgap [88].

First-principles studies suggested that substitution of oxygen atoms by sulfur may contribute to bandgap narrowing in α-Fe_2O_3 [89] and TiO_2 [86]. Different methods have been used to prepare S-doped TiO_2 such as sol gel [90-92], oxidation of TiS_2 [93], ion implantation [94], and hydrothermal synthesis [95], but no significant bandgap narrowing was reported. In this chapter, we report our studies on anionic doping in hematite Fe_2O_3 and anatase TiO_2 thin films by annealing them in H_2S atmosphere. When annealed at relatively low temperatures, we found that sulfurization of α-Fe_2O_3 and TiO_2 results in co-existence of multiple phases in the films, instead of a single phase of oxysulfide. At high temperature above 450°C, α-Fe_2O_3 is fully transformed into FeS_2. At 700°C, TiO_2 is completely transformed into TiS_2.

6.2 Preparation of α-Fe_2O_3 and Anatase TiO_2 Thin Films

Hematite Fe_2O_3 thin films were synthesized by open-air spray deposition for its versatility, simplicity, low cost, and high throughput. The substrates used in this work were soda lime glass slides. Prior to deposition, substrates were ultrasonically cleaned with acetone and deionized water, respectively. The precursor solution for spray deposition was a 0.1 M aqueous solution of $FeCl_3$ from Alfa Aesar. Pulsed spray deposition was employed with 10 s on cycle and 50 s off cycle, which reduces the fluctuations in substrate temperature and provides ample time for solvent evaporation. Deposition parameters such as solution flow rate, carrier gas flow rate, and distance between spray nozzle and substrate

were optimized to obtain hematite films with uniform thickness across the entire substrate. The process parameters for α-Fe$_2$O$_3$ film deposition are listed in Table 6.1

Table 6.1

Process parameters for optimized α-Fe$_2$O$_3$ film deposition by pulsed spray pyrolysis

Nozzle-substrate distance	15 cm
Solution flow rate	1 ml/cycle
Carrier gas	air
Atomization pressure	60 Pa
Substrate temperature	500˚C

Anatase TiO$_2$ thin films were prepared on quartz substrates by a sol-gel method under acidic conditions. Prior to deposition, substrates were ultrasonically cleaned with acetone and deionized water, respectively. The TiO$_2$ sol-gel precursor was synthesized by mixing 1.5 mL of Ti isopropoxide (Ti(OCH(CH$_3$)$_2$)$_4$ or TTIP, 97%), 3 mL of acetic acid (CH$_3$COOH, 99.9%), and 3 mL of ethanol (C$_2$H$_5$OH, 99.9%). This solution was added into a solution of 0.45 g of polyvinylpyrrolidone ((C$_6$H$_9$NO)$_n$ or PVP, M$_w$ ~1,300,000) in 7.5 mL of ethanol. The TTIP and PVP were purchased from Sigma Aldrich and the acetic acid and ethanol from J. T. Baker. The final solution was stirred for 1 h using a similar procedure reported by Li et al. [96]. The obtained sol-gel had a light-yellow color and it was spin coated at 2000 rpm onto the quartz substrates. After spin coating, the substrates were dried at 120˚C for 30 min and then annealed at 500˚C for 1 h to form anatase TiO$_2$.

6.3 Characterizations of α-Fe₂O₃ Thin Films

Figure 6.1 shows a SEM micrograph and the total transmittance spectrum of a spray-deposited α-Fe$_2$O$_3$ film on a soda lime glass substrate. The as-prepared α-Fe$_2$O$_3$ film is approximately 60% transparent in the visible region, and highly transparent in the IR region. The SEM micrograph shows that the as-prepared film has pyramid-shaped grains with a grain size of approximately 300 nm. The thickness of the α-Fe$_2$O$_3$ film is about 1 μm. The optical bandgap of α-Fe$_2$O$_3$ is evaluated from the transmittance spectrum using the Tauc relation:

$$\alpha h\nu = C(h\nu - E_g)^n \quad (6.1)$$

where hν is the photon energy, α is the absorption coefficient, C is a constant, E_g is the bandgap of the material, and n is a constant that depends on the type of transition. For n = ½, E_g in Eq. (1) is a direct bandgap transition, while n = 2 is an indirect bandgap transition. The bandgap is estimated from the intercept of the linear portion of the $(\alpha h\nu)^2$ vs hν or $(\alpha h\nu)^{1/2}$ vs hν plots on the hν axis as shown in Fig. 6.2. The estimated bandgap of as-prepared α-Fe$_2$O$_3$ is 2.2 eV for direct transition and 2.0 eV for indirect transition. Fig. 6.2 also suggests that the bandgap of spray-deposited α-Fe$_2$O$_3$ is more likely direct, as Fig. 6.2(a) displays a nice linear portion with a clear intercept with the hν axis.
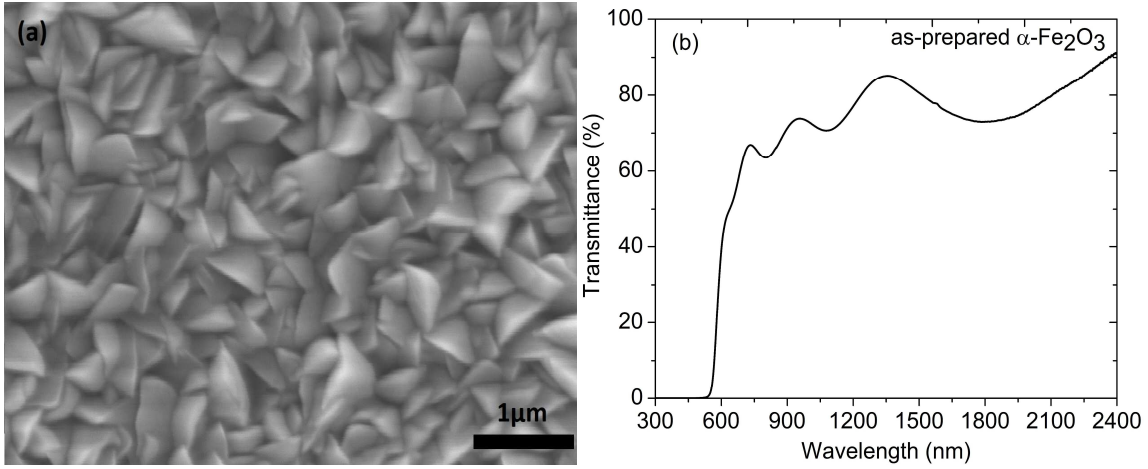
Figure 6.1. (a) Morphology by SEM and (b) transmittance spectrum by spectrophotometry of as-prepared α-Fe$_2$O$_3$.
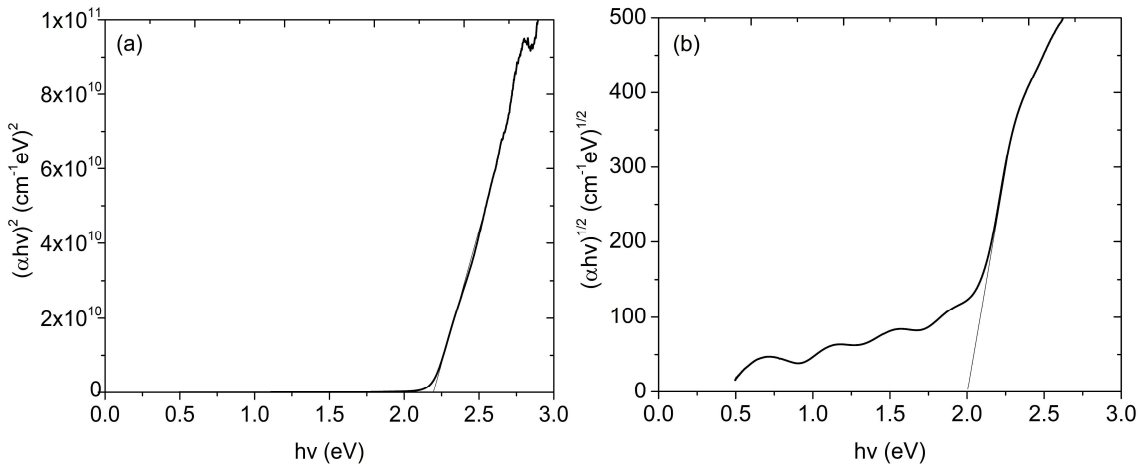
Figure 6.2. (a) Direct and (b) indirect bandgap calculations of a spray-deposited α-Fe$_2$O$_3$ film using Tauc's plots.

The crystal structure of a spray-deposited α-Fe$_2$O$_3$ film was confirmed by XRD as shown in Fig. 6.3. All the peaks coincide with those of hematite, with a preferred crystal

70

orientation along the (104) direction. Peaks associated to other phases of Fe oxides such as magnetite (Fe_3O_4), maghemite (γ-Fe_2O_3), or goethite ($FeO(OH)$) are not observed.
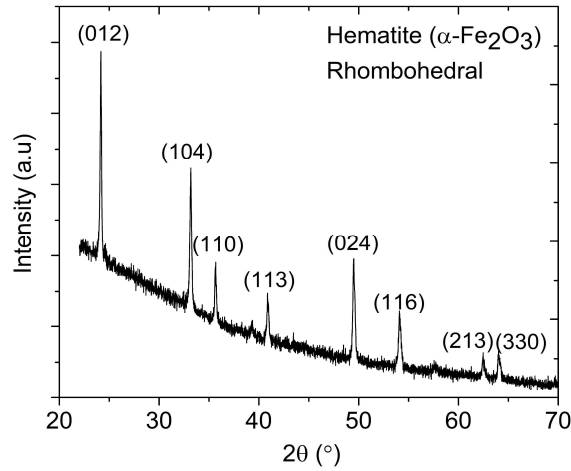
Figure 6.3. XRD pattern of a spray-deposited α-Fe_2O_3 film.

6.4 Characterizations of Sulfurized α-Fe_2O_3 thin films

As-prepared α-Fe_2O_3 films were sulfurized in a tube furnace at various temperatures ranging from 300°C to 450°C under 10 torr of H_2S for 30 min. The thickness of all the α-Fe_2O_3 films was 1 µm. As shown in Fig. 6.4(a), the transmittance of the sulfurized hematite films decreases with annealing temperature between 300°C and 450°C. More importantly, while the transmittance decreases, the absorption edge doesn't shift suggesting little change in the bandgap. At 450°C, the hematite film becomes totally opaque in the entire wavelength range measured (300–2400 nm). XRD spectrum of the sample sulfurized at 450°C for 30 min is shown in Fig. 6.5(a). It reveals that the α-Fe_2O_3 film undergoes phase transformation from hematite into a mixture of magnetite (Fe_3O_4) and pyrrhotite (FeS) phases. The decrease in transmittance is likely caused by the Fe_3O_4 phase which is semi-metallic and opaque in nature. It is suggested that the surface of the α-Fe_2O_3 grains in Fig.

71

6.1(a) after sulfurization transforms into FeS while the core of the α-Fe$_2$O$_3$ grains changes into Fe$_3$O$_4$. This hypothesis is supported by annealing the sample in H$_2$S at 450°C for 3 h. The hematite film is completely transformed into FeS$_2$ as shown in Fig. 6.5(b). The transmittance spectrum indicates that FeS$_2$ film has a low transmittance in the range of 30–40%. The bandgap of FeS$_2$ is estimated to be 1.3 eV for direct transition and 0.93 eV for indirect transition as shown in Figs. 6.4(c) and 4(d). Fig. 6.5(c) shows the morphology of FeS$_2$. The grains of FeS$_2$ are about 1 μm in size, and they have irregular shapes.
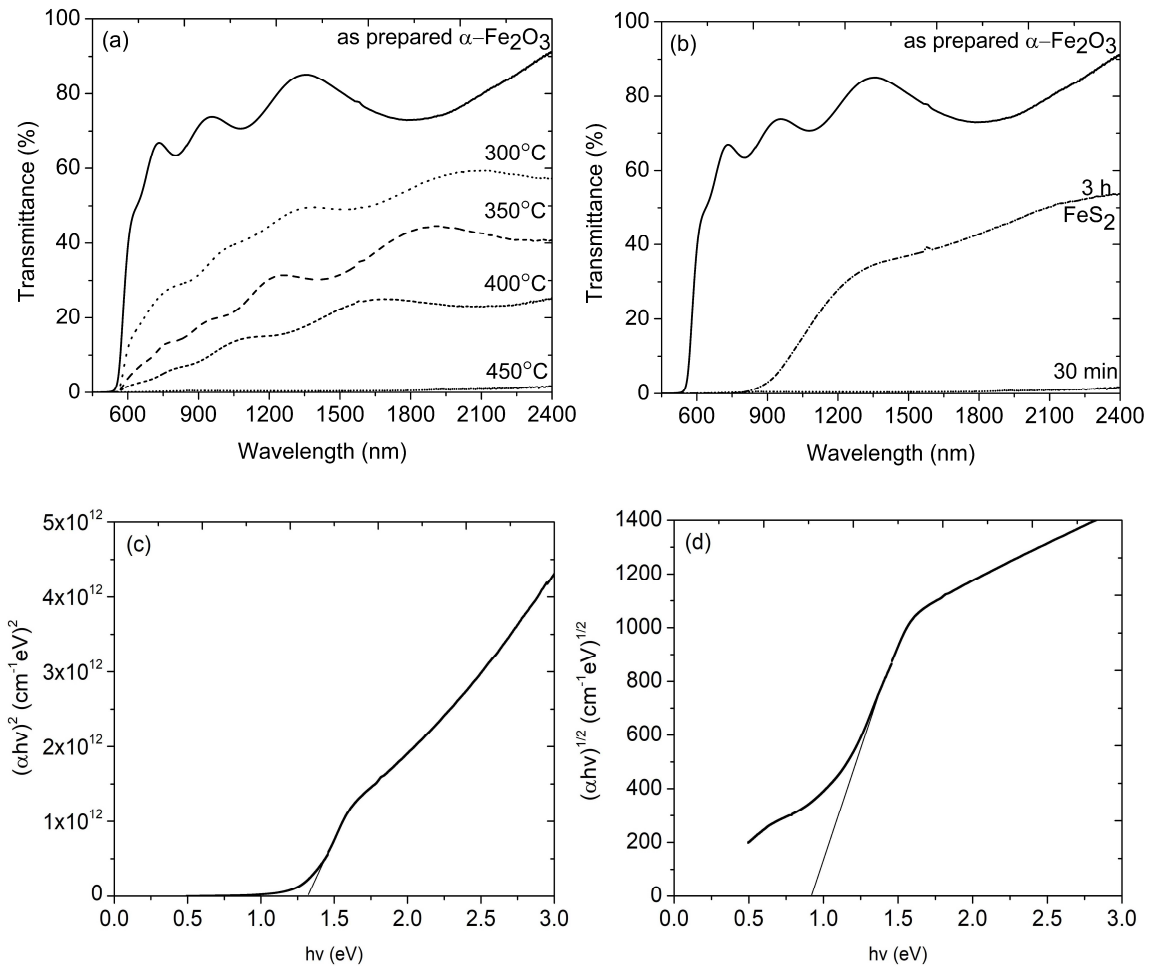
Figure 6.4. Transmittance spectra of α-Fe$_2$O$_3$ after sulfurization at (a) different

temperatures and (b) at 450˚C for different times. (c) Direct and (d) indirect bandgap

calculations for FeS$_2$ from (b) using Tauc's plots.
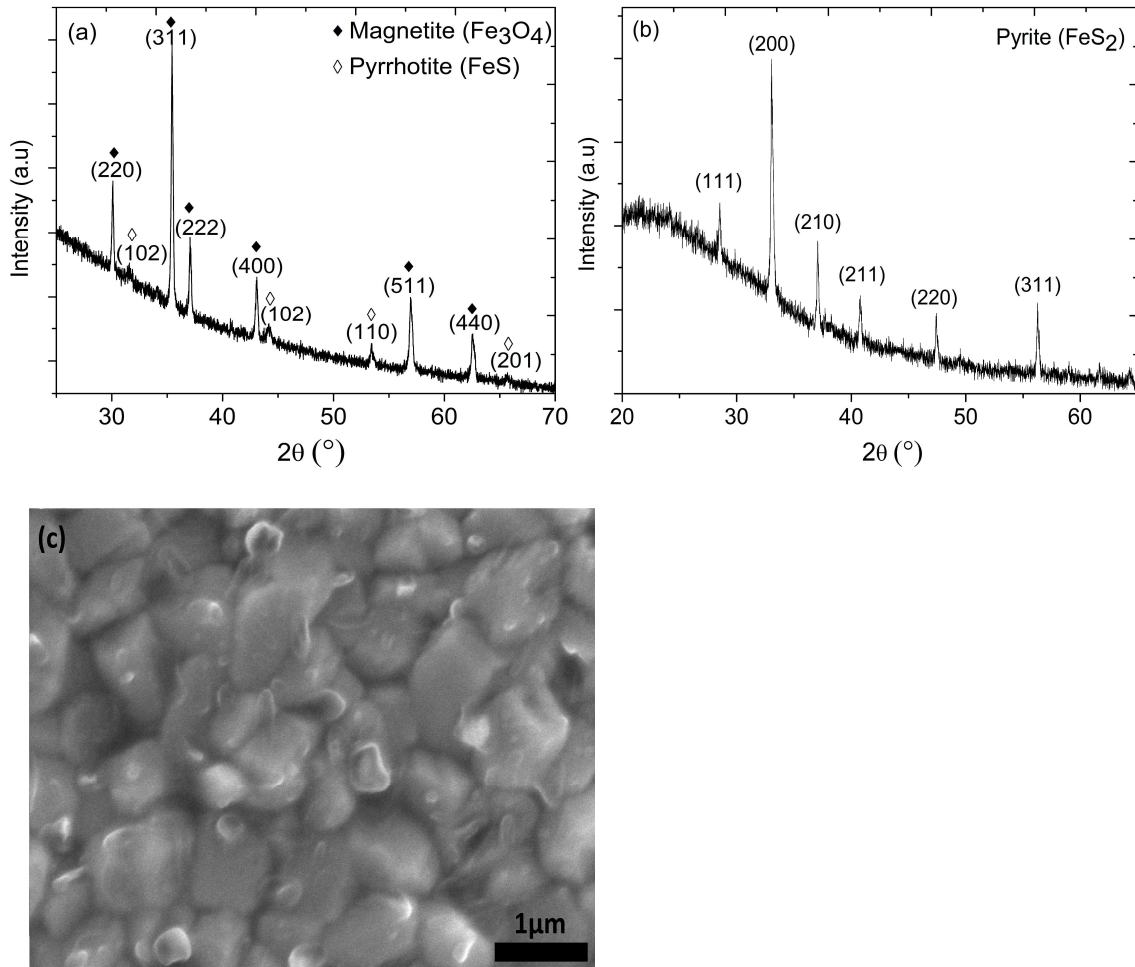
Figure 6.5. XRD patterns of α-Fe$_2$O$_3$ after sulfurization at 450˚C (a) for 30 min and (b)

for 3 h. (c) Surface morphology of FeS$_2$ from Fig. 6.4(b).
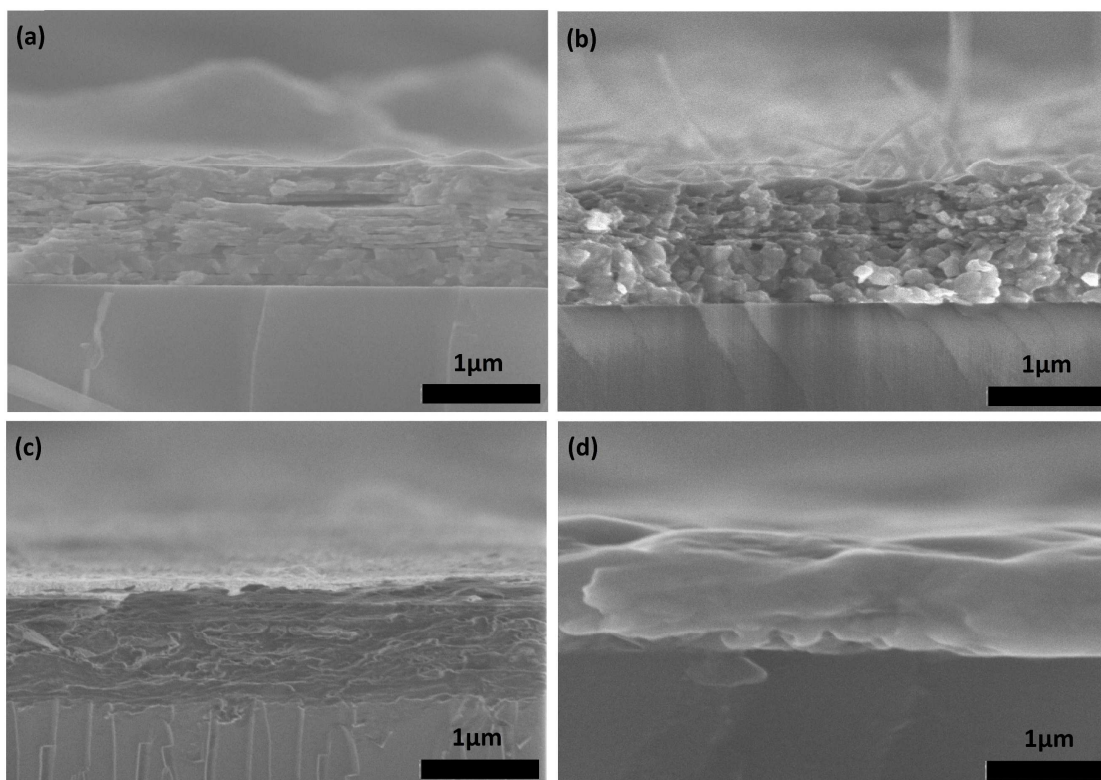
Figure 6.6. SEM cross section images of α-Fe$_2$O$_3$ after sulfurization at (a) as-prepared, (b) 350˚C for 1 h, (c) 450˚C for 1 h, and (d) 450˚C for 3 h.

Figure 6.6 shows SEM cross section image of as-prepared and sulfurized α-Fe$_2$O$_3$ films at various temperatures and times. Up to 350˚C, there is little change in morphology (Fig. 6.6(b)). At 450˚C, distinctive morphological changes are observed (Fig. 6.6(c)). The morphological changes are related to formation of Fe$_3$O$_4$ and FeS phases as revealed by XRD (Fig. 6.5(a)). When annealed at 450˚C for 3 h, α-Fe$_2$O$_3$ is completely transformed into FeS$_2$, and further morphological changes are observed (Fig. 6.6(d)). For all the sulfurization conditions studied, the films have good adherence to the substrate.

Table 6.2 lists the resistivity of α-Fe$_2$O$_3$ films after sulfurization under different conditions. Sheet resistance of as-prepared α-Fe$_2$O$_3$ was not measurable using a four-point

probe indicating that α-Fe_2O_3 is extremely resistive. As sulfurization temperature increases from 300˚C to 450˚C, the resistivity of the film decreases from 7.1 Ω-cm to 0.0045 Ω-cm. The latter is likely due to the formation of semi-metallic Fe_3O_4. FeS_2 films show p-type conductivity with a resistivity of 3.2 Ω-cm.

Table 6.2

Resistivity of α-Fe_2O_3 films after sulfurization under different conditions

Sulfurization conditions	300˚C 30 m	350˚C 30 m	400˚C 30m	450˚C 30 m	450˚C 1 h
Resistivity (Ω-cm)	7.1	0.12	0.037	0.0045	3.2

Since α-Fe_2O_3 underwent phase transformation when annealed in a S-rich O-deficient environment, re-oxidation of FeS_2 by annealing it in a S-deficient O-rich environment was performed to investigate its effect on FeS_2. Fig. 6.7 depicts the transmittance spectra of FeS_2 films after annealing in air at various temperatures and times. The transmittance of FeS_2 increases gradually with temperature and the absorption edge of FeS_2 near 900 nm becomes sharper as the annealing temperature increases from 300˚C to 400˚C, as shown in Fig. 6.7(a). However, the absorption edge doesn't move indicating that the bandgap doesn't change. The annealing time was fixed to 1 h for this set of experiments. In the next set of experiments, the annealing temperature was fixed to 400˚C while the annealing time was varied from 1 h to 4 h. As shown in Fig. 6.7(b), the absorption edge of FeS_2 changes slightly to a shorter wavelength when the annealing time increases from 1 h to 2 h. For annealing times longer than 3 h, there is a sudden change in absorption edge from 900 nm for FeS_2

75

to 520 nm for α-Fe$_2$O$_3$ indicating the sudden appearance of α-Fe$_2$O$_3$ within the film between 2 h and 3 h. Therefore, there is no Fe oxysulfide formed during re-oxidation, neither FeO$_x$S$_{2-x}$ nor α-Fe$_2$O$_{3-x}$S$_x$. After 4 h of annealing, FeS$_2$ is fully oxidized back to α-Fe$_2$O$_3$.
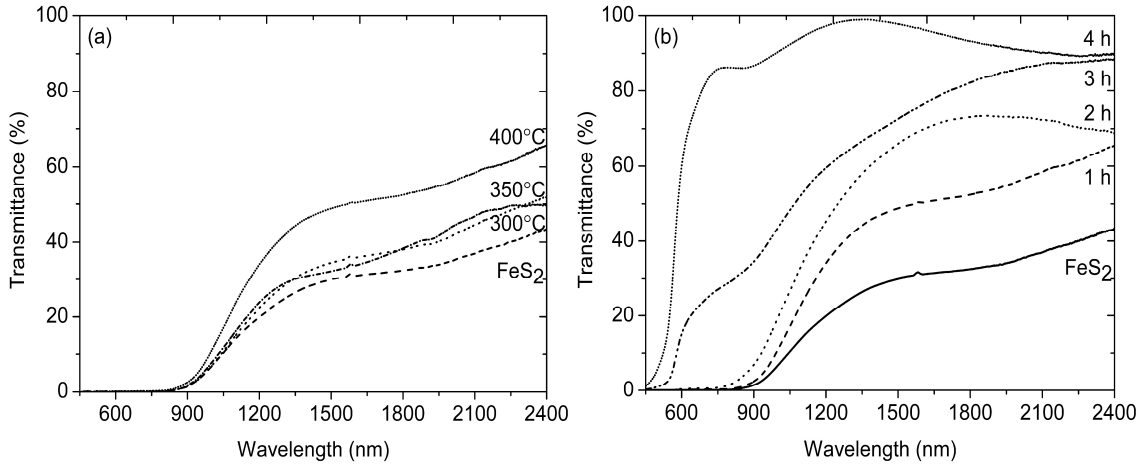
Figure 6.7. Transmittance spectra of FeS$_2$ after annealing in air (a) at different temperatures and (b) at 400˚C for different times.

6.5 Characterizations of Anatase TiO$_2$ Thin Films

Figure 6.8 shows the total transmittance spectrum of a sol-gel synthesized anatase TiO$_2$ film on a quartz substrate. As-prepared TiO$_2$ is over 90% transparent over a broad wavelength range and shows a sharp absorption edge near 370 nm. The thickness of the TiO$_2$ film is about 1μm. The optical bandgap of TiO$_2$ is evaluated from the transmittance spectrum using the Tauc's relation as shown in Fig. 6.9. The estimated bandgap of as-prepared TiO$_2$ is 3.55 eV for direct transition and 3.2 eV for indirect transition. The transmittance spectrum also suggests that the bandgap of sol-gel synthesized TiO$_2$ is direct.
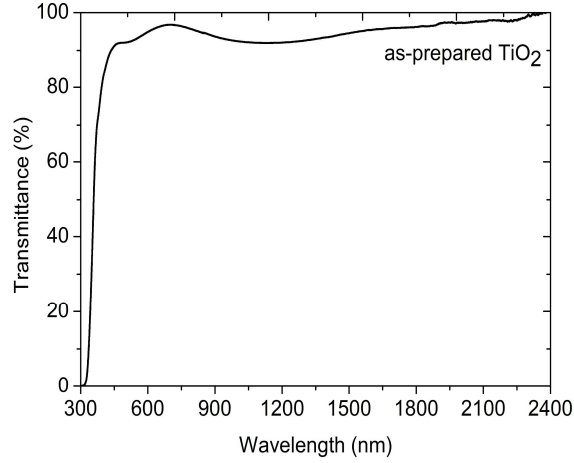
Figure 6.8. Transmittance spectrum by spectrophotometry of sol-gel synthesized TiO_2.
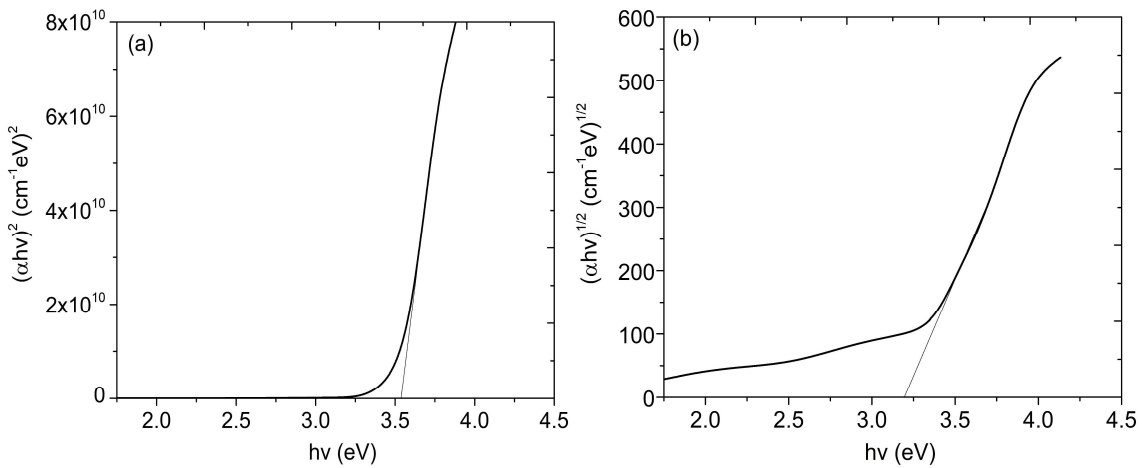
Figure 6.9. (a) Direct and (b) indirect bandgap calculations of a sol-gel synthesized TiO_2 film using Tauc's plots.

6.6 Characterizations of Sulfurized TiO_2 Thin Films

As-prepared TiO_2 films were annealed at temperatures between 550°C and 700°C under 10 torr of H_2S for 1 h. Fig. 6.10 compares the transmittance and reflectance spectra of anatase TiO_2 after annealing in H_2S. Anatase TiO_2 is more stable than α-Fe_2O_3 during

sulfurization at higher temperatures. While α-Fe$_2$O$_3$ films undergo phase transformation to Fe$_3$O$_4$ and FeS at a relatively-low temperature of 250°C, TiO$_2$ is stable up to 500°C as shown in Fig. 6.10(a). However, starting at 550°C, a new absorption edge at higher wavelengths between 650 nm and 1200 nm appears indicating a changing bandgap to the lower energy range. As the sulfurization temperature increases, the transmittance of TiO$_2$ gradually decreases while the absorption edge continues to shift towards lower energy. The relatively-small changes in reflectance for the same samples as shown in Fig. 6.10(b) suggest that the decrease in transmittance is due to absorption.
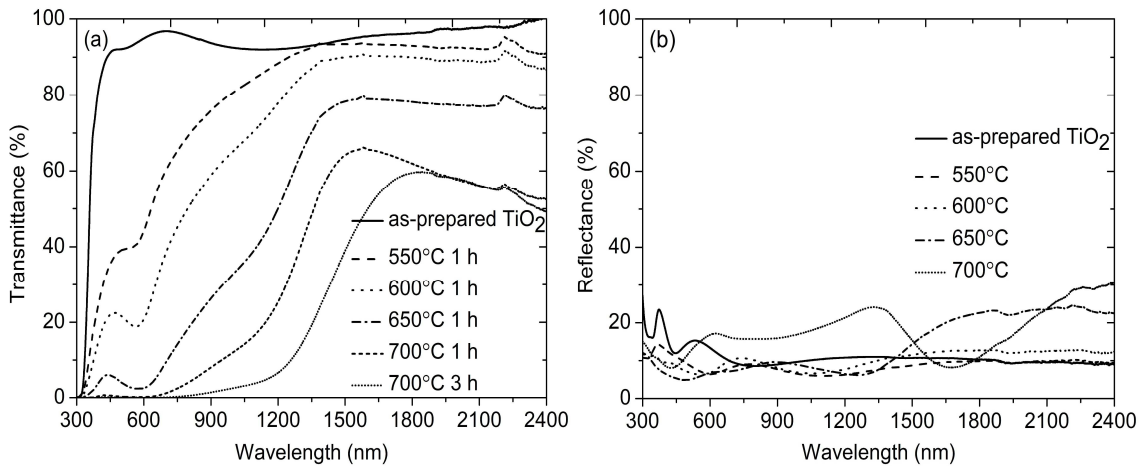
Figure 6.10. (a) Transmittance and (b) reflectance spectra of anatase TiO$_2$ after sulfurization at different temperatures and times.
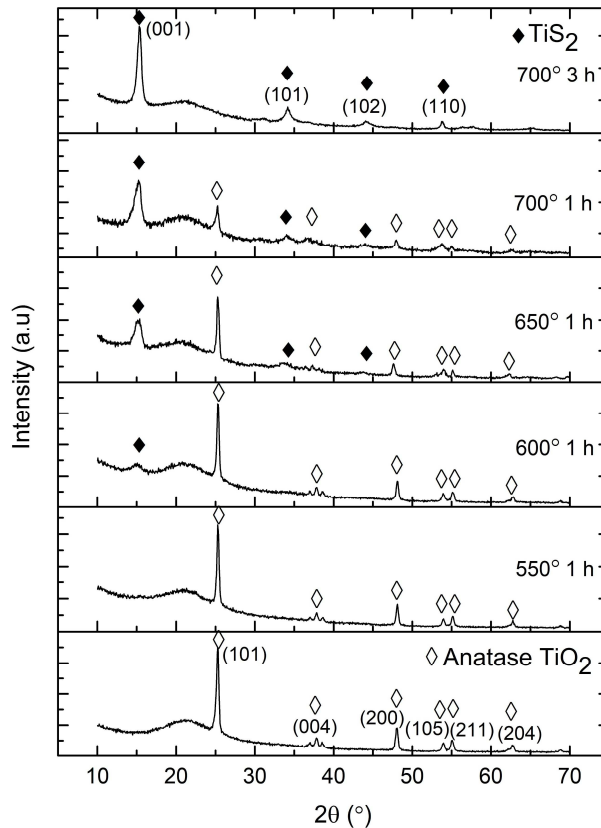
Figure 6.11. XRD patterns of anatase TiO$_2$ films after sulfurization at different temperatures and times.

The XRD patterns of as-prepared and H$_2$S-annealed TiO$_2$ films reveal the exclusive presence of anatase TiO$_2$ up to 550˚C (Fig. 6.11). No diffraction peaks from other TiO$_2$ phases such as rutile and brookite or Ti sulfide phases such as TiS$_2$ are detectable at 550˚C. Anatase TiO$_2$ starts to transform into TiS$_2$ at 600˚C when TiS$_2$ diffraction peaks starts to appear in XRD. As the annealing temperature increases, the intensity of TiO$_2$ diffraction peaks decreases gradually, indicating a loss of anatase TiO$_2$. In contrast, the intensity of TiS$_2$ peaks increases as the annealing temperature increases. When anatase TiO$_2$ is annealed at 700˚C for 3 h, it completely transforms into TiS$_2$ and there is no TiO$_2$

diffraction peak observed. Between 600˚C and 700˚C, there co-exist two phases, TiO$_2$ and TiS$_2$.

In order to investigate possible incorporation of S atoms into the anatase TiO$_2$ lattice, the lattice parameters as well as crystallite sizes of the sulfurized samples were evaluated. If O atoms in the TiO$_2$ lattice are replaced by S atoms which have a larger radius, the lattice parameters should show slight increase along all three directions (*a*, *b*, and *c* axes). Lattice parameters were calculated using the relationship between Bragg's law and crystal geometry for the tetragonal structure as shown below:

$$d_{(hkl)} = \lambda/2\sin\theta \quad (6.2)$$

$$1/d^2 = (h^2+k^2)/a^2 + l^2/c^2 \quad (6.3)$$

The calculated lattice parameters of as-prepared TiO$_2$ are a = b = 3.78784 Å and c = 9.57356 Å. Lattice parameters of TiO$_2$ films after sulfurization at different temperatures are shown in Table 6.3. Sulfurization doesn't show noticeable increase in lattice parameters indicating no presence of a single-phase Ti oxysulfide (TiO$_{2-x}$S$_x$) after sulfurization.

Table 6.3

Lattice parameters of anatase TiO$_2$ films after sulfurization at different temperatures

Annealing temperature	Lattice parameters
550˚C	a = b = 3.78801 Å, c = 9.57403 Å
600˚C	a = b = 3.78848 Å, c = 9.57457 Å
650˚C	a = b = 3.78771 Å, c = 9.57328 Å

In addition to lattice parameters, the crystallite size before and after sulfurization was estimated by applying the Debye-Scherrer equation to the full width at half maximum (FWHM) of the (101) peak of anatase TiO$_2$:

80

$$D = K\lambda/(\beta \cos \theta) \quad (6.4)$$

where D is the average crystallite size in angstrom, K is a constant which is taken as 0.89, λ is the wavelength of the X-ray radiation (Cu Kα, 0.15406 nm), β is the corrected FWHM after subtraction of equipment broadening, and θ is the diffraction angle. As shown in Table 6.4, samples annealed below 600°C in H_2S show slight peak broadening as compared to the as-prepared sample. The average crystallite size increases from 32 nm to 39 nm as the sulfurization temperature increases from room temperature to 600°C. It is expected that as the annealing temperature increases, the crystallites grow in size. At 650°C, the crystallite size decreases to 30.5 nm. Fig. 6.11 suggests that the second phase, TiS_2, forms between 600°C and 650°C. It is speculated that the formation of the second phase is at the expense of the anatase TiO_2 phase.

Table 6.4

Crystallite size of anatase TiO_2 films after sulfurization at different temperatures

Annealing temperature	FWHM (°)	Crystallite size (nm)
As-prepared	0.350	32.3
550°C	0.327	34.4
600°C	0.294	39.8
650°C	0.360	30.5

Raman spectroscopy was employed to obtain more information about the microstructure of as-prepared and sulfurized TiO_2 films. Fig. 6.12(a) shows the Raman spectra of as-prepared and sulfurized TiO_2. The observed peaks at 151, 404, 513, and 634 cm^{-1} are

attributed to the anatase phase and anatase is the only phase present in as-prepared TiO_2. There are no detectable peaks from other Ti phases such as rutile or brookite in as-prepared TiO_2. After 600°C annealing in H_2S, peaks at 227 and 335 cm^{-1} start to appear which are attributed to the TiS_2 phase. As the annealing temperature increases to 650°C, the peaks related to TiS_2 become stronger while the peaks related to anatase TiO_2 become weaker. The 151 cm^{-1} peak of anatase TiO_2 for samples annealed at different temperatures is compared in Fig. 6.12(b). The position of the 151 cm^{-1} peak shifts slightly to a higher wavenumber as the annealing temperature increases. In general, lighter atoms vibrate at higher frequencies. Therefore, if a single-phase $TiO_{2-x}S_x$ exists within the film, the peak should shift to a lower wavenumber since S atoms are heavier than O atoms. Peak shifting to a higher wavenumber by sulfurization is probably caused by structural stress introduced by the presence of the second phase, TiS_2.
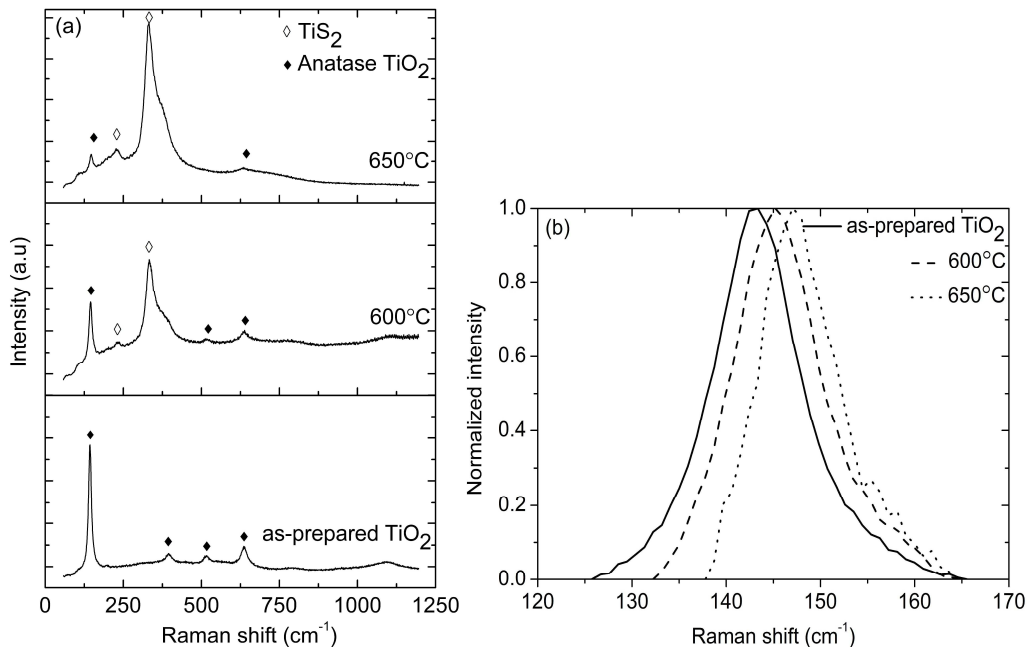
Figure 6.12. (a) Raman spectra of anatase TiO_2 after sulfurization at different temperatures for 1 h and (b) comparison of the 151 cm^{-1} peak at different temperatures.

82

EDX was employed to determine the S content within the sulfurized TiO_2 film. As shown in Fig. 6.13, EDX spectra show peaks at 0.525 keV, 2.306 keV, and 4.507 keV which correspond to $K\alpha$ peaks of O, S, and Ti atoms, respectively. Table 6.5 indicates that the atomic percentage of S content gradually increases as the temperature increases. It is noted that the atomic percentage of S from EDX doesn't necessarily mean that S is distributed uniformly throughout the film in lateral and vertical directions since the penetration depth and spot size of EDX are typically about 1 μm. With the co-existence of TiO_2 and TiS_2, it is expected that the S content gradually decreases in the film from top to bottom and concentrates at grain boundaries without deep penetration into TiO_2 grains.
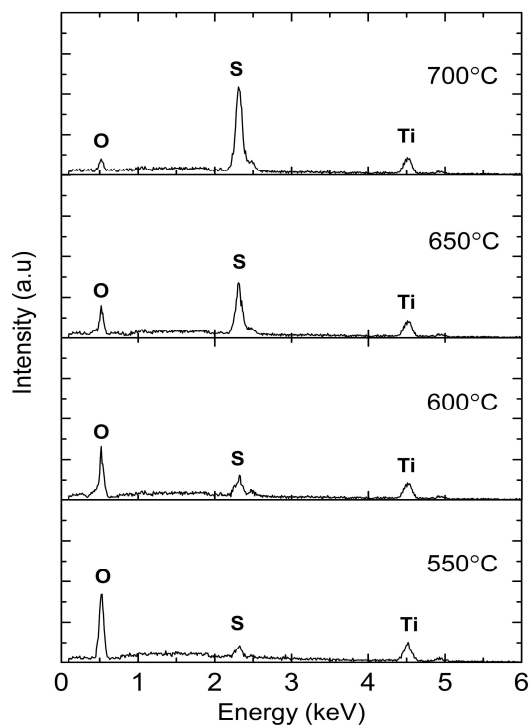
Figure 6.13. EDX spectra of anatase TiO_2 after sulfurization at different temperatures for 1 h.

Table 6.5

Quantitative analysis of anatase TiO_2 after sulfurization at different temperatures for 1h

Sulfurization temperature	Oxygen at%	Sulfur at%
550˚C	94	6
600˚C	68	32
650˚C	33	67
700˚C	12	88

Figure 6.14 shows SEM micrographs of as-prepared and sulfurized TiO_2 films at various temperatures. The grain size of the as-prepared anatase film is approximately 100 nm (Fig. 6.14(a)). Up to 550˚C, there is no distinctive change in the morphology of the film (Fig. 6.14(b)). Starting at 600˚C, morphological changes start to appear in the film (Fig. 6.14(c)) and become more prominent as the temperature increases (Fig. 6.14(d)). The changes in morphology are related to formation of TiS_2 since TiS_2 diffraction peaks start to appear at 600˚C according to XRD (Fig. 6.11) and Raman (Fig. 6.12). At 650˚C, large grains on top of the film and smaller TiO_2 grains below are observed, confirming that the film is composed of multiple phases as revealed by XRD and Raman. For all the sulfurization conditions, the films have good adherence to the substrate. However, TiS_2 is moisture sensitive as it reacts with moisture in the air and reoxide back to TiO_2. Based on our experimental results, sulfurized TiS_2 completely transforms back to TiO_2 after 3 months in the air.
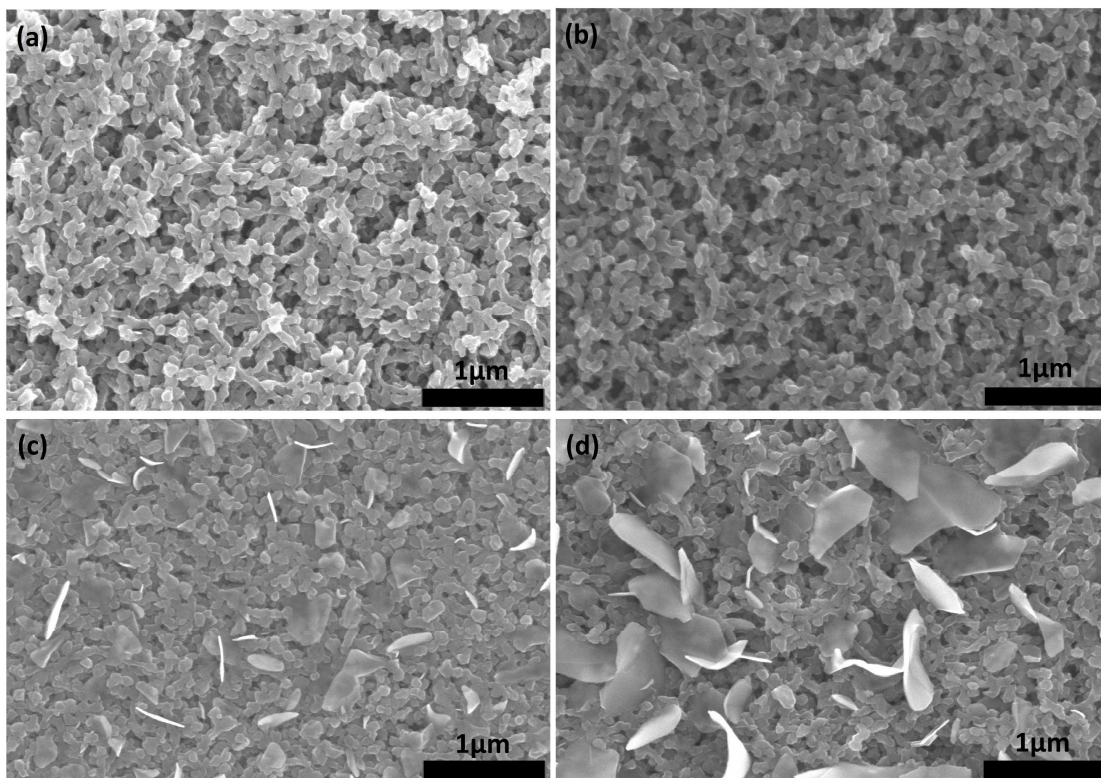
Figures 6.14. SEM top view images of anatase TiO$_2$ after sulfurization at (a) as-prepared, (b) 550˚C, (C) 600˚C, and (d) 650˚C.

6.7 Summary

Spray-deposited hematite Fe$_2$O$_3$ and sol-gel spin-coated anatase TiO$_2$ films were annealed in H$_2$S at various temperatures to investigate the effect of sulfurization by H$_2$S. The transmittance of α-Fe$_2$O$_3$ films decreases with annealing temperature between 300˚C and 450˚C. While the transmittance decreases, the absorption edge doesn't shift, suggesting no noticeable change in the bandgap. At 450˚C, the sulfurized α-Fe$_2$O$_3$ film becomes totally opaque. The resistivity of sulfurized α-Fe$_2$O$_3$ films also decreases with temperature. XRD reveals that α-Fe$_2$O$_3$ undergoes phase transformation into a mixture of Fe$_3$O$_4$ and FeS phases after annealing in H$_2$S. A 1-μm α-Fe$_2$O$_3$ film is fully transformed into FeS$_2$ after

annealing at 450°C for 3 h. FeS_2 shows p-type conductivity with a resistivity of 3.2 Ω-cm. It converts back to α-Fe_2O_3 by annealing it in the air at 400°C for 4 h.

On the other hand, anatase TiO_2 is more stable than α-Fe_2O_3 against sulfurization. Transformation of TiO_2 into TiS_2 starts above 550°C, and a 1-μm TiO_2 film is completely transformed into TiS_2 at 700°C after 3 h. TiO_2 films after sulfurization show small changes in their absorption edge, i.e. a new absorption edge in the wavelength range of 650 nm and 1200 nm appears. The shift in absorption edge indicates a changing bandgap to lower energy. However, XRD and Raman suggest that sulfurized TiO_2 is composed of multiple phases of TiO_2 and TiS_2 without the presence of a single-phase $TiO_{2-x}S_x$, i.e. S doesn't diffuse into the anatase TiO_2 lattice by annealing in H_2S. TiS_2 converts back to anatase TiO_2 after 3 months in the air, without annealing.

CHAPTER 7

CONCLUSION

In this thesis, various metal oxides are prepared by low-cost spray pyrolysis method for different applications in solar cells. In Chapter 6, spray-deposited hematite Fe_2O_3 and sol-gel prepared anatase TiO_2 thin films are sulfurized by annealing in H_2S to investigate the band gap narrowing by sulfur doping for their application as solar absorbers. While α-Fe_2O_3 films indicate no noticeable change in the bandgap, anatase TiO_2 films show small changes in their absorption edge after annealing in H_2S. However, structural characterizations of sulfurized TiO_2 films reveal that sulfurized TiO_2 is composed of multiple phases of TiO_2 and TiS_2 without the presence of a single-phase $TiO_{2-x}S_x$. i.e. S does not diffuse into the α-Fe_2O_3 and anatase TiO_2 lattice by annealing in H_2S.

In Chapter 5, low-cost spray-deposited ZrO_2 is investigated for its application as front side dielectric in Si solar cells. Optical, electrical, and structural properties of spray-deposited ZrO_2 are studied and compared to the industrial standard PECVD SiNx to evaluate the suitability of ZrO_2 as the antireflection and passivation layer in Si solar cells. Optical studies show that the reflection and absorption losses in spray-deposited ZrO_2 are comparable to SiN_x indicating that ZrO_2 is a good candidate for antireflection coating in c-Si solar cells. However, electrical studies show that ZrO_2 does not effectively passivate the n-type Si surface due to the negative density of fixed charges present in ZrO_2 film. This suggests that ZrO_2 may be able to serve for surface passivation on p-type Si. Doping in ZrO_2 is attempted to manipulate the density of fixed charges, but a negative flat-band voltage shift (increase in positive charge density) is not observed.

In Chapter 4, the possibility of using low-cost spray-deposited Al_2O_3 for rear passivation and optical trapping in Si PERC cells is investigated. Optical, electrical, and structural properties of spray-deposited Al_2O_3 are examined and compared to the industrial standard ALD Al_2O_3/PECVD SiN_x stack. Electrical characteristics of spray-deposited Al_2O_3 show that spray-deposited Al_2O_3 can serve as the passivation layer on p-type Si. Optical properties of spray-deposited Al_2O_3 are identical to the ALD Al_2O_3/PECVD SiN_x stack, indicating that spray-deposited Al_2O_3 can also serve as the optical trapping layer. These properties suggest that low-cost spray-deposited Al_2O_3 is a promising candidate to replace the ALD Al_2O_3/PECVD SiN_x stack in Si PERC cells.

In the future, spray-deposited Al_2O_3 should be tested in actual devices to check if the different passivation quality and optical performance will have a significant effect on actual solar cells. Furthermore, the new design of experimental set-up such as using multiple spray heads or rotating the substrate during the deposition should also be carried out to improve the film thickness uniformity on textured Si surface.

REFERENCES

[1]   Hoffert MI, Caldeira K, Jain AK, Haites EF, Harvey LD, Potter SD, Schlesinger ME, Schneider SH, Watts RG, Wigley TM, Wuebbles DJ. Energy implications of future stabilization of atmospheric CO_2 content. Nature. 1998 Oct;395(6705):881.

[2]   Endeavor Business Media, 2019.

[3]   SPV Market Research, 2018.

[4]   International Technology Roadmap for Photovoltaic (ITRPV), 2017.

[5]   Institute for Solar Energy Research in Hamelin, 2018.

[6]   Lauinger T, Schmidt J, Aberle AG, Hezel R. Record low surface recombination velocities on 1 Ω cm p□silicon using remote plasma silicon nitride passivation. Applied Physics Letters. 1996 Feb 26;68(9):1232-4.

[7]   Dauwe S, Mittelstädt L, Metz A, Hezel R. Experimental evidence of parasitic shunting in silicon nitride rear surface passivated solar cells. Progress in Photovoltaics: Research and Applications. 2002 Jun;10(4):271-8.

[8]   Hoex B, Heil SB, Langereis E, Van de Sanden MC, Kessels WM. Ultralow surface recombination of c-Si substrates passivated by plasma-assisted atomic layer deposited Al_2O_3. Applied Physics Letters. 2006 Jul 24;89(4):042112.

[9]   Schmidt J, Merkle A, Brendel R, Hoex B, de Sanden MV, Kessels WM. Surface passivation of high□efficiency silicon solar cells by atomic□layer□deposited Al_2O_3. Progress in photovoltaics: research and applications. 2008 Sep;16(6):461-6.

[10]   Institute for Microelectronics, 2018.

[11]   Clean Energy Reviews, 2018.

[12]   Design Rules of Crystalline Silicon, Delft University of Technology, 2013.

[13]   Edmund Optics Inc, 2019.

[14]   Rahman MM, Udoy AB. Investigation of surface passivation schemes for p-type monocrystalline silicon solar cell. Applied Physics A. 2016 Oct 1;122(10):926.

[15]   PerkinElmer Inc, 2009.

[16]   J.A. Woollam, 2019.

[17]   Canadian Centre for Electron Microscopy, February 2017

[18]   Wang Y, Özcan AS, Özaydin G, Ludwig Jr KF, Bhattacharyya A, Moustakas TD, Zhou H, Headrick RL, Siddons DP. Real-time synchrotron x-ray studies of low-and high-temperature nitridation of c-plane sapphire. Physical Review B. 2006 Dec 4;74(23):235304.

[19]   AG jacobs, Experimental Physics Saarland University, 2019.

[20]   Metz A, Adler D, Bagus S, Blanke H, Bothar M, Brouwer E, Dauwe S, Dressler K, Droessler R, Droste T, Fiedler M. Industrial high-performance crystalline silicon solar cells and modules based on rear surface passivation technology. Solar Energy Materials and Solar Cells. 2014 Jan 1;(120):417-25.

[21]   Batra N, Gope J, Singh R, Panigrahi J, Tyagi S, Pathi P, Srivastava SK, Rauthan CM, Singh PK. Effect of low thermal budget annealing on surface passivation of silicon by ALD based aluminum oxide films. Physical Chemistry Chemical Physics. 2014;16(39):21804-11.

[22]   Vermang B, Goverde H, Tous L, Lorenz A, Choulat P, Horzel J, John J, Poortmans J, Mertens R. Approach for Al_2O_3 rear surface passivation of industrial p□type Si PERC above 19%. Progress in Photovoltaics: Research and Applications. 2012 May;20(3):269-73.

[23]   Groner MD, Fabreguette FH, Elam JW, George SM. Low-temperature Al_2O_3 atomic layer deposition. Chemistry of materials. 2004 Feb 24;16(4):639-45.

[24]   Dingemans G, Van de Sanden MC, Kessels WM. Influence of the deposition temperature on the c-Si surface passivation by Al_2O_3 films synthesized by ALD and PECVD. Electrochemical and Solid-state letters. 2010 Mar 1;13(3):H76-9.

[25]   Rice CE, Cuchiaro JD, Sun S, Provost LG, Tompa GS, Davenport T, Fox G, Sun S, Chu F. Development of low temperature Al_2O_3 MOCVD for ferroelectric film passivation on 8 ″wafers. Integrated Ferroelectrics. 2003 Sep 1;59(1):1453-63.

[26]   Black LE, Allen T, Cuevas A, McIntosh KR, Veith B, Schmidt J. Thermal stability of silicon surface passivation by APCVD Al_2O_3. Solar Energy Materials and Solar Cells. 2014 Jan 1;120:339-45.

[27]   Quah HJ, Cheong KY. Surface passivation of gallium nitride by ultrathin RF-magnetron sputtered Al_2O_3 gate. ACS applied materials & interfaces. 2013 Jul 24;5(15):6860-3.

[28]   Schmidt J, Kerr M. Highest-quality surface passivation of low-resistivity p-type silicon using stoichiometric PECVD silicon nitride. Solar Energy Materials and

Solar Cells. 2001 Jan 1;65(1-4):585-91.

[29] Hai-Qing X, Chun-Lan Z, Xiao-Ning C, Wen-Jing W, Lei Z, Hai-Ling L, Hong-Wei D. Excellent passivation of p-type Si surface by sol-gel Al_2O_3 films. Chinese Physics Letters. 2009 Aug;26(8):088102.

[30] Kalaivani S, Kottantharayil A. Spray coated aluminum oxide thin film for P-type crystalline silicon surface passivation. In 2015 IEEE 42nd Photovoltaic Specialist Conference (PVSC) 2015 Jun 14 (pp. 1-4). IEEE.

[31] Shin WJ, Huang WH, Tao M. Low-Cost Spray-Deposited ZrO_2 for Antireflection in Si Solar Cells. Materials Chemistry and Physics. 2019 Mar 21.

[32] Sproul AB. Dimensionless solution of the equation describing the effect of surface recombination on carrier decay in semiconductors. Journal of Applied Physics. 1994 Sep 1;76(5):2851-4.

[33] Stephens AW, Green MA. Minority carrier mobility of Czochralski☐grown silicon by microwave☐detected photoconductance decay. Journal of applied physics. 1993 Nov 15;74(10):6212-6.

[34] Agostinelli G, Delabie A, Vitanov P, Alexieva Z, Dekkers HF, De Wolf S, Beaucarne G. Very low surface recombination velocities on p-type silicon wafers passivated with a dielectric with fixed negative charge. Solar Energy Materials and Solar Cells. 2006 Nov 23;90(18-19):3438-43.

[35] Engel-Herbert R, Hwang Y, Stemmer S. Comparison of methods to quantify interface trap densities at dielectric/III-V semiconductor interfaces. Journal of applied physics. 2010 Dec 15;108(12):124101.

[36] Fraunhofer Institute for Solar Energy Systems, Photovoltaic Report, 2018.

[37] Diop MM, Diaw A, Mbengue N, Ba O, Diagne M, Niasse OA, Ba B, Sarr J. Optimization and modeling of antireflective layers for silicon solar cells: in search of optimal materials. Materials Sciences and Applications. 2018 Jul 6;9(08):705-22.

[38] Gangopadhyay U, Kim K, Mangalaraj D, Yi J. Low cost CBD ZnS antireflection coating on large area commercial mono-crystalline silicon solar cells. Applied Surface Science. 2004 May 31;230(1-4):364-70.

[39] Gangopadhyay U, Ray S, Panda E, Jana S, Das S. Efficiency enhancement of solar cell by introduction of cerium oxide along with silicon nitride. International Journal of Renewable and Sustainable Energy. 2013;2(2):46-50.

[40] Hocine D, Belkaid MS, Pasquinelli M, Escoubas L, Simon JJ, Rivière GA, Moussi

A. Improved efficiency of multicrystalline silicon solar cells by TiO_2 antireflection coatings derived by APCVD process. Materials Science in Semiconductor Processing. 2013 Feb 1;16(1):113-7.

[41] Rubio F, Denis J, Albella JM, Martinez-Duart JM. Sputtered Ta_2O_5 antireflection coatings for silicon solar cells. Thin Solid Films. 1982 Apr 30;90(4):405-8.

[42] Aurang P, Demircioglu O, Es F, Turan R, Unalan HE. ZnO nanorods as antireflective coatings for industrial☐scale single☐crystalline silicon solar cells. Journal of the American Ceramic Society. 2013 Feb 28;96(4):1253-7.

[43] Verlaan V, Verkerk AD, Arnoldbik WM, van der Werf CH, Bakker R, Houweling ZS, Romijn IG, Borsa DM, Weeber AW, Luxembourg SL, Zeman M. The effect of composition on the bond structure and refractive index of silicon nitride deposited by HWCVD and PECVD. Thin Solid Films. 2009 Apr 30;517(12):3499-502.

[44] Wan Y, McIntosh KR, Thomson AF. Characterization and optimization of PECVD SiN_x as an antireflection coating and passivation layer for silicon solar cells. AIP Advances. 2013 Mar 5;3(3):032113-1-15.

[45] Ko J, Gong D, Pillai K, Lee KS, Ju M, Choi P, Kim KR, Yi J, Choi B. Double layer SiN_x:H films for passivation and anti-reflection coating of c-Si solar cells. Thin Solid Films. 2011 Aug 1;519(20):6887-91.

[46] Krogman KC, Druffel T, Sunkara MK. Antireflective optical coatings incorporating nanoparticles. Nanotechnology. 2005 Apr 15;16(7):S338-43.

[47] U.S. Geological Survey, Mineral Commodity Summary, 2018.

[48] Tao M, Terawatt Solar Photovoltaics – Roadblocks and Opportunities. London: Springer, 2014.

[49] Shin WJ, Wang L, Tao M. Low-cost spray deposited ZrO_2 for passivation and antireflection on p-type Si. In 43rd IEEE Photovoltaic Specialists Conference. 2016 Jun 5 (pp. 2971-4). IEEE.

[50] French RH, Glass SJ, Ohuchi FS, Xu YN, Ching WY. Experimental and theoretical determination of the electronic structure and optical properties of three phases of ZrO_2. Physical Review B. 1994 Feb 14;49(8):5133-42.

[51] Balakrishnan G, Thanigaiarul K, Sudhakara P, Song JI. Microstructural and optical properties of nanocrystalline undoped zirconia thin films prepared by pulsed laser deposition. Applied Physics A. 2013 Feb 1;110(2):427-32.

[52] Chang JP, Lin YS. Dielectric property and conduction mechanism of ultrathin

zirconium oxide films. Applied Physics Letters. 2001 Nov 26;79(22):3666-8.

[53]   Dingemans G, Seguin R, Engelhart P, van de Sanden MCM, Kessels WMM. Silicon surface passivation by ultrathin Al_2O_3 films synthesized by thermal and plasma atomic layer deposition. Physica Status Solidi–Rapid Research Letters. 2010 Feb 4;4(1-2);10-2.

[54]   Qi WJ, Nieh R, Lee BH, Kang L, Jeon Y, Lee JC. Electrical and reliability characteristics of ZrO_2 deposited directly on Si for gate dielectric application. Applied Physics Letters. 2000 Nov 13;77(20):3269-71.

[55]   Tarre A, Aarik J, Mändar H, Niilisk A, Pärna R, Rammula R, Uustare T, Rosental A, Sammelselg V. Atomic layer deposition of Cr_2O_3 thin films: Effect of crystallization on growth and properties. Applied Surface Science. 2008 Jun 15;254(16):5149-56.

[56]   Park JH, Kim S, Bard AJ. Novel carbon-doped TiO_2 nanotube arrays with high aspect ratios for efficient solar water splitting. Nano Letters. 2006 Jan 11;6(1):24-8.

[57]   Sivula K, Le Formal F, Grätzel M. Solar water splitting: progress using hematite ($\alpha\Box Fe_2O_3$) photoelectrodes. ChemSusChem. 2011 Apr 18;4(4):432-49.

[58]   Wang G, Wang H, Ling Y, Tang Y, Yang X, Fitzmorris RC, Wang C, Zhang JZ, Li Y. Hydrogen-treated TiO_2 nanowire arrays for photoelectrochemical water splitting. Nano Letters. 2011 Jun 28;11(7):3026-33.

[59]   Hu YS, Kleiman-Shwarsctein A, Forman AJ, Hazen D, Park JN, McFarland EW. Pt-doped α-Fe_2O_3 thin films active for photoelectrochemical water splitting. Chemistry of Materials. 2008 Jun 3;20(12):3803-5.

[60]   Bach U, Lupo D, Comte P, Moser JE. Solid-state dye-sensitized mesoporous TiO_2 solar cells with high proton-to-electron conversion efficiencies. Nature. 1998 Oct 8;395(6702):583-585.

[61]   Park NG, Van de Lagemaat J, Frank AJ. Comparison of dye-sensitized rutile- and anatase-based TiO_2 solar cells. Journal of Physical Chemistry B. 2000 Sep 28;104(38):8989-94.

[62]   Huang SY, Schlichthörl G, Nozik AJ, Grätzel M, Frank AJ. Charge recombination in dye-sensitized nanocrystalline TiO_2 solar cells. Journal of Physical Chemistry B. 1997 Apr 3;101(14):2576-82.

[63]   Hara K, Sayama K, Ohga Y, Shinpo A, Suga S, Arakawa H. A coumarin-derivative dye sensitized nanocrystalline TiO_2 solar cell having a high solar-energy conversion efficiency up to 5.6%. Chemical Communications. 2001 Mar 21;(6):569-70.

[64] Ling Y, Wang G, Wheeler DA, Zhang JZ, Li Y. Sn-doped hematite nanostructures for photoelectrochemical water splitting. Nano Letters. 2011 Apr 8;11(5):2119-25.

[65] Ennaoui A, Fiechter S, Jaegermann W, Tributsch H. Photoelectrochemistry of highly quantum efficiency single☐crystalline n☐FeS$_2$. Journal of the Electrochemical Society. 1986 Jan 1;133(1):97-106.

[66] Ennaoui A, Fiechter S, Tributsch H, Giersig M, Vogel R, Weller H. Photoelectrochemical energy conversion obtained with ultrathin organometallic☐ chemical☐vapor☐deposition layer of FeS$_2$ on TiO$_2$. Journal of the Electrochemical Society. 1992 Sep 1;139(9):2514-8.

[67] Puthussery J, Seefeld S, Berry N, Gibbs M, Law M. Colloidal iron pyrite nanocrystal inks for thin-film photovoltaics. Journal of the American Chemical Society. 2010 Dec 22;133(4):716-9.

[68] Klipstein PC, Friend RH. Semiconductor to semimetal transition in TiS$_2$ at 40 kbar. Journal of Physics C: Solid State Physics. 1984 May 30;17(15):2713-34.

[69] Yin G, Zhao H, Feng J, Sun J, Yan J, Liu Z, Lin S, Liu SF. Low-temperature and facile solution-processed two-dimensional TiS$_2$ as an effective electron transport layer for UV-stable planar perovskite solar cells. Journal of Materials Chemistry A. 2018 Apr 13;6(19):9132-8.

[70] Al-Kuhaili MF, Saleem M, Durrani SM. Optical properties of iron oxide (α-Fe$_2$O$_3$) thin films deposited by the reactive evaporation of iron. Journal of Alloys and Compounds. 2012 Apr 25;521:178-82.

[71] Gaudon M, Pailhé N, Majimel J, Wattiaux A, Abel J, Demourgues A. Influence of Sn^{4+} and Sn^{4+}/Mg^{2+} doping on structural features and visible absorption properties of α-Fe$_2$O$_3$ hematite. Journal of Solid State Chemistry. 2010 Sep 30;183(9):2101-9.

[72] Hahn NT, Mullins CB. Photoelectrochemical performance of nanostructured Ti-and Sn-doped α-Fe$_2$O$_3$ photoanodes. Chemistry of Materials. 2010 Nov 19;22(23):6474-82.

[73] Lukowski MA, Jin S. Improved synthesis and electrical properties of Si-doped α-Fe$_2$O$_3$ nanowires. Journal of Physical Chemistry C. 2011 Jun 8;115(25):12388-95.

[74] Shinde SS, Bhosale CH, Rajpure KY. Studies on morphological and electrical properties of Al incorporated combusted iron oxide. Journal of Alloys and Compounds. 2011 Mar 3;509(9):3943-51.

[75] Reddy GK, Gunasekera K, Boolchand P, Dong J, Smirniotis PG. High temperature

water gas shift reaction over nanocrystalline copper codoped-modified ferrites. Journal of Physical Chemistry C. 2011 Mar 29;115(15):7586-95.

[76] Zhang M, Luo W, Li Z, Yu T, Zou Z. Improved photoelectrochemical responses of Si and Ti codoped α-Fe_2O_3 photoanode films. Applied Physics Letters. 2010 Jul 26;97(4):042105.

[77] Kleiman-Shwarsctein A, Huda MN, Walsh A, Yan Y, Stucky GD, Hu YS, Al-Jassim MM, McFarland EW. Electrodeposited aluminum-doped α-Fe_2O_3 photoelectrodes: experiment and theory. Chemistry of Materials. 2009 Dec 30;22(2):510-7.

[78] Morikawa T, Kitazumi K, Takahashi N, Arai T, Kajino T. p-type conduction induced by N-doping in α-Fe_2O_3. Applied Physics Letters. 2011 Jun 13;98(24):242108.

[79] Martin ST, Morrison CL, Hoffmann MR. Photochemical mechanism of size-quantized vanadium-doped TiO_2 particles. Journal of Physical Chemistry. 1994 Dec;98(51):13695-704.

[80] Zhu J, Deng Z, Chen F, Zhang J, Chen H, Anpo M, Huang J, Zhang L. Hydrothermal doping method for preparation of Cr^{3+}-TiO_2 photocatalysts with concentration gradient distribution of Cr^{3+}. Applied Catalysis B: Environmental. 2006 Feb 22;62(3):329-35.

[81] Zhu J, Zheng W, He B, Zhang J, Anpo M. Characterization of Fe-TiO_2 photocatalysts synthesized by hydrothermal method and their photocatalytic reactivity for photodegradation of XRG dye diluted in water. Journal of Molecular Catalysis A: Chemical. 2004 Jul 1;216(1):35-43.

[82] Di Paola A, Marci G, Palmisano L, Schiavello M, Uosaki K, Ikeda S, Ohtani B. Preparation of polycrystalline TiO_2 photocatalysts impregnated with various transition metal ions: characterization and photocatalytic activity for the degradation of 4-nitrophenol. Journal of Physical Chemistry B. 2002 Jan 24;106(3):637-45.

[83] Choi W, Termin A, Hoffmann MR. The role of metal ion dopants in quantum-sized TiO_2: correlation between photoreactivity and charge carrier recombination dynamics. Journal of Physical Chemistry. 1994 Dec;98(51):13669-79.

[84] Sakthivel S, Kisch H. Daylight photocatalysis by carbon□modified titanium dioxide. Angewandte Chemie International Edition. 2003 Oct 20;42(40):4908-11.

[85] Asahi RY, Morikawa TA, Ohwaki T, Aoki K, Taga Y. Visible-light photocatalysis in nitrogen-doped titanium oxides. Science. 2001 Jul 13;293(5528):269-71.

[86] Umebayashi T, Yamaki T, Tanaka S, Asai K. Visible light-induced degradation of

methylene blue on S-doped TiO_2. Chemistry Letters. 2003 Mar 4;32(4):330-1.

[87] Wang H, Lewis JP. Second-generation photocatalytic materials: anion-doped TiO_2. Journal of Physics: Condensed Matter. 2005 Dec 14;18(2):421-34.

[88] Han C, Pelaez M, Likodimos V, Kontos AG, Falaras P, O'Shea K, Dionysiou DD. Innovative visible light-activated sulfur doped TiO_2 films for water treatment. Applied Catalysis B: Environmental. 2011 Aug 31;107(1):77-87.

[89] Xia C, Jia Y, Tao M, Zhang Q. Tuning the band gap of hematite α-Fe_2O_3 by sulfur doping. Physics Letters A. 2013 Oct 30;377(31-33):1943-7.

[90] Ohno T, Mitsui T, Matsumura M. Photocatalytic activity of S-doped TiO_2 photocatalyst under visible light. Chemistry letters. 2003 Mar 19;32(4):364-5.

[91] Yu JC, Ho W, Yu J, Yip H, Wong PK, Zhao J. Efficient visible-light-induced photocatalytic disinfection on sulfur-doped nanocrystalline titania. Environmental Science & Technology. 2005 Feb 15;39(4):1175-9.

[92] Pathakoti K, Morrow S, Han C, Pelaez M, He X, Dionysiou DD, Hwang HM. Photoinactivation of Escherichia coli by sulfur-doped and nitrogen–fluorine-codoped TiO_2 nanoparticles under solar simulated light and visible light irradiation. Environmental Science & Technology. 2013 Aug 16;47(17):9988-96.

[93] Umebayashi T, Yamaki T, Itoh H, Asai K. Bandgap narrowing of titanium dioxide by sulfur doping. Applied Physics Letters. 2002 Jul 15;81(3):454-6.

[94] Umebayashi T, Yamaki T, Yamamoto S, Miyashita A, Tanaka S, Sumita T, Asai K. Sulfur-doping of rutile-titanium dioxide by ion implantation: photocurrent spectroscopy and first-principles band calculation studies. Journal of Applied Physics. 2003 May 1;93(9):5156-60.

[95] Ho W, Jimmy CY, Lee S. Low-temperature hydrothermal synthesis of S-doped TiO_2 with visible light photocatalytic activity. Journal of Solid-State Chemistry. 2006 Apr 30;179(4):1171-6.

[96] Li D, Xia Y. Fabrication of titania nanofibers by electrospinning. Nano Letters. 2003 Apr 9;3(4):555-60.